UNIVERSITY OF OKLAHOMA

GRADUATE COLLEGE

IMPROVING QUANTIFICATION OF NANOSCALE INTERACTIONS BY ENGINEERING MONODISPERSE GOLD NANOPARTICLES

A DISSERTATION

SUBMITTED TO THE GRADUATE FACULTY

in partial fulfillment of the requirements for the

Degree of

DOCTOR OF PHILOSOPHY

By

ALEX FRICKENSTEIN

Norman, Oklahoma

2023

IMPROVING QUANTIFICATION OF NANOSCALE INTERACTIONS BY ENGINEERING MONODISPERSE GOLD NANOPARTICLES

A DISSERTATION APPROVED FOR THE

STEPHENSON SCHOOL OF BIOMEDICAL ENGINEERING

BY THE COMMITTEE CONSISTING OF

Dr. Stefan Wilhelm, Chair

Dr. Handan Acar

Dr. John Clegg

Dr. Rahki Rajan

Acknowledgements

To begin, I owe the overwhelming value of my graduate student career in large part to my Ph.D. adviser, Dr. Stefan Wilhelm. His exceptional guidance, tutelage, and support have propelled me to greater scientific and professional heights. Dr. Wilhelm went above and beyond to ensure my scientific pursuits were well-performed and well-communicated. Further, his coaching on preparing for faculty roles and applications far exceeded my expectations. I will value his advice for years to come as I move forward into the realms of undergraduate education. Thank you for accepting me as a member of the lab and as a colleague.

I would like to thank the members of my Ph.D. committee – Dr. Handan Acar, Dr. John Clegg, and Dr. Rahki Rajan. Their support and insight throughout my studies has been instrumental in managing both my research, teaching, and my work-life balance. The feedback they have offered on various aspects of my research goals and performance greatly shaped the trajectory I have taken with my studies. I look forward to working with you all throughout the remainder of my Ph.D. path and beyond.

Other faculty and staff members of the Stephenson School of Biomedical Engineering have also contributed to my growth and success. Dr. Michael Detamore as the department chair and as a mentor has provided advice that has benefitted my research, professionalism, and career aspirations. His support also helped me find new opportunity where I thought there was none. Thanks Dr. Rebecca Scott and Dr. Sarah Breen for sharing your insights and experiences on teaching-focused roles and philosophies, as well as for your support as I completed the faculty application processes. Thanks to Shayla Glover and Nicole Palmeter for their help in managing administrative

aspects of my graduates studies. Special thanks to Cherie Hudson as well, you live on in our hearts and memories for your invaluable support.

I want to thank Dr. Steven Foster of the Mass Spectrometry, Metabolomics, and Proteomics (MSPM) core facility for his assistance in using the ICP-MS. Your support as I was learning the instrument and later as I was effectively managing the ICP-MS for several labs and users was greatly appreciated. Thank you for advocating for me, my time, and my sanity as we navigated my role as a graduate assistant of MSPM. Thanks also for sharing your insights on the behind-the-scenes workings of department and faculty goings-on. Your wisdom and friendship are extremely valued.

Thanks for Dr. Andrew Madden, Dr. Preston Larson, Dr. Julian Sabisch, Dr. Tingting Gu, and the other faculty and staff of the Samuel Roberts Noble Microscopy Laboratory (SRNML) for training me in how to use transmission electron microscopy. Your support of my work and teaching me in how to use the instruments and software for image analysis was monumental to the success of my studies. Thanks also to Dr. Ben Fowler of the Oklahoma Medical Research Foundation (OMRF) for support with providing access the confocal laser scanning microscope.

The Wilhelm Lab team has also been instrumental in the completion of this work and in furthering my career. Thanks to former members Dr. Nathan Donahue and Dr. Wen Yang for training me in nanoparticle synthesis, ICP-MS, data analysis, and project management. I would like to thank Dr. Lin Wang for her support in experiment design and ideation through every step of my research journey. Thanks to former member Alyssa Holden for bearing with me as my first mentee and helping me setup my initial research endeavors. Thanks to Vinit Sheth and Yuxin He for working with me on the cell

management, confocal microscopy, and protein assay components of my projects, as well as for your friendship. I want to thank all my undergraduate and high school mentees as well for their support in project completion and for giving me the chance to hone my mentorship skills: Tekena Harcourt, Zain Malik, Nathan Mjema, Tyler Wilson, Luke Whitehead, Logan Longacre, Haley Taffe, Izzy McSpadden, Sarah Butterfield, and Shirsha Mukherjee. Also, I want to say thanks and welcome to Nathan Means, who will be continuing where my investigations leave off. I am excited to see how you carry this work closer to application in patient care environments.

Finally, I would like to thank my wife, Katie, for being an ever-present source of encouragement, love, and inspiration during my studies. You always listened, providing wisdom and suggestions I never would have thought of. Thanks also to my father, mother, brother, and extended family for their constant love and support as I navigated this exciting and challenging endeavor.

Table of Contents

List of Figures

Chapter 1

Chapter 2

Chapter 3

Chapter 4

List of Tables

Chapter 1

No tables

Chapter 2

Chapter 3

Chapter 4

Chapter 5

Chapter 6

No Tables

Abstract

Mechanisms of nanoparticle-cell interactions are dependent upon the size of the administered nanoparticles. At pre-clinical and clinical levels, precise control over the size and monodispersity of nanoparticles is required to produce consistent, effective, well-understood results. Gold nanoparticles (AuNPs) are a commonly used model nanoparticle for understanding nano-bio interactions based on AuNPs relative ease of synthesis and characterization. While ensemble characterization methods of AuNPs made using citrate-based synthesis approaches indicate relative size monodispersity, single nanoparticle analytical techniques reveal a wide size distribution. This wide size distribution decreases confidence in exact size-interaction correlations within nano-bio interactions and confounds sensitivity of single nanoparticle analysis. There is a need for AuNPs possessing a lower size distribution for improving single cell and single nanoparticle analyses of nano-bio interactions. In the current dissertation, single particle inductively coupled mass spectrometry (SP-ICP-MS) is used to characterize AuNPs synthesized using two different synthesis methods – citrate-based and CTAC-based – to identify differences in size monodispersity. Our analysis confirmed that CTAC-based AuNPs possess a tighter size distribution compared to citrate-based AuNPs. SP-ICP-MS was used to assess size prediction and synthesis scale-up models for each of the two synthesis methods. Further, AuNP growth kinetics of CTAC-based synthesis were characterized. AuNPs synthesized using CTAC-based methods are innately cytotoxic, making them unfit for biomedical use immediately after synthesis. To overcome this challenge, different methods of surface modification were developed that improved biocompatibility and biofunctionalization of CTAC-based AuNPs. SP-ICP-MS measurements confirmed that surface modification strategies did not result in a change

in monodispersity, maintaining a tight size distribution for CTAC-based AuNPs. Biocompatible, biofunctional CTAC-based AuNPs were compared to citrate-based AuNPs in cell viability, cell uptake, and surface ligand interaction experiments. The overall findings of these results provide tools and methods by which highly monodisperse AuNPs may be synthesized, modified, and applied to better understand nano-bio interactions. Further, these results illuminate the possibilities and advantages of applying biocompatible monodisperse AuNPs in nanomedicine.

Chapter 1 – Introduction

The overarching goal of this work is to demonstrate that highly monodisperse gold nanoparticles (AuNPs) may provide better results in probing and understanding nanoparticle characterization and interactions biological systems. AuNPs are commonly used in current nanomedicine efforts based on their ease of synthesis, relative biocompatibility, and multifunctional behavior. AuNPs serve as ideal model nanoparticles for understanding how nanomaterials interact with cells and tissues. Largely, the utility of AuNPs stems from the high atomic weight of gold (Au), the interaction of light with AuNPs, and their easily modifiable surface that permits experimentation with a wide range of surface chemistries and molecular payloads. By using AuNPs in preliminary nanomedicine experiments and studies, we may learn more about how nanoparticle characteristics such as size, shape, charge, and surface chemistry may influence interactions with cellular and tissue environments. We can then apply the knowledge gained from AuNP experiments and translate them to alternative nanoparticle formulations for therapy, imaging, or vaccination.

In an ideal nanoparticle suspension, all nanoparticles would be exactly the same in terms of size and shape. This “interparticle similarity” is commonly referred to as “monodispersity,” where a monodisperse nanoparticle formulation is one where the suspended nanoparticles are similar to each other in terms of size and shape. Given the complex nature of nanoparticle synthesis and stability, such ideal suspensions are near impossible to create or maintain. This inevitability holds true for AuNPs as well. One of the commonly used AuNP formulations used in nanomedicine uses AuNP synthesized from a bottom-up, seed-mediated synthesis method that uses citrate as the primary

stabilizing agent. While preliminary characterization methods, such as dynamic light scattering, may indicate AuNPs synthesized using this citrate-based method are relatively monodisperse in solution, single-particle characterization methods, such as single particle inductively coupled plasma mass spectrometry, reveal a wide distribution of nanoparticle mass, size, and shape.

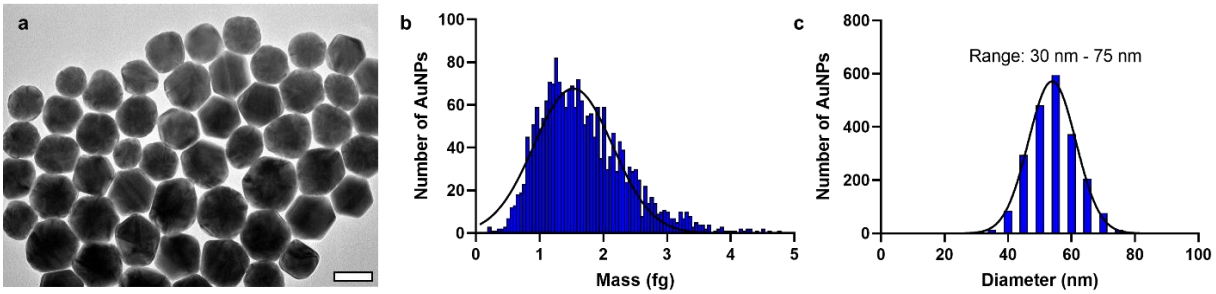

Figure 1.1: **Representative TEM imaging and SP-ICP-MS analysis of citrate-based AuNPs. a)** TEM micrograph image of ~55 nm diameter citrate-based AuNPs, showing a wide size and shape variety of AuNPs. Scale bar is 50 nm. **b)** Mass distribution of the mass distribution of ~55 nm AuNPs as measured by SP-ICP-MS. Black line shows the Gaussian normal distribution of measured masses. **c)** Estimated AuNP diameter distribution as calculated from the measured mass distribution from SP-ICP-MS with the range of AuNP sizes shown. Black line shows the Gaussian normal distribution of measured masses.

As seen in Figure 1.1, there is a wide variety of AuNP sizes and shapes in what is considered to be a monodisperse AuNP suspension. This size distribution poses a problem when compared against a principle assumption in nanomedicine research: nanoparticles used to treat cells or *in vivo* models are all the same size and shape. Clearly, this assumption does not apply to citrate-based AuNPs and decreases confidence in exact correlation between observed nanoparticle effect and exact nanoparticle size. After all, with a distribution of sizes as shown, it is challenging to identify which particles within the measured size distribution induce or significantly contribute towards the observed effect. Additionally, in the case of single-nanoparticle analysis, the wide size distribution limits our ability to resolve between nanoparticles from AuNP populations batches of different target diameters due to overlap of measured distributions.

There is an evident need for improved model AuNP with tighter size distributions that a) better align with key assumptions in nanomedicine relative to uniform nanoparticle size and shape and b) allow for accurate resolution between AuNPs from suspensions of different target diameters.

This dissertation aims to identify a AuNP formulation that possesses an improved size and shape monodispersity compared to citrate-based AuNPs. From the literature, I observed that AuNPs synthesized using a cetyltrimethylammonium chloride (CTAC)-based approach appeared to be more monodisperse based on electron micrograph images. Based on these literature observations, I sought to use SP-ICP-MS as a high-throughput elemental analysis technique with single nanoparticle resolution to characterize differences between citrate-based and CTAC-based AuNPs. Towards this end, I developed three principal research aims. My first research aim is to quantify the difference in monodispersity between citrate-based and CTAC-based AuNPs. During this aim, I would also identify an initial method for removing cytotoxic CTAC from the surface of CTAC-based AuNPs and replacing it with PEG. My second research aim was to predictive models that relate AuNP reaction input to final synthesized diameter and allow for easy reaction scale-up. Finally, my third research aim is to develop a novel approach for replacing CTAC directly with citrate, allowing for improved comparison between citrate- and CTAC-based AuNPs relative to surface topology and size monodispersity. SP-ICP-MS is a pivotal elemental analysis technique necessary to achieve all research aims given its single nanoparticle resolution and was used extensively during my studies. Central to all of these aims is SP-ICP-MS given its ability to measure individual nanoparticles in solution. This advantage provides opportunity for exact quantification in

differences between AuNP type as well as monitoring changes in colloidal stability during CTAC removal processes.

The following chapters detail my findings as I achieved the above research aims. Chapter 2 provides an overview of single cell elemental analysis techniques used in quantifying nano-bio interactions. I discuss several techniques for measuring exogenous and endogenous elements in cells treated with nanoparticles. In particular, I highlight the apparent value of time-of-flight analyses for its multi-element analysis capabilities. I conclude with discussing promising future directions for the field relative to enhancing quantification of nano-bio interactions.

In Chapter 3, Aim 1 of the proposed research strategy is addressed. I started by synthesizing AuNPs using two different methods: citrate-based and CTAC-based. I characterized AuNPs using both population-based batch methods (DLS, UV-Vis) and single-particle analysis methods (TEM, SP-ICP-MS). My results indicate that AuNPs synthesized using CTAC-based methods demonstrate improved size monodispersity compared to AuNPs synthesized by citrate-based methods. I also developed an initial method by which CTAC-based AuNPs can be made biocompatible and biofunctional using physical replacement to remove CTAC, allowing PEG to covalently bind to the gold surface. Cell viability and cell uptake experiments affirmed the safety and functionality of these surface-modified CTAC-based AuNPs, indicating their utility in biomedical and bioanalytical applications.

In Chapter 4, I aim to expand upon current synthesis approaches using SP-ICP-MS analysis, thus addressing Aim 2. Based on literature methods, I characterized the relationship between the molar ratio of ionic gold and AuNP seeds used in AuNP growth

reaction to develop a robust mathematical model to predict final AuNP diameter. SP-ICP-MS was used to estimate AuNP diameter for both citrate-based and CTAC-based synthesis. I performed yield estimates for both reactions based on SP-ICP-MS results, and I showed how reaction scale-up was readily possible based on mathematical model design. Finally, I measured the growth of CTAC-based AuNPs using SP-ICP-MS, highlighting the possible mechanisms of AuNP growth during CTAC-based AuNP synthesis reactions. These compiled results provide avenues by which researchers may readily synthesize AuNPs of desired diameter and amount for research applications.

In Chapter 5, I further developed the CTAC physical replacement techniques described in Chapter 3 by showing how citrate can replace CTAC. The method I developed uses similar mechanics to the previous PEGylation approach but uses citrate as the primary surface ligand. Our hypothesis was that by replacing CTAC with citrate using our physical replacement (PR) approach, we would impart similar properties, in terms of biocompatibility and surface modification potential, as seen in originally citrate-based synthesized AuNPs to originally CTAC-based synthesized AuNPs while maintaining the improved monodispersity seen in CTAC-based AuNPs. I extensively characterized the post-PR AUNPs to verify CTAC removal while maintaining monodispersity. I then compared citrate-based AuNPs to post-PR CTAC-based AuNPs in terms of surface area saturation, nanoparticle-protein interactions, and cellular viability and uptake.

In Chapter 6, I conclude this dissertation by summarizing the primary findings and how they inform upcoming experiments on the currently discussed study topics. I also indicate exciting future directions for the field based on my discovered results. I end with

a discussion of the opportunities for applying my highly monodisperse AuNPs in patient diagnostics.

Chapter 2 – Elemental Analysis Techniques for Understanding Nano-Bio Interactions

2.1 Abstract

Nanomedicine efficacy is reliant upon a thorough understating of the interactions between nanoparticles and cells (i.e., “nano-bio” interactions). Many factors alter nano-bio interaction mechanisms, with nanoparticle characteristics such as size, shape, and surface chemistry being particularly influential. Quantification of nano-bio interactions allows for accurate determination of valuable methods of nanoparticle engineering for improved nanoparticle uptake or effect. Analyzing and quantifying cells at the single-cell level is particularly valuable given the increased resolution compared to batch population-based analysis. In this chapter, we review methods and technologies used for element analysis of single-cell systems. In particular, we focus on inductively coupled plasma mass spectrometry (ICP-MS) approaches for measuring endogenous or exogenous elements in cellular samples. Current trends in the field are discussed with potential future directions indicated that could improve elemental analysis methods and quantification of nano-bio interactions.

Section(s) 2.3 – 2.4 and Section 2.6 have published as a part of a review manuscript in *Trends in Analytical Chemistry (TrAC)* – IF 14.908 – as:

Haddad M*, **Frickenstein A***, Wilhelm S, “High-Throughput Single-Cell Analysis of Nanoparticle-Cell Interactions,” *TrAC*, 2023, 166, DOI: 10.1016/j.trac.2023.117172

Authors and contributors:

Majood Haddad* – Composed the flow cytometry sections

Alex Frickenstein* – Composed the elemental analysis sections

Stefan Wilhelm – Oversaw manuscript completion

* Denotes equal contribution

2.2 Introduction

The field of nanomedicine relies upon understanding the nature of nanoparticle interactions with cells (i.e., “nano-bio interactions”) in order to improve patient outcomes.[1-3] Nanoparticles are defined as 1-100 nm particles and can be comprised of either inorganic materials, such as gold, silver, or platinum, or organic materials, such as polymers or lipids.[4] Primarily, nanoparticles are synthesized and modified for specific clinical applications. Nanoparticle targeted clinical applications vary from therapeutic drug delivery, imaging diagnostics, and vaccination.[5-9] At the core of each of nanoparticle application is nano-bio interactions that dictate nanoparticle fate, safety, and efficacy. To better probe and understand the interactions between nanoparticles and cells, researchers require robust analytical techniques to spatiotemporally resolve nano-bio interactions at the single-cell and single-nanoparticle levels. This research has the potential to guide the engineering of safer and more effective nanomedicines for improved clinical outcomes.[10,11]

Single-cell analysis allows for increased resolution and understanding of cellular mechanisms and behaviors relative to nano-bio interactions. It is well understood that nanoparticle characteristics such as size, shape, and surface chemistry influence nano-bio interactions.[12-19] Detailed understanding of how nanoparticle characteristics influence nano-bio interactions is required to improve nanomedicine clinical safety and efficacy.

While batch mode, population-based analysis can provide insight into broad trends in nano-bio interactions based on changes in nanoparticle characteristics, batch analysis fails to indicate the cellular or subcellular distribution of nanoparticles in cells. Additionally,

batch analysis relies upon assumptions that may not hold true for all samples, such as the assumption that all cells contain nanoparticles or that all nanoparticles have the same size, shape, and mass.

Single-cell analysis allows for distribution analysis to understand the range of nano-bio interactions for a given system and can identify cells that contain no nanoparticles after treatment. Additionally, for blood or tissue samples comprised of a complex cellular milieu, single-cell analysis allows for the identification and quantification of different cell identities (i.e., phenotypes) and corresponding nano-bio interactions on a per-cell basis that can point towards valuable nanoparticle design strategies. For example, by identifying how nanoparticles may have increased or decreased interactions with particular cell types in complex cellular systems (e.g., tissues), nanomedicines may be better engineered for enhanced safety and efficacy, Further, where possible, imaging of cells during single-cell analysis increases data value and provides opportunity for correlating nanoparticle quantity with sub-cellular accumulation.

Currently, there are three primary methods of quantifying nano-bio interactions at the single-cell level: microscopy, flow cytometry, and mass spectrometry. Of these, mass spectrometry allows for high-throughput accurate quantification of cells and nanoparticles with both single-cell and single-nanoparticle resolution.[20,21] By comparison, microscopy allows for visualization and relative quantification of nano-bio interactions though it is generally low-throughput and requires extensive sample preparation and image analysis methods. Advances in microscopy have been examining methods of increasing throughput of single cells; reporting of these studies is left to other reviews.[22-25] Flow cytometry can allow for the quantification and identification of cell phenotypes but lacks

the ability to accurately quantify the number of nanoparticles per cell.[26,27] As with microscopy, recent advances in flow cytometry provide new options for single-cell analysis and are left to be explored in other literature.[28]

In this review, we highlight current advances in mass spectrometry instrumentation and methodology for quantifying nano-bio interactions. Specific focus is given to inductively coupled plasma mass spectrometry approaches given its high-throughput and high-resolution. The intersection of flow cytometry with mass spectrometry has been explored in the form of CyTOF, which will be discussed in this review.

2.3 Elemental Analysis and Mass Spectrometry

Direct analysis of individual elementals is a powerful tool for quantifying nanoparticle-cell interactions. Cells possess endogenous elemental fingerprints that can be used to identify cells compared to background signals. Additionally, exogenous staining or labeling agents can be used to identify cells using high atomic weight isotopes (i.e., Ir, Y, etc.). Nanoparticles comprised of inorganic elements or tagged with elemental markers can be identified and quantified. Quantifying the amount of each element in cell samples exposed to elemental labeling agents or nanoparticles allows for accurate quantification of nanoparticle interactions with cells and can be used to identify cell phenotype. While multiple tools can be used for elemental quantification, one of the most used and effective methods is inductively coupled plasma mass spectrometry (ICP-MS). Here, samples are atomized and ionized by an argon plasma and the resulting ion cloud is focused and filtered through transmitting ion lenses for quantification of desired ions.[29] The high throughput capabilities of ICP-MS technology allow for hundreds of cells to be quantified per minute. When paired with the sensitivity of the technology, trace amounts of elemental signal can be detected and quantified with appropriate calibration [30]. These characteristics of ICP-MS paired with recent advances in the field propel ICP-MS technology to the forefront of effective means of quantifying nanoparticle-cell interactions at the single-nanoparticle and single-cell level.

2.3.1 Quadrupole ICP-MS

The most widely used iteration of ICP-MS instruments is quadrupole ICP-MS (ICP-Q-MS). ICP-Q-MS uses a quadrupole to filter out undesired ions, permitting accurate detection and quantification of a single specific ion.[29] ICP-Q-MS has been used to quantify nanoparticle-cell interactions in multiple studies, though many of these approaches require destruction of cell samples through acidification.[31-34] Further, the resulting data only provides mean population data that fails to reach the ideal of single-nanoparticle and single-cell resolution. Single particle ICP-Q-MS (SP-ICP-Q-MS) approaches provide avenues for quantifying elements one cell at a time through using alternative hardware compared to traditional ICP-Q-MS. SP-ICP-Q-MS has been used to quantify cellular uptake of gold [20,35,36], silver [37-39], and platinum [40] nanoparticles in varying cells lines, as shown in Table 2.1. In each case, the presence and number of nanoparticles in cells could be accurately identified, providing insight into nanoparticle-cell interactions at the single-cell level. SP-ICP-Q-MS has also been used to quantify elements intrinsic to themselves, such as copper and zinc.[41]

Introduction of single cells into the instrument is a key consideration when assessing measurement of individual cells. SP-ICP-Q-MS does not possess innate methods for visualizing or identifying cell entry into the instrument, relying solely upon exogenous or endogenous elemental signal detection and analysis to identify cell entry and measurement. Additionally, sample introduction methods do not delivery cells with 100% transport efficiency and may also introduce opportunity for multi-cell event quantification. Recent innovative methods for improving and tracking introduction of single cells for ICP-MS analysis include microfluidic control mechanisms, magnets, and cameras to visualize individual cell entry into the instrument.[42-45]

Another method to ensure measured signal aligns with single cells is to count cells through cell-associated elemental analysis. Based on quadrupole settings and short transient ion signals from cells and nanoparticles, SP-ICP-Q-MS on its own is only capable of accurately measuring one element at a time.[29,41] While quantifying a single element allows for label-free cellular quantification, this single-element quantification approach is also a limitation that prevents simultaneous quantification of both cell-associated or cell-labeling elements and nanoparticles.[21] Recent studies have overcome this limitation using dual-analyte techniques, whereby the transient ion cloud resulting from ionization at the plasma torch is stretched using collision gases, such as NH_3 (Figure 2.1A).[46-48] This ion cloud stretching provides ample time for quadrupole switching to occur within the same event (i.e., particle), allowing for two elements to be measured for each sample. Donahue *et al*. used this approach to quantify gold nanoparticle uptake in nonadherent Raji B cells. After incubation with gold nanoparticles conjugated to peptides that increase cellular uptake, the cells were labeled with ^{114}Cd quantum dots and fixed using paraformaldehyde. Dual-analyte SP-ICP-Q-MS was then used to measure both ^{197}Au and ^{114}Cd simultaneously, so both gold nanoparticles and cells could be quantified by ^{197}Au and ^{114}Cd, respectively (Figures 2.1B-2.1D).[21] In this study, ^{114}Cd quantum dot labeling was used instead of more traditionally applied ^{193}Ir labeling due to the weak ^{193}Ir signal intensity measured using dual-analyte methods, demonstrating that this method reduces signal intensity and, thus, influences the limit of detection. By using dual-analyte SP-ICP-Q-MS approaches, simultaneous tracking of cells and nanoparticles is made possible, expanding upon current SP-ICP-Q-MS options for understanding nanoparticle-cell interactions.

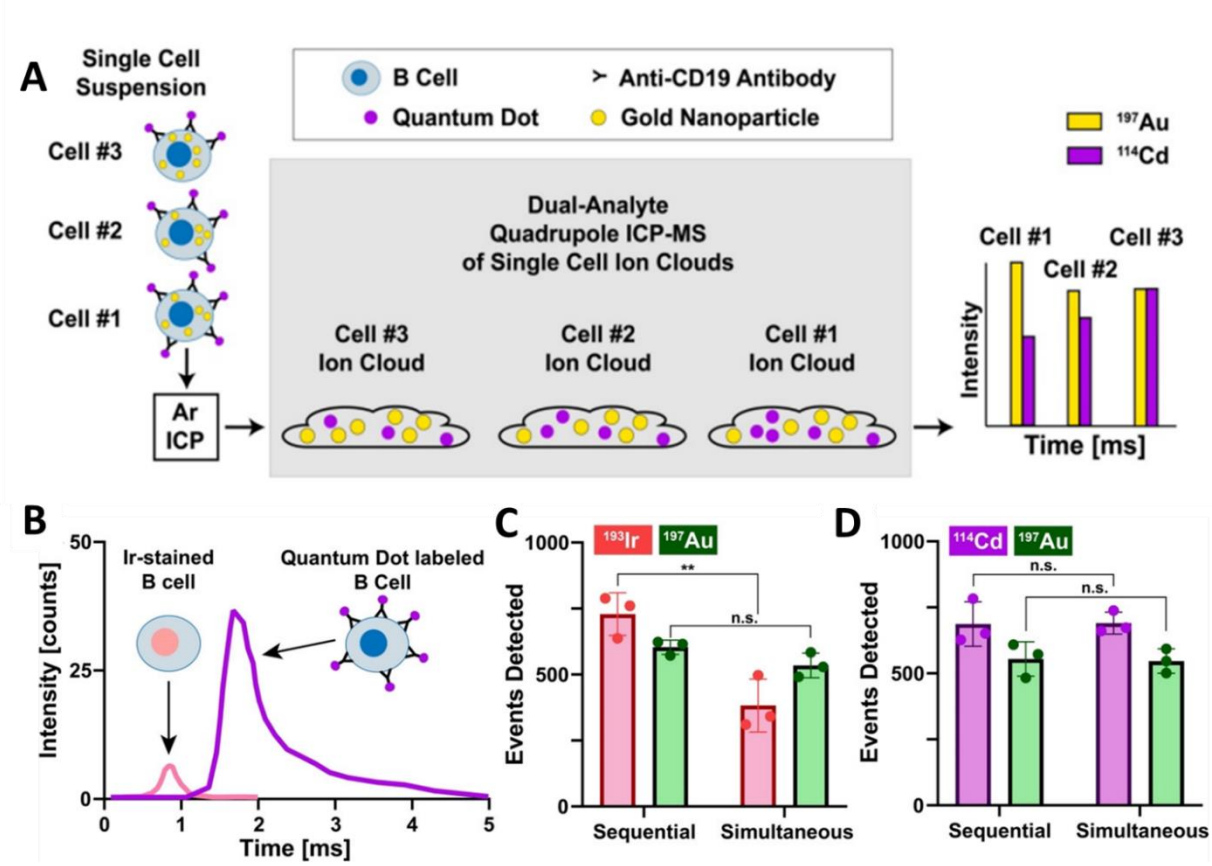

Figure 2.1: SP-ICP-Q-MS analysis of two elements in single cells using dual-analyte ICP-Q-MS techniques. (A) Schematic overview of sample introduction and measurement workflow. Ion clouds containing the two ions to be analyzed are stretched using collision gases to allow for simultaneous ion measurements. **(B)** Cells stained with ionic ^{193}Ir possess a different transient ion cloud intensity peak compared to cells labeled with ^{114}Cd-containing quantum dots when dual-analyte ICP-Q-MS conditions are used. **(C)** Counting of AuNP-containing cells stained with ionic ^{193}Ir using sequential or simultaneous (i.e., dual-analyte) operating modes demonstrates a mismatch in accurate cell counting. **(D)** Counting of AuNP-containing cells labeled with ^{114}Cd-containing quantum dots using sequential or simultaneous (i.e., dual-analyte) operating modes demonstrates maintained accuracy in cell counting. Reprinted with permission from Ref. [21]. Copyright 2023 American Chemical Society.

2.3.2 Laser Ablation ICP-MS

Traditionally, ICP-Q-MS measurements are performed using aqueous solutions or with samples suspended in solution (i.e., non-adherent cells). Adherent or dried cells can be quantified using laser ablation ICP-MS approaches (LA-ICP-MS), whereby individual cells can be ablated with a laser and the resulting aerosol is carried to the ICP-MS for quantification.[49] Previous studies have used this technique to quantify metallodrugs, such as cisplatin, in cell and tissue samples following treatments.[50-54] Nanoparticle uptake in cells and tissues has also been measured using LA-ICP-MS.[55-57]

Historically, challenges with LA-ICP-MS single cell analysis include ablating individual cells, comparing ablated signal against appropriate standards, and low throughput of LA-ICP-MS methods. Recent studies have aimed to overcome these issues using novel approaches for arraying individual cells inside of droplets containing known concentrations of ionic standards. One study by Zheng *et al*. used microfluidic channels to flow RAW 264.7 murine macrophages treated with silver nanoparticles through a PDMS mold containing evenly spaced “traps” to capture individual cells, which then adhere to the surface of the dish (Figure 2.2A-2.2C). After the mold was removed (Figure 2.2D), an inkjet printer dispensed a droplet of known ion concentration onto each individual cell (Figure 2.2E) before the cells were quantified by LA-ICP-MS (Figure 2.2F-2.2I). LA-ICP-MS results for nanoparticle uptake matched those observed from standard ICP-Q-MS quantification.[58] Similar cell array and doped droplet approaches have been used with ICP-Q-MS [59] and time-of-flight ICP-MS analysis.[60]

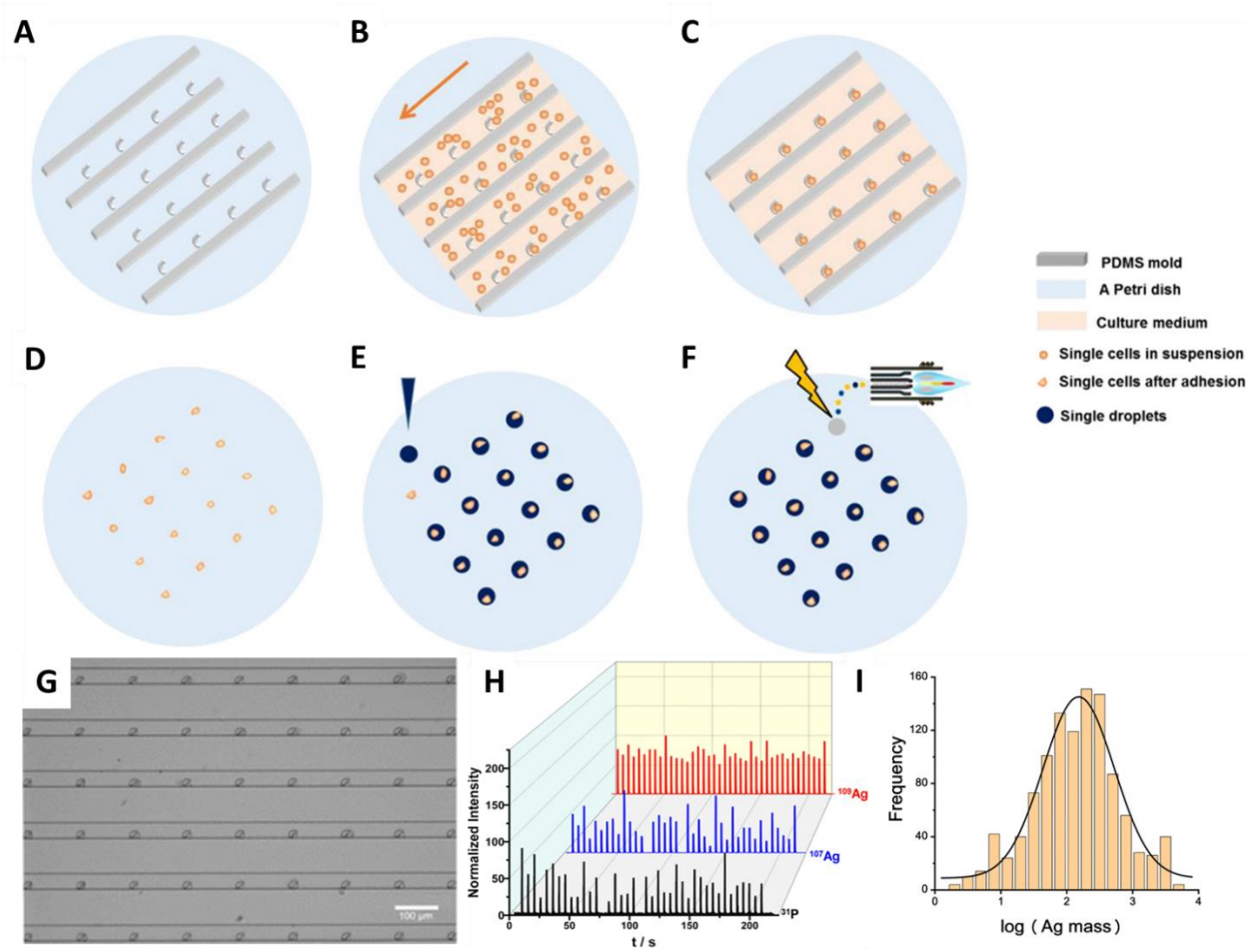

Figure 2.2: Arraying single cells for laser ablation ICP-MS analysis. (A) A PDMS mold possesses hook-shaped traps to capture individual cells. **(B)** Cells suspended in media flow through the mold, resulting in the capture of individual cells inside the hook-shaped traps. **(C)** Trapped cells are allowed to adhere to the Petri dish where cell capture occurred. **(D)** The PDMS mold is removed, leaving individual cells arrayed on the Petri dish. **(E)** Droplets enriched with the ion of interest (i.e., ^{109}Ag) are dropped onto each arrayed cell. **(F)** Each point in the array, containing a single cell inside the ion-enriched droplet, is ablated via laser and quantified by ICP-Q-MS. **(G)** Single cells trapped inside the hook-shaped traps of the PDMS mold can be seen using brightfield microscopy imaging. **(H)** Transient ion signals collected during laser ablation ICP-Q-MS measurements of arrayed single cells treated with AgNPs. **(I)** Quantified Ag content of measured cells. Reproduced with permission from Ref. [58]. Copyright 2023 American Chemical Society.

2.3.3 Time-of-Flight ICP-MS

Another approach for ICP-MS elemental quantification uses time-of-flight methods (TOF-ICP-MS). Here, the transient ion signal formed during the atomization and ionization of the sample is separated into individual ion signals in a time-of-flight mass analyzer. This separation occurs based on principle differences in the mass-to-charge (i.e., *m/z*) ratio values between ions and allows for the quantification of multiple ions in the same analyzed particle.[61] Additionally, the sensitivity of TOF-ICP-MS allows for the quantification of low atomic weight elements, with carbon having been successfully quantified in polymer beads.[62] This ability allows for cells to be identified and quantified without the need for cell visualization or tracking strategies during sample introduction. Additionally, exogenous labeling or staining agents can be disregarded as the elemental footprint of individual cells themselves can be sufficiently detected.[63,64]

Single cell analysis by TOF-ICP-MS remains a relatively new approach and has been mainly applied for environmental analysis rather than biomedical.[65,66] One study by Hendriks *et al*. used TOF-ICP-MS to assess gold nanoparticle and $BaSO_4$ nanoparticle uptake by algal cells, using magnesium and phosphorus ion signals to identify cells.[67] Signal overlap between nanoparticle ions (^{197}Au or ^{138}Ba) and cell ions (^{24}Mg and ^{31}P) was interpreted as an indication of interactions, such as cell uptake, between cells and nanoparticles. Other applications of TOF-ICP-MS for single-cell analysis are typically applied alongside flow cytometry technologies, as will be discussed in the next section. Continued investigation into the use of TOF-ICP-MS applications for biomedical and nanomedicine applications is encouraged.

Particularly for biological samples, matrix effects can complicate ICP-MS analysis due to the complex composition of biological and cellular media.[68,69] Removing the

matrix effects from sample analysis provides greater confidence in the results. One recent development in the field of TOF-ICP-MS is the use of online microdroplets during sample introduction to overcome sample matrix effects (Figure 2.3).[70-72] After nebulization but before atomization and ionization, cells or particles introduced into the instrument are immersed in microdroplets doped with known concentrations of multiple elements, including the element(s) of interest.

Current studies have shown the value of microdroplet approaches for accurately quantifying nanoparticles in varying matrices.[70,72] The translation of this technology to single-cell experiments offers new opportunities for minimizing matrix effects and increasing confidence in collected data. While these approaches could be used with other ICP-MS techniques, TOF-ICP-MS proves to be the best option based on its unique ability to simultaneously quantify multiple elements, from both the sample and the doped microdroplets, at the single-particle level.

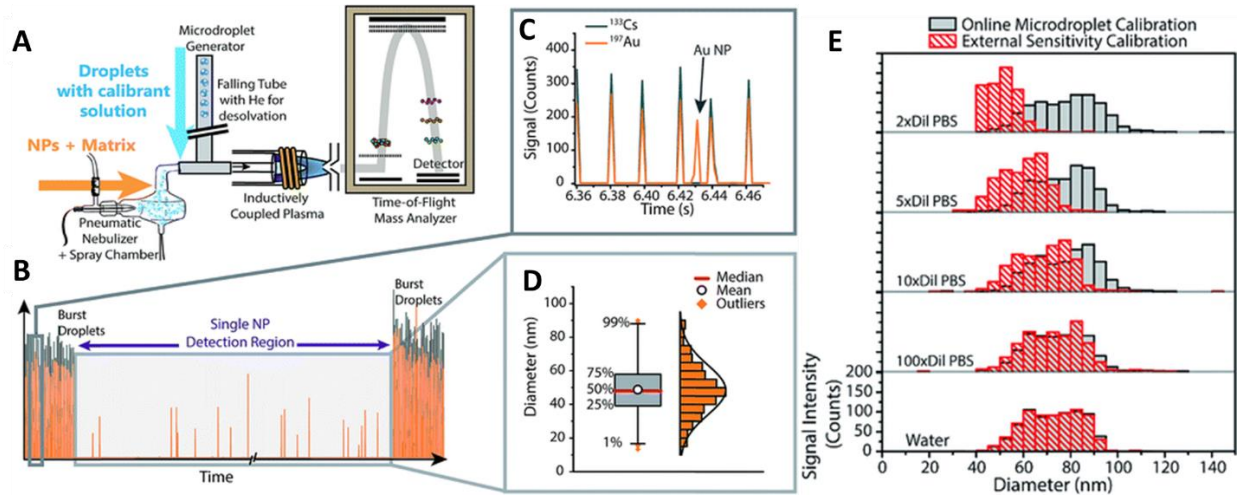

Figure 2.3: Online microdroplet methods paired with TOF-ICP-MS overcome sample matrix effects. (A) Schematic demonstrating the methodology behind online microdroplet systems. Microdroplets are doped with the ion of interest along with other elements and are added to the sample after nebulization during sample introduction. **(B)** Real-time ionic signal from TOF-ICP-MS measurement of gold nanoparticles with microdroplets. Microdroplets are introduced on the front and back end of sample analysis, allowing for nanoparticle-only identification and quantification in between droplet regimes. **(C)** Gold nanoparticle events are differentiated from microdroplet events as the microdroplets contain multiple overlapping elements. **(D)** After identifying nanoparticle events independent of microdroplets, gold nanoparticle analysis occurs similarly to standard SP-ICP-MS. **(E)** Use of the microdroplet system removes matrix effects from gold nanoparticles suspended in different PBS concentrations, accurately measuring AuNP diameter without suffering from signal attenuation associated with the matrix. Reproduced from Ref. [70] with permission from the Royal Chemistry Society.

Table 2.1: Summary of Single-Cell Studies Using ICP-MS Instrumentation

Instrument	Cell (Label) Elements	Nanoparticle Elements	Cell Line(s)	Notable Methodology	References
SP-ICP-Q-MS	None	^{197}Au	Human T24	As few as one PEGylated gold nanoparticle could be detected per cancer cell.	[20]
	None	^{197}Au	*Cyptomonas ovate*	Gold nanoparticle uptake measured in algal cells	[36]
	^{63}Cu, ^{64}Zn	^{197}Au	CP70, A2780, CAOV3	*Distinct* quantification of gold nanoparticle uptake and cell ionic signal	[41]
	None	^{197}Au	MDAMB231, T47D	Detailed computations and correlation of nanoparticles with electron microscopy	[35]
	^{114}Cd (label)	^{197}Au	Raji B Cells	Dual-analyte detection through ion-cloud stretching by collision gases (NH_3)	[21]
LA-ICP-Q-MS	^{31}P	^{107}Ag, ^{109}Ag	RAW 264.7	Cellular array for individual cell ablation	[58]
	^{31}P	^{107}Ag, ^{109}Ag	16HBE human normal bronchial epithelial cells	Cellular array for individual cell ablation	[59]
LA-TOF-ICP-MS	^{23}Na, ^{24}Mg, ^{31}P, ^{66}Zn, ^{191}Ir (label), ^{193}Ir (label)	None	THP-1	Cellular array for individual cell ablation, quantification of multiple endogenous cellular elements	[60]
TOF-ICP-MS	^{24}Mg, ^{31}P	^{197}Au, ^{138}Ba	*Raphidocelis subcapitata*	Simultaneous detection of multiple endogenous cell and exogenous nanoparticle elements	[67]
CyTOF	^{191}Ir (label)	^{109}Ag	THP-1	Silver nanoparticles used during calibration to improve nanoparticle quantification	[73]
	^{191}Ir, ^{193}Ir (label)	^{107}Ag, ^{109}Ag	TIB-152	Ir staining of cells prior to nanoparticle treatment	[74]
	^{191}Ir (label)	^{107}Ag	Jurkat	Ir staining, results compared to traditional ICP-MS and SP-ICP-Q-MS	[75]
	^{147}Sm, ^{152}Sm, ^{168}Er, ^{172}Yb, ^{174}Yb, ^{176}Yb, ^{148}Nd, ^{142}Nd, ^{159}Tb, ^{170}Er, ^{151}Eu, ^{165}Ho, ^{191}Ir, ^{193}Ir (all labels)	^{197}Au	RAW 264.7, C57BL/6 mouse lymph node tissue	Assessing gold nanoparticle uptake by murine cells and murine cell phenotyping to identify differences in nanoparticle interaction based on cellular identity	[76]

2.4 Mass Cytometry

While mass spectrometry and flow cytometry are independently valuable in quantifying nanoparticle-cell interactions, combining the two techniques affords additional analysis opportunities. Mass cytometry, commonly referred to as CyTOF, combines elemental time-of-flight aspects of mass spectrometry with flow cytometry techniques to identify cells in heterogenous mixtures and subsequently quantify differences in, for example, nanoparticle uptake (Figure 2.4A).[76,77] Since fluorophore emission spectra can overlap, it is preferable to tag antibodies with heavy metal ions rather than with fluorochromes.[77-79] CyTOF instruments do not function in the same way as conventional flow cytometers as they do not have forward scattering signal or side scattering signal light detection or fluorescence signal detection.[26] CyTOF can discriminate between isotopes of various atomic masses with high accuracy; instead of coupling cell-labeling probes (i.e., antibodies) to fluorophores, CyTOF uses probes that are coupled to stable heavy-metal isotopes.[77,80] Cell-labeling probes can be extracellular or intracellular, the latter using primarily iridium (Ir) staining methods. CyTOF allows for the analysis of up to 100 isotopes at one time while performing single cell quantification, greatly expanding the possible range of cell analysis options.[81,82] The wide possibility space for isotopic analysis and corresponding cellular features (i.e., phenotypes) distinguishes CyTOF as an effective tool for quantifying complex samples, such as for immune cell analysis.[83,84]

Exogenous heavy metal labeling of cells is required in CyTOF to detect and quantify cells as the mass filters cutoff elements below 80 amu, thus preventing the detection of endogenous cellular elements.[85] This cutoff is primarily set to limit background noise and signal interference, as can come from argon dimers (Ar_2), but also

limits endogenous elemental quantification.[86] Additionally, in order for the instrument to obtain sensitivities comparable to those of the fluorophores, ~100 atoms of a given isotope should be bound to each antibody or probe, and multiple probes must be associated with cells for accurate cell detection and quantification. The quantity of the isotopes for a particular mass represents a molecular expression of these isotopes, where a little signal overlap is present.[80] These restrictions also mean that detection of single nanoparticles proves challenging for CyTOF, while nanoparticle aggregates not associated with cells may be detected, resulting in signal confusion.[76] It should be noted that CyTOF studies with nanoparticles can forgo cell labeling as many inorganic nanoparticles qualify as "probes" for the purposes of detecting cells. However, correlating nanoparticle elemental signal with another cell-associated signal is not possible with this methodology.

CyTOF has been used for immunoassays as well as for human blood cell phenotyping.[87,88] Nanoparticle quantification has also been performed using CyTOF, largely to assess immune cell interaction with silver nanoparticles [74,75,89] and gold nanoparticles.[76] One study by Schulz *et al*. used silver nanoparticles as antigen-labeling agents to quantify antigen presence on peripheral blood leukocytes.[90] Another study by López-Serrano Oliver *et al*. used silver nanoparticles during instrument calibration prior to quantifying silver nanoparticle uptake by THP-1 cells (Figure 2.4B-2.4C).[73] The results of the study suggest that using nanoparticles during calibration allow for greater accuracy in quantifying nanoparticle association with cells compared to ionic calibrations. Nonspecific interactions between nanoparticles and cells has been quantified using CyTOF. Pichaandi et al. treated KG1a human macrophages, THP-1 cells, and Ramos

lymphocytes with different doses of liposome-encapsulated lanthanide nanoparticles. Their results indicated low levels of interaction between the liposome encapsulated nanoparticles and treated cells across different treatment doses and incubation times, demonstrating how CyTOF can quantify nano-bio interactions with low interaction frequency.[91] Finally, in a study by Yang *et al.*, CyTOF has been used to simultaneously perform cell phenotyping of excised C57BL/6 mouse lymph node tissue labeled with a heavy-metal antibody cocktail and treated with gold nanoparticles of varying surface chemistries. Their approach demonstrates the ability of CyTOF to simultaneously identify cell phenotypes and nanoparticle quantification based upon the intensity of isotopic signals.[76]

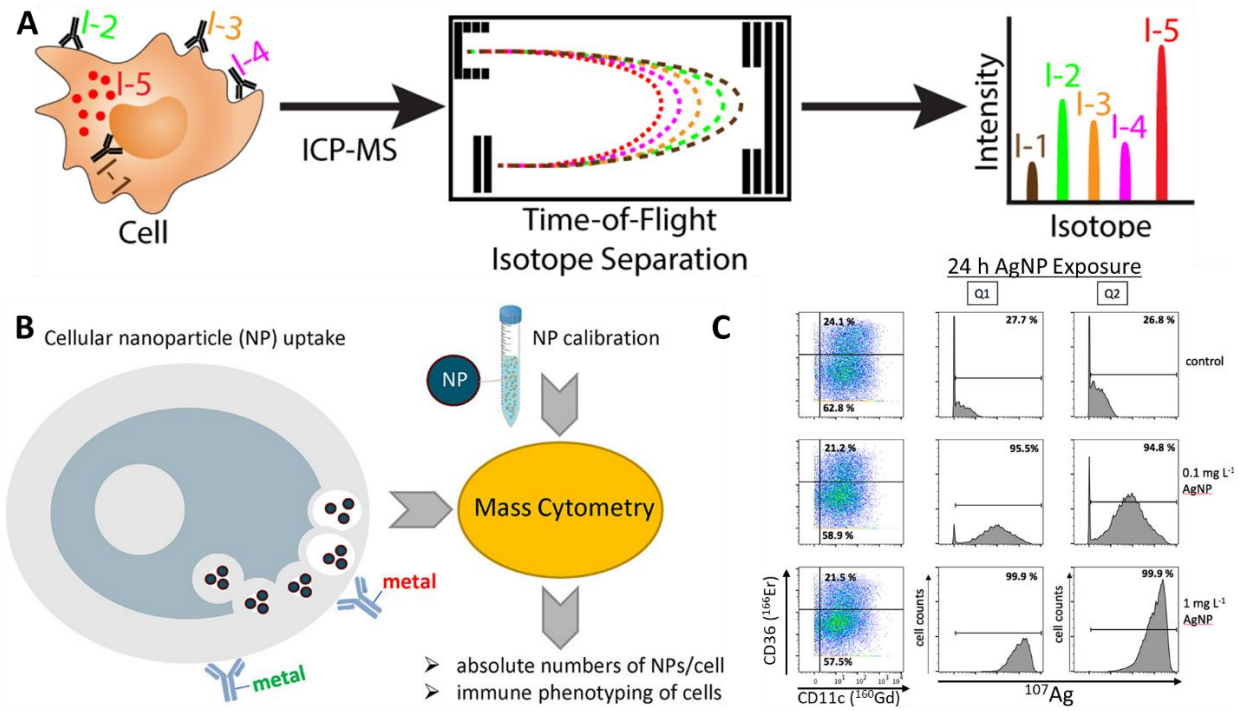

Figure 2.4: CyTOF analysis of single cells. **(A)** Schematic of sample introduction and time-of-flight ion separation during CyTOF measurements. Exogenous isotopes can be detected following uptake by cells or labelling with isotope-tagged antibodies. Transient ion signals are separated based on the difference in *m/z* ratio value between isotopes. **(B)** Cells treated with nanoparticles and tagged with metal-bound antibodies can be measured by CyTOF with a nanoparticle calibration solution to quantify nanoparticle uptake of each individual cell. **(C)** Live CD45+ cells treated with AgNPs are quantified based on different expression of CD36, with AgNP presence indicated with histograms (middle and right columns). Reprinted with permission from Ref. [73]. Copyright 2023 American Chemical Society.

One recent innovation with CyTOF allows for visualization of cells prior to elemental quantification. Imaging CyTOF uses laser ablation with a small laser spot size to enhance spatial resolution, though at the expense of a reduced sensitivity, due to lower ions being collected from each spot.[92,93] Imaging mass cytometry can be used in genomics to examine the *in vitro* uptake and cellular distribution of DNA. For instance, Malile *et al*. used DNA-functionalized gold nanoparticles as probes in imaging CyTOF as only picomolar of nanoparticles were required to be used when compared to conventional flow cytometry.[94]

To compare mass spectrometry techniques for quantifying nanoparticle-cell interactions, one study by Tian *et al*. quantified silver nanoparticle uptake by cyanobacteria using SP-ICP-Q-MS, TOF-ICP-MS, and CyTOF.[85] The study concluded that TOF-ICP-MS is a promising direction for single-cell, single-nanoparticle quantification given its ability to quantify both exogenous nanoparticle elements alongside endogenous cellular elements. SP-ICP-Q-MS performance was poor in comparison due to the single analyte limitations, though it is unclear how the previously discussed dual analyte methods could improve performance in this study. CyTOF performed at a slightly higher level to TOF-ICP-MS in terms of number of detected and paired events but requires the use of additional staining agents to correlate nanoparticle signal with cell signal given the mass cutoff limits of CyTOF filters.[85] The results of this study serve as indicators for the direction of mass spectrometry and elemental analysis research moving forward: TOF-ICP-MS is advantageous given its label-free counting of cells and correlation with nanoparticle events while CyTOF possesses greater accuracy at the cost of requiring cell labeling.

2.5 Conclusions

Analysis of nano-bio interactions at the single-cell level is a promising direction for understanding how nanoparticles can be better engineered for specific cell interactions. Elemental analysis of single cells by way of ICP-MS possesses multiple avenues for single-cell analysis, ranging from relatively affordable SP-ICP-Q-MS methods to more expensive but more informative TOF-ICP-MS. The most limiting factors remain single-analyte restrictions for more conventional single-particle systems (e.g., quadrupole-based mass analyzer systems), complex matrix effects associated with biomedical media and serum, and ion cutoff points preventing endogenous element measurement (e.g., phosphorous). Continued investigations into applications of TOF-ICP-MS with microdroplet systems to circumvent matrix effects associated with complex cell suspensions prove to be potentially valuable to the field. Additionally, the ability for TOF-ICP-MS to measure multiple elements simultaneously, including both endogenous cellular elements and exogenous isotopic labels for cell phenotyping, affords expanded opportunity for analysis of nano-bio interactions and nanoparticle distribution in complex cell or tissue samples. Finally, the combination of flow cytometry and mass spectrometry approaches yields mass spectrometry methods that further expand single cell analysis opportunities. The pairing of imaging methods with existing elemental analysis and mass cytometry methods seems a rational avenue to continue investing in so as to allow for coinciding visual and spectrometry data by which quantification of nanoparticle-cell interactions at the single-cell level may be improved. Finally, improvements to current models and assumptions regarding nanoparticles and cells in single-cell analysis should be considered for obtaining greater quality of data from elemental analysis and ICP-MS

technologies. Overall, the continued investigation into elemental analysis methods for single-cell and single-nanoparticle quantification proves a promising direction that can shape the field of nanomedicine to improve understanding of nano-bio interactions and enhance subsequent patient care.

2.6 Acknowledgements and Funding

This work was supported in part by awards from NIH COBRE (P20GM135009), NSF CAREER (2048130), and OCAST (HR20-106).

Chapter 3 – Quantification of Monodisperse and Biocompatible Gold Nanoparticle by Single Particle ICP-MS

3.1 Abstract

Bioanalytical and biomedical applications often require nanoparticles that exhibit narrow size distributions and biocompatibility. Here, we demonstrate how different synthesis methods affect gold nanoparticle (AuNPs) monodispersity and cytotoxicity. Using single particle inductively coupled plasma mass spectrometry (SP-ICP-MS), we found that the size distribution of AuNPs synthesized with a cetyltrimethylammonium chloride (CTAC) capping was significantly improved compared to AuNPs synthesized with citrate capping agents. We determined an up to 4x decrease in the full width at half maximum (FWHM) value of the normal distributions of AuNP diameter and up to a 12% decrease in relative standard deviation (RSD). While the CTAC-capped AuNPs exhibit narrow nanoparticle size distributions, they are cytotoxic, which limits safe and effective bioanalytical and biomedical applications. We sought to impart biocompatibility to CTAC-capped AuNPs through a PEGylation-based surface ligand exchange. We developed a unique ligand exchange method driven by physical force. We demonstrated the successful PEGylation using various PEG derivatives and used these PEGylated nanoparticles to further bioconjugate nucleic acids and peptides. Using cell viability quantification, we confirmed that the monodisperse PEGylated AuNPs were biocompatible. Our monodisperse and biocompatible nanoparticles may advance safe and effective bioanalytical and biomedical applications of nanomaterials.

This chapter was published in *Analytical and Bioanalytical Chemistry (Anal. Bioanal. Chem.)* – IF 4.478 – as:

Frickenstein A*, Mukherjee S*, Harcourt T, He Y, Sheth V, Wang L, Malik Z, Wilhelm S, "Quantification of Biocompatible Monodisperse Gold Nanoparticles by SP-ICP-MS," *Analytical and Bioanalytical Chemistry,* 2023, https://doi.org/10.1007/s00216-023-04540-x

Author contributions to this work:

Alex Frickenstein* – Project leader, primary experiment coordinator and performer, primary writer

Shirsha Mukherjee* – Assisted with nanoparticle synthesis and surface modification method development

Tekena Harcourt – Assisted with making and characterizing nanoparticles

Yuxin He – Assisted with cell viability and cell uptake studies

Vinit Sheth – Assisted with cell uptake studies and confocal microscopy

Lin Wang – Assisted with cell viability studies

Zain Malik – Assisted with data collection and interpretation

Stefan Wilhelm – Project adviser and corresponding author

* Denotes equal contribution

3.2 Introduction

Probing the interactions between nanoparticles and cells remains a primary focus of bioanalytical and nanomedicine research.[21,95,96] Current investigations have identified that the nanoparticle size and size distributions influence how nanoparticles interact with cells and biological systems.[97-99] The availability of monodisperse and biocompatible nanoparticles is often a prerequisite to enable safe, accurate, and effective applications in research and clinical practice.

Monodisperse nanoparticles are defined by minimal size variation between individual colloidally dispersed nanoparticles. Studies have demonstrated that monodisperse nanoparticles are preferable for improved therapeutic results.[100,101] In particular, gold nanoparticles (AuNPs) are commonly employed given their relative ease of synthesis and surface modification and their inherent biocompatibility.[102] AuNPs are used in bioanalytical and biomedical contexts as model systems for understanding and probing nanoparticle-cell interactions.[20,32,34,103] Additionally, AuNPs have demonstrated a significant ability to serve as carriers for adjuvant delivery or as drivers for photothermal therapy.[104] Further, AuNPs are frequently used for molecular detection and diagnostic assays.[105,106] Given the continued usage of AuNPs, there is a significant need to understand and improve upon the monodispersity of AuNPs used in research and clinical environments leading up to bioanalytical and biomedical applications.

To assess nanoparticles' relative size and colloidal stability, batch characterization methods such as light scattering or spectrophotometry can be used.[107,108] Despite their utility, batch methods do not precisely inform researchers of the differences between nanoparticles on a single-particle basis, making accurate quantification of nanoparticle

monodispersity challenging. Two techniques for individual particle measurements stand out, i.e., transmission electron microscopy (TEM) and single particle inductively coupled plasma mass spectrometry (SP-ICP-MS).[109-111] TEM allows for the exact measuring of individual particle size following appropriate sample preparation and post-imaging analysis. By counting large numbers of nanoparticles, a size distribution is generated that defines nanoparticle monodispersity. SP-ICP-MS techniques are applied in bioanalytical and biomedical studies to characterize nanoparticle mass, size, and concentration or correlating changes in nanoparticles due to solution conditions or biomarker presence.[112-115] SP-ICP-MS performs rapid, continuous measurement of individual nanoparticle mass, generating a mass distribution from collected data. The wider the mass distribution, the more polydisperse the nanoparticle sample is. We have previously demonstrated how SP-ICP-MS may be used to assess changes in nanoparticle aggregation and chemical composition based on changes in mass distribution, indicating the ability of SP-ICP-MS to measure differences in mass distributions effectively.[116,117] The high-throughput and continuous nature of SP-ICP-MS makes analysis rapid while maintaining high accuracy given its single-particle resolution.

In this study, we demonstrate how AuNPs synthesized between two different methods differ in their monodispersity. From reviewing several reports using AuNPs, we observed an apparent difference in the size distribution between large (>10 nm) citrate-capped AuNPs and AuNPs capped with cetyltrimethylammonium chloride (CTAC).[118,119] If CTAC-capped AuNPs possess a better monodispersity compared to citrate-capped AuNPs, CTAC-capped AuNPs may prove more useful in bioanalytical and biomedical applications.[101] We synthesized citrate-capped and CTAC-capped AuNPs

of various diameters and characterized them extensively. Notably, SP-ICP-MS measures were collected to verify any differences in mass, and thus size, distribution between AuNPs. Through this, we demonstrate how SP-ICP-MS techniques can be effectively applied to analyze differences in mass distribution between nanoparticle populations.

It is, however, well known that CTAC is cytotoxic and thus unfit for many applications in bioanalytical and biomedical settings.[120,121] To overcome this challenge, we implemented a unique physical replacement method that imparts biocompatibility to CTAC-capped AuNPs, increasing their bioanalytical and biomedical relevance. Using SP-ICP-MS quantification, we demonstrated that our physical replacement method did not change the mass distribution of CTAC-capped AuNPs. Finally, we showed how through conjugating the appropriate ligand during our physical replacement method, CTAC-capped AuNPs could be made bio-functional by conjugating thiolated nucleic acids or peptides. Further, we performed cell uptake experiments to find that when surface chemistries are matched, CTAC-capped AuNPs demonstrate similar performance to citrate-capped AuNPs, which are more commonly used in bioanalytical and biomedical contexts.

Our study shows the significant difference between the monodispersity of AuNPs synthesized by different methods. Further, we demonstrate how SP-ICP-MS is a valuable tool for quantifying and comparing the monodispersity between nanoparticle populations. Additionally, we illuminate how physical replacement methods of nanoparticle surface ligands may be applicable for improving the biocompatibility of highly monodisperse CTAC-capped AuNPs. The combination of our findings offers new means by which highly

monodisperse AuNPs may be synthesized, characterized, and surface modified for downstream use in bioanalytical and biomedical applications.

3.3 Experimental Section

A complete list of the materials and instruments used in this study can be found in the Electronic Supplementary Material (ESM, Appendix B).

3.3.1 Synthesis of Gold Nanoparticles by Different Methods

All gold nanoparticle synthesis was performed in glassware cleaned by Aqua Regia, comprised of a 3:1 v/v ratio of hydrochloric acid and nitric acid. Fourteen-nanometer citrate-capped AuNP seeds were synthesized according to the Frens/Turkevich method, whereby ionic gold is reduced into solid gold via citrate at high temperatures.[122] These 14-nm seeds were used to grow larger quasi-spherical AuNPs based on methods developed by Perrault and Chan.[118] By varying the molar ratio of $HAuCl_4$ to 14-nm AuNP seeds, the final size of grown AuNPs could be controlled (Table D3.1). This method targeted the synthesis of AuNPs of diameters 30 nm, 45 nm, and 60 nm. The AuNPs were purified by centrifugation after growth and resuspended in a 0.01% citrate, 0.1% Tween20 solution before characterization and surface modification.

The CTAC-capped AuNPs were synthesized using previously developed methods.[119,123,124] First, gold clusters were synthesized by reducing Au^{3+} ions with $NaBH_4$ in a concentrated cetyltrimethylammonium bromide (CTAB) solution. These clusters were then used to synthesize 10-nm CTAC-capped AuNPs needed to grow larger CTAC-capped AuNPs. The growth process for CTAC-capped AuNPs differs from that of citrate-capped AuNPs as it uses CTAC as the stabilizing agent and ascorbic acid at 35°C as the reducing agent. Further, the precursor Au^{3+} ions were added dropwise via a syringe pump setup. The size of grown AuNPs was predicted by controlling the moles of seeds used in the growth reaction (see Table D3.2). The CTAC-capped AuNPs of 15-nm, 30-

nm, 45-nm, and 60-nm target diameters were synthesized using these methods. Following growth, CTAC-capped AuNPs were purified by centrifugation and resuspended in 20-mM CTAC solution before characterization and surface modification. For more details on the AuNP synthesis methods, see the ESM (Appendix B).

3.3.1 Nanoparticle Characterization

Initial characterization of the synthesized AuNPs was performed using dynamic light scattering (DLS), ultraviolet-visible spectrophotometry (UV-Vis), and transmission electron microscopy (TEM). The DLS techniques measured the hydrodynamic diameter and surface zeta potential of the synthesized AuNP before and after surface modification. These measurements also provided an initial indication of polydispersity through the polydispersity index (PDI) value. Generally, nanoparticles possessing a PDI<0.1 are colloidally stable and monodisperse; this arbitrary metric was considered when evaluating synthesis success. The UV-Vis measurements were used to determine the extinction spectrum of each nanoparticle dispersion and to estimate the nanoparticle molar concentrations.[118] We further prepared TEM micrographs of the synthesized AuNPs and collected TEM images of each AuNP population. Images were analyzed using ImageJ, and typically >150 AuNPs were counted and measured to determine the distribution of AuNP diameters for a given synthesized nanoparticle population.

3.3.3 SP-ICP-MS Measurements of Synthesized Gold Nanoparticles

Recently, we have demonstrated how SP-ICP-MS is useful for accurately and rapidly measuring nanoparticle mass and size distributions.[21,116,117] In the current study, we used SP-ICP-MS to identify the mass distribution of synthesized AuNPs and corroborate the size distribution data observed from our TEM imaging studies. All measurements were collected using a PerkinElmer NexION 2000 ICP-MS with a high-efficiency sample-introduction system comprised of a nebulizer, spray chamber, and a heating element wrapped around the spray chamber. The heating element limits condensation on the interior of the spray chamber, improving the transport efficiency (TE) of introduced AuNPs. We optimized the instrument settings for SP-ICP-MS measurements (see Table D3.3). We measured the TE using commercially available Lu175-doped polystyrene beads and found the TE to be ~70%. Using a set of AuNP standards of known diameter, we created a particle calibration that correlated Au^{3+} signal intensity to Au mass in attograms (ag), allowing for immediate translation of the intensity of individual Au events into an estimated particle mass. Prior to measurements of prepared samples, we significantly diluted the AuNPs to ~$3x10^{-16}$ M in nanopure water to minimize matrix effects between samples and to minimize any potential signal overlap that would result from multiple AuNPs being detected simultaneously.[125-127] Dilute AuNPs were then introduced into the instrument via a microfluidic introduction system, and correlating mass distributions were collected. We then translated the mass distribution of each AuNP into a correlating size distribution to gain further insights into the monodispersity of the measured AuNPs.

3.3.4 PEGylation of Gold Nanoparticles

Modifying the surface of citrate-capped AuNPs with thiolated or disulfide-modified PEG ligands was performed according to prior methods.[128] Room temperature incubation of AuNPs in a solution of PEG and Tween20 for 30 min. was sufficient to complete PEGylation of the AuNP surface. A PEG density of 7 PEG/nm^2 was targeted for each PEGylation procedure. Note: seven PEG per nanoparticle surface area in nm^2 unit is the amount of PEG molecules added to the citrate-capped AuNPs.

The PEG molecules, however, do not readily bind to the surface of CTAC-capped molecules and therefore require an alternative conjugation method. Our approach was inspired by prior studies using physical methods to displace cetyltrimethylammonium-based positively charged ligands from gold-based nanomaterials.[129,130] In this "physical replacement" method, CTAC-capped AuNPs are spun down into concentrated pellets via centrifugation. The supernatant is removed, and the pellet is suspended in 50 µL of a concentrated solution of PEG in 0.1% Tween20. The solution is sonicated for 1 minute and then vortexed vigorously for 30 s. The resulting AuNP solutions were then diluted to 1 mL in a 0.1% Tween20 solution before purification by centrifugation. This process was repeated twice for three iterations of sonication, vortexing, and centrifugation. The concentration of PEG used at each step was such that after the three repetitions of the process, the final added PEG amount would be 7 PEG/nm^2.

We characterized all PEGylated AuNPs by DLS to affirm PEG presence. Further, we collected zeta potential measurements of pre- and post-PEGylation AuNPs to demonstrate successful surface charge changes. We also performed UV-Vis and SP-ICP-MS measurements of AuNPs to ascertain how our "physical replacement" method

may induce changes in AuNP extinction spectra or mass distribution. For more details on PEGylation methods, see the ESM (Appendix B).

3.3.5 Biofunctionalization Via Maleimide-Thiol Conjugation

Previous studies have demonstrated that conjugating PEG with maleimide functional groups can be used to conjugate thiolated ligands to the surface of nanoparticles.[128,131] Applying this technique to CTAC-AuNPs would increase the versatility of these monodisperse model nanoparticles beyond PEG functional groups. Thus, as described, we performed PEGylation of 60-nm CTAC-capped AuNPs using 5-kDa maleimide PEG-OPSS (malPEG) and confirmed the PEG presence using DLS measurements. After centrifuging PEGylated AuNPs to remove any excess malPEG, the resulting AuNP pellet was dispersed in a concentrated solution of either thiolated peptide K7C (amino acid sequence of KKKKKKKC) or thiolated single-stranded DNA (ssDNA) molecules (see Table D3.4). We selected these ligands based on prior studies.[128,132,133] For ssDNA and K7C, the concentration of ligands in solution added to malPEG-AuNPs was such that there would be a maximum of 7 ligand molecules per nm^2 on the AuNP surfaces. After allowing the mixture to incubate overnight at room temperature, we took DLS measurements to confirm changes in hydrodynamic diameter associated with the conjugation of K7C or ssDNA.

We performed additional experiments depending on the ligand conjugated to confirm successful conjugation via maleimide-thiol click chemistry further. For K7C, *in vitro* experiments using various cell lines were performed. For ssDNA, we created DNA-AuNP superstructures by conjugating ssDNA of two different sequences to either 60-nm or 15-nm diameter AuNPs. The conjugated ssDNA is complementary to different sections of a third “linker” ssDNA strand. After washing off excess ssDNA, one DNA-AuNP population would be hybridized to the linker through previously defined methods.[132] We

centrifuged the resulting linker-DNA-AuNP complex multiple times to remove excess linker ssDNA strands. Then, we introduced the other DNA-AuNP population, which binds to the other available section of the linker, forming a “core-satellite” AuNP-DNA-AuNP superstructure. The resulting superstructures were characterized by DLS and TEM. For more details on maleimide-thiol conjugation steps, see the ESM (Appendix B).

3.3.6 Cell Viability of PEGylated Gold Nanoparticles

To verify the complete removal of cytotoxic CTAC from the CTAC-capped AuNPs via our unique physical replacement approach, we performed commercially available XTT viability assays for DC2.4 murine dendritic cells and RAW 264.7 murine macrophages. Ninety-six-well plates with either 10,000 DC2.4 cells/well or 22,000 RAW 264.7 cells/well were prepared in appropriate media and treated with 0.1 nM of 60-nm AuNPs in media and incubated for 24 h. The AuNP groups included citrate-capped AuNPs, CTAC-capped AuNPs, and citrate- and CTAC-capped AuNPs that underwent their respective PEGylation methods. Media-only and cell-only wells were included for negative controls. Following treatment incubation, an XTT cell viability assay was performed on all wells, and absorbance was measured to assess relative cell viability according to the manufacturer's instructions. For more details on cell culturing and XTT viability assay methods used, see the ESM (Appendix B).

3.3.7 Cell Uptake of Biofunctionalized Gold Nanoparticles

The K7C peptide is a model positively-charged biomolecule that has been reported to increase AuNP uptake in cells.[21,128] We sought to demonstrate that CTAC-capped AuNPs modified with malPEG and conjugated to K7C would demonstrate similar uptake results compared to citrate-capped AuNPs of the same surface chemistry. We first affirmed our malPEG-K7C AuNP conjugates maintained biocompatibility via an XTT viability assay using RAW 264.7 murine macrophages. PEGylated or malPEG-K7C AuNPs synthesized by citrate-capped or CTAC-capped methods (4 total groups) treatments in media (0.1 nM) were added to 22,000 cells/well and incubated for 3 h. The CTAC molecules were used as positive controls for this experiment, and results were compared to media-only and cell-only negative controls. Following incubation, wells were treated with XTT viability agents, and absorbance was measured.

Based on the XTT viability results, we sought to assess the uptake of our AuNPs by RAW 264.7 murine macrophages using confocal laser scanning microscopy (CSLM) and ICP-MS. For CLSM, 0.01 nM of AuNPs in media were used to treat 15,000 cells/well in 24-well plates with coverslips. This lower AuNP concentration was selected as it would not impact cell viability and would limit the saturation of the scattering signal from CSLM. After 3 h of incubation, coverslips were stained to fluorescently tag cell membranes and nuclei according to previously defined methods.[21] Coverslips were then imaged using a ZEISS LSM 880 inverted CLSM. The AuNPs were detected by light scattering from the laser.[21,32]

Cell uptake of AuNPs was measured using previously defined ICP-MS methods.[32] Briefly, RAW 264.7 cells were seeded in a 48-well plate with 200,000

cells/well and treated with 0.01 nM AuNPs in media. The lower AuNP concentration was selected to limit the possibility of saturating the ICP-MS detector. After 3 hours, wells were rapidly washed once with a dilute gold etchant (KI/I_2) solution to remove any AuNPs not internalized by cells.[21,32] Then, wells were washed with 1xPBS, and the well contents were digested in 500 µL aqua regia (4:1 v/v HNO_3:HCl). The digested solution (125 µL) was diluted in nanopure water and measured using standard ICP-MS to measure the Au content of each sample. The Au intensity signal was compared against the Mg intensity signal used to estimate the cell number, and calibration curves for both ions were used to calculate the number of AuNPs and the number of cells in each sample. To account for any AuNPs stuck to well plates, the same process was performed on a plate with no cells using the same AuNP treatments, incubation time, and wash steps. The ICP-MS signal from these wells was subtracted from the signal from the cell data, so only cell-associated AuNPs were counted. For more details on methods used for CSLM and ICP-MS preparation and data collection, see the ESM (Appendix B).

3.4 Results and Discussion

3.4.1 Mass and Size Distributions of Gold Nanoparticles

We synthesized AuNPs by the citrate-capping and CTAC-capping methods and initially characterized AuNPs by DLS, UV-Vis, and TEM (Figure 3.1). To synthesize CTAC-capped AuNPs, we followed the multi-step process reported in prior studies and characterized both the Au-clusters (Figure C3.1) and the 10-nm CTAC-capped AuNP seeds (Figure C3.2).[119,124] For DLS data of synthesized AuNPs, it is important to consider that the diameter reported is the hydrodynamic diameter, which includes surface ligands and behavior that influence particle Brownian motion.[134] Thus, hydrodynamic diameter estimates are typically larger than the desired or expected AuNP diameter. With this consideration, we observed that the hydrodynamic diameter estimates align with our targeted AuNP diameter during synthesis (Figure 3.1a-3.1b).

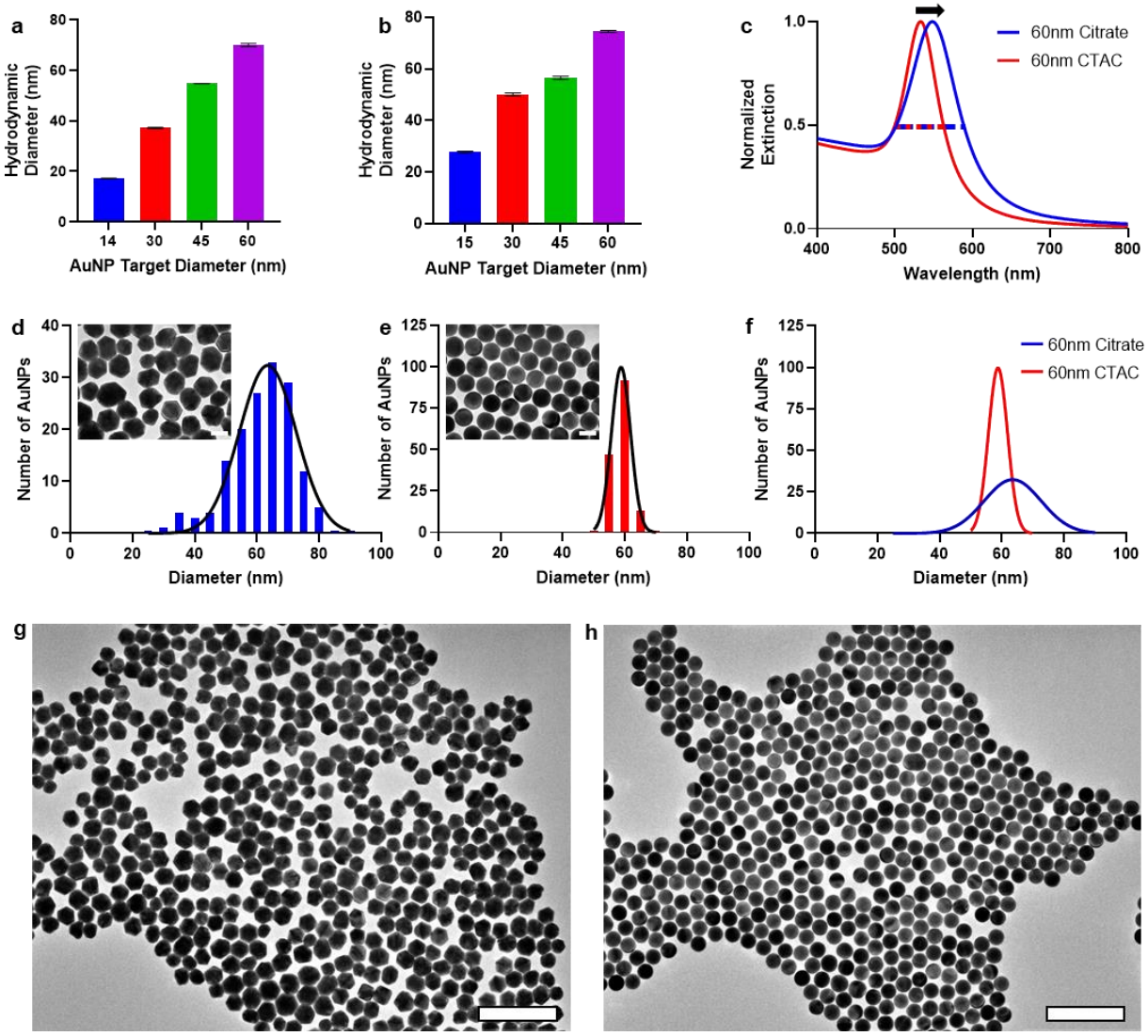

Figure 3.1: Physicochemical characterization of synthesized AuNPs. **a)** DLS measurements of synthesized citrate-capped AuNPs. **b)** DLS measurements of synthesized CTAC-capped AuNPs. Colored bars for 1a and 1b represent the measured mean hydrodynamic diameter for synthesized AuNPs of different target diameters. Error bars for 1a and 1b show standard deviation from N=3 measurements. **c)** The UV-Vis extinction spectrum for 60-nm diameter citrate-capped AuNPs differs from that of the UV-Vis extinction spectrum for CTAC-capped AuNPs of the same diameter. **d-e)** TEM micrograph images and size distributions of 60-nm diameter citrate-capped and CTAC-capped AuNPs. Colored bars indicate the number of AuNPs (i.e., frequency) of each diameter listed on the x-axis. Black lines indicate the Gaussian normal distribution. Size distributions were normalized to N=150 AuNPs for each distribution. The scale bar is 50 nm. **f)** Overlay of the Gaussian normal distributions for 60-nm AuNPs by both capping methods demonstrating the difference in particle size distribution height and width. **g-h)** Low magnification TEM micrographs of 60-nm diameter citrate- and CTAC-capped AuNPs, respectively. The scale bar is 300 nm.

The UV-Vis characterization can further indicate AuNP size and stability based on the nanoparticles' surface plasmon resonance. Additionally, UV-Vis extinction spectral analysis is useful for estimating AuNP concentration. The Beer-Lambert Law is a valuable method for estimating AuNP molar concentrations based on measured UV-Vis extinction spectra of the AuNP colloidal dispersions.[118] This remains the case for CTAC-synthesized AuNPs. Despite the difference in UV-Vis spectra between citrate- and CTAC-synthesized AuNPs (Figure C3.3), we applied the Beer-Lambert Law for calculating the nanoparticle concentration given that a primary driver of differences in the AuNP molar extinction coefficient is size.[118] Interestingly, the peak extinction wavelength and spectral width of all synthesized CTAC-capped AuNPs differed from citrate-capped AuNPs of the same size in that CTAC-capped AuNPs possessed a lower peak extinction wavelength and a narrower spectral width (Figure 3.1c, Table 3.1). We attribute this phenomenon to how nanoparticle size and size distributions contribute to extinction.[135,136] For citrate-capped AuNPs, a greater proportion of AuNPs is larger than the target diameter, as shown by the TEM size distributions (Figure 3.1d-3.1e, Figure C3.4). The larger particles in the citrate-capped AuNP population may contribute substantially to the overall extinction spectrum, resulting in a red shift of the peak extinction wavelength and the spectrum width. By comparison, CTAC-capped AuNPs possess AuNPs that are primarily of the target diameter, minimizing "off-target" extinction. Our observations of the difference in extinction spectra indicate the AuNPs initially synthesized to be CTAC-capped may prove useful in bioanalytical and biomedical applications that could rely on small changes in extinction spectra to identify molecule presence[106] or solution conditions.[117]

We collected TEM micrographs of each particle population to quantify AuNP size distributions (Figure 3.1d-3.1f, Figure C3.4). Before measuring size distributions, we observed a striking difference in AuNP shape and monodispersity by TEM (Figure 3.1g-3.1h). We attribute this difference primarily to how Au^{3+} ions are reduced onto the surface of the precursor AuNP

seeds and the differing surface chemistries of the precursor AuNP seeds. For CTAC-capped AuNPs, Au^{3+} ions are added dropwise to the reaction solution, permitting gradual AuNP growth. Further, the bilayer nature of the amphiphilic CTAC molecules on the surface of the AuNPs as they grow serves to maintain a spherical AuNP shape. By comparison, the rapid nature by which Au^{3+} is added for citrate-capped AuNPs as well as the less constraining nature of citrate on the surface of precursor AuNPs results in quasi-spherical AuNPs of a wider shape and size variety.

In addition to calculating the approximate mean diameter values for each particle population using ImageJ, we applied a normal Gaussian distribution to the diameter distribution to assess the relative polydispersity. We quantified polydispersity through measuring the full width at half maximum (FWHM) of each distribution according to Equation 3.1:

$$FWHM \approx 2.355 * \sigma \qquad Equation\ 3.1$$

Where σ is the standard deviation of the Gaussian normal distribution.

This quantification of nanoparticle polydispersity is used in the literature and provides insight into the relative size differences between nanoparticles in solution.[101] For each target size except the 14-nm citrate-capped and 15-nm CTAC-capped AuNPs, there is an evident difference in the FWHM values (Table 3.1). Namely, the FWHM values for CTAC-capped AuNPs are lower than that of citrate-capped AuNPs by up to four times. Interestingly, we observed that the difference in FWHM values becomes more apparent with increasing AuNP diameter. The larger the target AuNP diameter, the more monodisperse the CTAC-capped AuNPs are compared to the citrate-capped AuNPs. We demonstrate this phenomenon clearly in Figure 1f.

As another metric for nanoparticle monodispersity, we calculated the relative standard deviation (RSD) using Equation 3.2:

$$RSD = \frac{100 * \sigma}{\mu} \qquad Equation\ 3.2$$

Where RSD is reported as a perfect (%) value and μ is the mean diameter of the normal distribution for the nanoparticle population. The RSD values are often used to assess nanoparticle monodispersity, with lower RSD values indicating a greater degree of monodispersity.[101,137] For each comparison between citrate-capped and CTAC-capped AuNPs, we found that the RSD value was lower for the CTAC-capped AuNPs than for the citrate-capped AuNPs. The magnitude of the difference was as high as ~12%, with the difference increasing directly with AuNP diameter. These RSD trends align with those observed from the FWHM observations, further corroborating the improved monodispersity of CTAC-capped AuNPs compared to citrate-capped AuNPs.

Table 3.1: Physicochemical characterization results for synthesized AuNPs.

Target AuNP Diameter (nm)	Synthesis Method	Hydrodynamic Diameter[#] (nm)	Polydispersity Index[#] (PDI)	Peak Extinction Wavelength (nm)	TEM AuNP Diameter[#] (nm)	TEM FWHM	TEM RSD (%)
14	Citrate	17.2 ± 0.1	0.02 ± 0.02	518	13.1 ± 1.2	2.8	9.0
30	Citrate	37.2 ± 0.2	0.05 ± 0.02	525	29.2 ± 5.3	12.5	18.1
45	Citrate	54.8 ± 0.0	0.08 + 0.01	533	46.3 ± 6.5	15.3	14.1
60	Citrate	70.0 ± 1.0	0.08 + 0.01	548	62.1 ± 9.7	22.7	15.5
15	CTAC	27.7 ± 0.4	0.09 ± 0.01	527	15.3 ± 1.1	2.7	7.4
30	CTAC	50.1 ± 0.6	0.05 + 0.02	526	35.5 ± 3.3	7.7	9.2
45	CTAC	56.5 ± 0.6	0.02 + 0.01	526	42.2 ± 1.5	3.6	3.7
60	CTAC	74.5 ± 0.4	0.04 + 0.02	533	59.3 ± 2.4	5.6	4.0

[#] Mean value ± standard deviation.

Imaging with TEM is limited in its ability to characterize numerous nanoparticles in a high-throughput manner. To overcome this limitation, we performed quantitative SP-ICP-MS analysis to provide additional insight into the mass and size distributions for synthesized AuNPs. We used an AuNP calibration curve made by measuring synthesized AuNP standards to correlate individual event ion signals with AuNP mass distributions (Figure C3.5). With this calibration curve, accurate mass distributions for all AuNPs were generated (Figures 3.2a-3.2c, Figure C3.6). The SP-ICP-MS technique measures the mass of individual particles, which we converted into an estimated AuNP diameter by assuming a spherical AuNP (Equation 3.3).

$$D = \sqrt[3]{\frac{6 * m}{\pi * \rho}} \qquad Equation\ 3.3$$

In Equation 3.3, *D* is the calculated AuNP diameter, *m* is the particle mass as measured by SP-ICP-MS, and *ρ* is the density of the particle composite material ($\rho = 19.3 \frac{g}{cm^3}$ for Au).

From the mass distributions measured by SP-ICP-MS and using Equation 3.3, we estimated the apparent size distributions for each AuNP population (Figures 3.2d-3.2e, Figure C3.7).

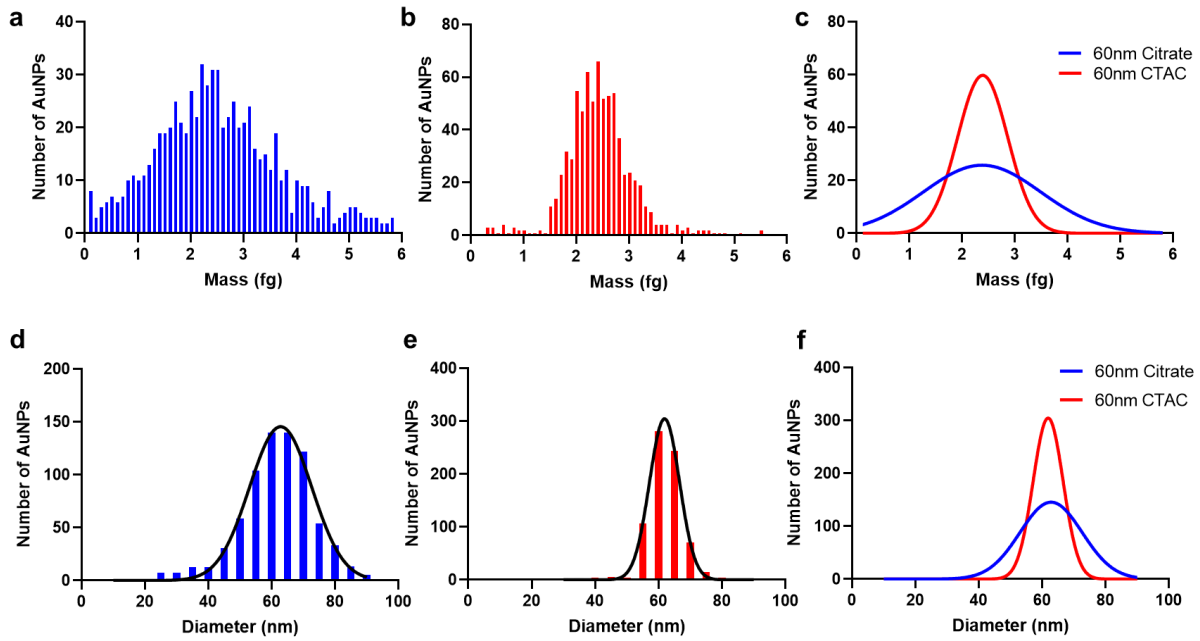

Figure 3.2: SP-ICP-MS characterization of synthesized 60-nm diameter AuNPs. a-b) Mass distributions of 60-nm diameter citrate-capped and CTAC-capped AuNPs. Colored bars indicate the number of AuNPs at each mass on the x-axis. Distributions were normalized to N=750 AuNPs. **c)** Overlay of Gaussian normal mass distributions of synthesized 60-nm diameter AuNPs demonstrating differences in distribution height and width. **d-e)** Measured mass distributions were converted into diameter distributions using Equation 3. Colored bars indicate the number of AuNPs of each diameter n the x-axis. Black lines indicate the Gaussian normal distribution. **f)** Overlay of Gaussian normal diameter distributions of synthesized 60-nm diameter AuNPs demonstrating differences in distribution height and width.

The results from SP-ICP-MS corroborate those found in TEM, i.e. CTAC-capped AuNPs possess tighter mass distributions compared to citrate-capped AuNPs. Further, we observed that the general FWHM and RSD trends from the TEM analysis are similar to those seen in the SP-ICP-MS mass and size distributions (Table 3.2). CTAC-capped AuNPs generally possess lower FWHM and RSD values. We noted an exception to the previous TEM data in the case of the citrate-capped 14-nm AuNPs and the CTAC-capped 15-nm AuNPs, where the mean diameter along with the FWHM and RSD values and trends are all different from those found by TEM. We attribute these results to the fact that these particles are small enough to push the limit of detection of SP-ICP-MS instrumentation and methods.[127,138]

Table 3.2: SP-ICP-MS characterization results for synthesized AuNPs.

Target AuNP Diameter (nm)	Synthesis Method	Mean Mass[#] (ag)	Mass FWHM	Mass RSD (%)	Mean Calculated Diameter[#] (nm)	Diameter FWHM	Diameter RSD (%)
14	Citrate	39 ± 2	4.2	4.6	16.7 ± 0.8	1.9	4.8
30	Citrate	251 ± 169	397.5	67.2	30.1 ± 6.0	14.2	20.1
45	Citrate	923 ± 527	1241.1	57.1	45.9 ± 8.9	21.0	19.4
60	Citrate	2379 ± 1114	2623.5	46.8	62.8 ± 9.8	23.1	15.6
15	CTAC	67 ± 18	42.6	27.1	18.8 ± 1.8	4.2	9.6
30	CTAC	379 ± 133	312.3	35.0	34.5 ± 4.7	11.1	13.6
45	CTAC	681 ± 144	339.1	21.1	40.6 ± 3.2	7.5	7.9
60	CTAC	2391 ± 476	1121.0	19.9	61.9 ± 4.7	11.1	7.6

[#] Mean value ± standard deviation.

Thus, from both TEM and SP-ICP-MS characterization of the nanoparticles, we see that AuNPs synthesized using the CTAC-capping method possess a greater degree of monodispersity (i.e. narrower mass/size distribution) in comparison to AuNPs synthesized using the citrate-capping method.

3.4.2 Surface Modification of Gold Nanoparticles

While our comparisons of monodispersity promote the use of CTAC-capped AuNPs for bioanalytical and biomedical applications, additional steps must be taken to remove the cytotoxic effects CTAC imposes on these AuNPs. PEGylation is a commonly applied method to improve nanoparticle stability and biocompatibility in biological environments.[139,140] We performed PEGylation of AuNPs as previously described. We incubated citrate-capped AuNPs with PEG at room temperature while we PEGylated the CTAC-capped AuNPs using our unique physical replacement approach. The CTAC interactions with AuNPs occur via electrostatic interactions between the positively charged CTAC molecules and the AuNP surface. In our physical replacement approach, CTAC is replaced by PEG molecules that covalently bind to the gold surface through Au-S interactions.[141,142] With repeated washing of AuNPs and introduction of PEG in multiple steps, all CTAC is effectively removed and replaced with biocompatible PEG molecules covalently bound to the AuNP surface (Figure 3.3a).

We confirmed the successful conjugation of mPEG-SH based on our DLS measurements, indicating an increase in hydrodynamic diameter (Figure 3.3b and Table 3.3). We attempted to confirm the PEG layer presence through TEM imaging of negatively stained AuNPs, but there was no apparent difference between CTAC-capped AuNPs before or after PEGylation (Figure C3.8). However, zeta-potential quantification further confirmed the presence of PEG on the AuNP surface (Figure 3.3d). It is known that CTAC-capped AuNPs possess a positive surface charge due to the CTAC on the surface of the AuNPs.[130] Following PEGylation by our physical replacement method, we observed that zeta potential measurements indicated a shift towards neutral charge values associated

with mPEG-SH. Remarkably, our physical displacement PEGylation process did not result in a significant change in the UV-Vis extinction spectrum (Figure 3.3e) or mass distribution of AuNPs as measured by SP-ICP-MS (Figure 3.3f), thus demonstrating that our technique does not change the monodispersity of AuNPs.

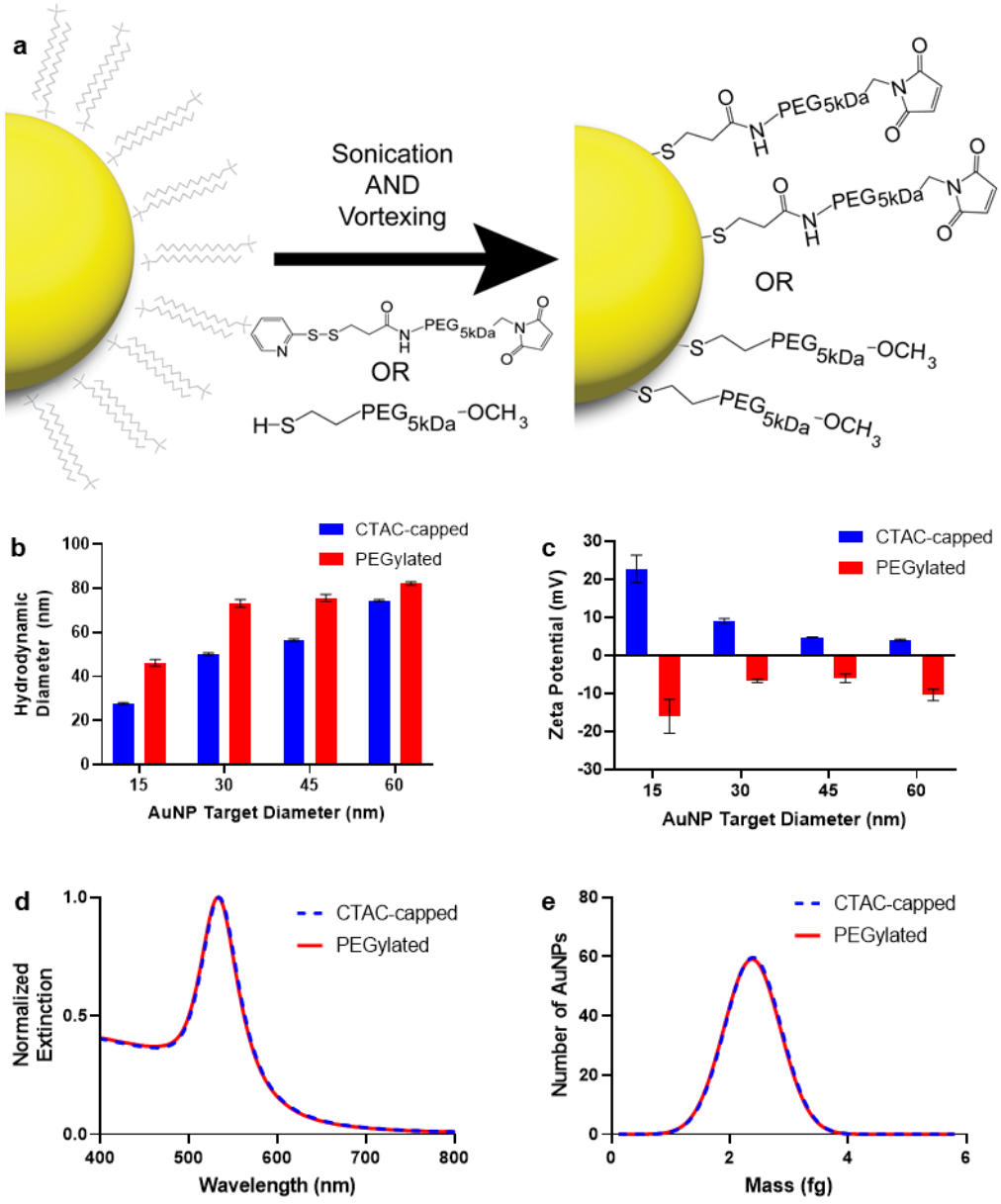

Figure 3.3: PEGylation of CTAC-capped AuNPs is possible by applying physical force. a) Schematic demonstrating the transition from CTAC-capped to PEG-conjugated AuNP surface chemistry using either 5-kDa mPEG-SH or 5-kDa malPEG-OPSS. **b)** DLS data demonstrating an increase in hydrodynamic diameter following PEGylation of CTAC-capped AuNPs with 5-kDa mPEG-SH. Error bars indicate the standard deviation for three measurements. **c)** Zeta potential measurements of CTAC-capped AuNP before and after PEGylation. Error bars indicate the standard deviation for three measurements. **d)** UV-Vis extinction spectra of 60-nm diameter CTAC-capped AuNPs before and after PEGylation, demonstrating no change in extinction from PEGylation. **e)** SP-ICP-MS Gaussian normal distribution of 60-nm diameter CTAC-capped AuNPs before and after PEGylation, demonstrating no change in the mass distribution from PEGylation. Mass distributions were normalized to N=750 AuNPs.

Having demonstrated our physical replacement PEGylation method was successful, we sought to expand the possible surface chemistries available to CTAC-capped AuNPs. Previously, we have shown how maleimide PEG-OPSS (malPEG-OPSS) can be used to conjugate thiolated peptides onto the surface of AuNPs.[128] We applied our physical replacement method using malPEG-OPSS and incubated the PEGylated AuNPs overnight with thiolated molecules. Specifically, we performed this first with thiolated single-stranded DNA. We deemed conjugation successful based on increased hydrodynamic diameter as measured by DLS (Figure 3.4a, Table 3.3). We selected single-stranded DNA (ssDNA) strands for our investigation on the basis that they could form DNA-AuNP superstructures as seen in other studies (Table D3.3).[132,133] Using established protocols, we created similar DNA-AuNP superstructures using 60-nm diameter AuNPs and 15-nm diameter AuNPs, as evidenced by both DLS and TEM data (Figure 3.4b-3.4c). These results demonstrated how CTAC-capped AuNPs could be made bio-functional with nucleic acids by using PEGylation with malPEG-OPSS and then conjugating thiolated DNA strands to the surface.

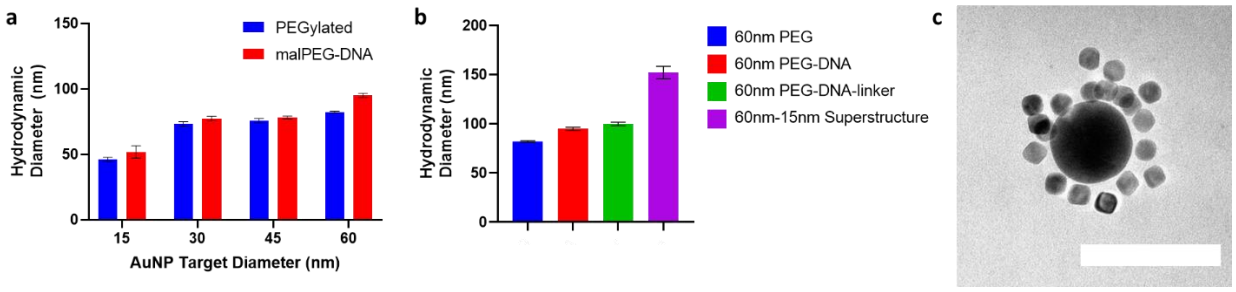

Figure 3.4: DNA conjugation to malPEG on the surface of CTAC-synthesized AuNPs. **a)** DLS data of CTAC-capped AuNPs following PEGylation with 5-kDa malPEG-OPSS PEG and overnight incubation with thiolated DNA oligos. AuNPs of 15-45-nm diameters were conjugated to DNA strands having the OligoB sequence, while 60-nm diameter AuNPs were conjugated to DNA strands having the OligoA sequence. **b)** DLS data of 60-nm CTAC-capped AuNPs after PEGylation with 5-kDa malPEG-OPSS PEG, overnight conjugation with OligoA, hybridization with the "linker" strand, and conjugation to 15-nm AuNP conjugated to malPEG-OligoB. For 4a and 4b, colored bars represent mean hydrodynamic diameter values from N=3 measurements. Black error bars represent the standard deviation from three measurements. **c)** TEM micrograph of resulting final DNA-AuNP superstructure. The scale bar is 100 nm.

Table 3.3: DLS results of nanoparticles with PEG and PEG-biomolecule conjugation.

Nanoparticle Sample	Hydrodynamic Diameter[#] (nm)	Polydispersity Index[#] (PDI)
15-nm CTAC mPEG	46.2 ± 1.5	0.06 ± 0.04
15-nm CTAC malPEG-DNA	51.8 ± 4.7	0.10 ± 0.04
30-nm CTAC mPEG	73.2 ± 1.7	0.02 ± 0.01
30-nm CTAC malPEG-DNA	77.2 ± 1.8	0.05 ± 0.01
45-nm CTAC mPEG	75.7 ± 1.6	0.02 ± 0.01
45-nm CTAC malPEG-DNA	78.1 ± 1.1	0.04 ± 0.04
60-nm CTAC mPEG	82.2 ± 0.8	0.03 ± 0.02
60-nm CTAC malPEG-DNA	94.9 ± 1.6	0.03 ± 0.02
60-nm CTAC malPEG-DNA-linker	99.9 ± 1.8	0.03 ± 0.02
60-nm CTAC Superstructure	152.0 ± 6.4	0.09 ± 0.05
60-nm CTAC malPEG-K7C	90.6 ± 0.6	0.05 ± 0.03

[#] Mean value +/- standard deviation.

3.4.3 Biocompatibility and Cell Uptake of AuNPs

Next, we investigated if our method imparts biocompatibility to the originally CTAC-capped and thus cytotoxic AuNPs. We ran XTT-based cell viability assays with DC2.4 murine dendritic cells (Figure 3.5a) and RAW 264.7 murine macrophages (Figure 3.5b) following incubation with 60-nm AuNPs for 24 hours. Our CTAC-synthesized AuNPs PEGylated with mPEG-SH demonstrated a significantly higher degree of cell viability than as-synthesized CTAC-capped AuNPs in both cell lines. Thus, we confirmed that our method is not only successful in conjugating PEG to the surface of originally CTAC-capped AuNPs, but also that our process removes any cytotoxic CTAC from the surface of the AuNPs.

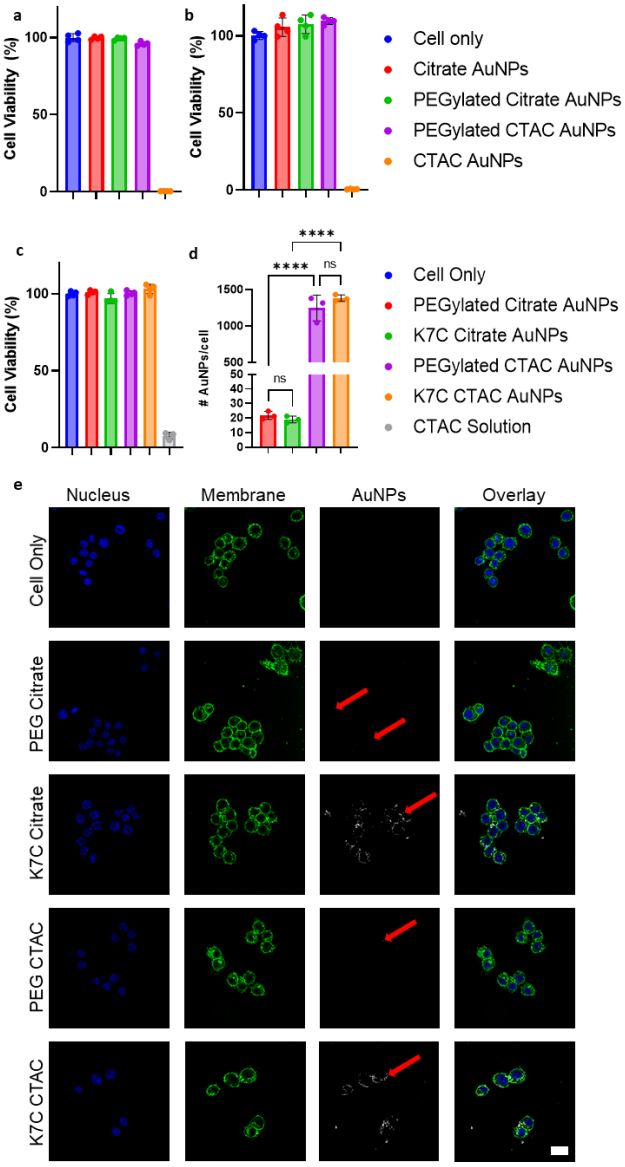

Figure 3.5: Cell viability and cell uptake experiments with modified CTAC-capped AuNPs compared to modified citrate-capped controls. a) XTT cell viability data were collected from DC2.4 cells treated with PEGylated and non-PEGylated AuNPs and incubated overnight. **b)** XTT cell viability data were collected from RAW 264.7 cells treated with PEGylated and non-PEGylated AuNPs and incubated overnight. For 5a and 5b, colored bars indicate mean cell viability values for N=4 measures for each treatment group. **c)** XTT cell viability data were collected from RAW 264.7 cells following 3 hours of incubation with AuNPs modified with PEG or with malPEG-K7C conjugates. A CTAC solution was used as a positive control. Colored bars indicate mean cell viability values for N=3 measures for each treatment group **d)** ICP-MS estimations of the number of AuNPs/cell for RAW 264.7 cells following the same treatments used in 5d. Colored bars represent mean AuNP/cell values for N=3 measurements per treatment group. One-way ANOVA was used to assess the statistical significance between PEG-only AuNPs and K7C AuNPs. ns = no statistical significance, **** = p<0.0001. **e)** CLSM images of RAW 264.7 cells treated with AuNPs following the same conditions as in 5d. Red arrows point to the scattering signal associated with internalized AuNPs. The scale bar is 20 µm.

While the conjugation of PEG to the surface demonstrated improved biocompatibility, the conjugation of additional ligands is essential to improving and understanding interactions between nanoparticles and cells. This bio-functionalization is key to optimizing nanoparticle-cell mechanisms that will enhance bioanalytical and nanomedicine outcomes. As we had previously shown that thiolated biomolecules could bind to malPEG on the surface of AuNPs, we conjugated malPEG to 60-nm AuNP surfaces and then incubated the mixture overnight with the model peptide K7C. In an earlier study, we demonstrated that K7C peptides increase AuNP uptake by cells.[21,128] We decided to focus our cell uptake and cell viability studies on using 60-nm diameter AuNPs based on nanoparticles of this diameter being favored for cellular uptake, as demonstrated in earlier studies.[143] We first confirmed that a 3 h incubation of RAW 264.7 cells with these K7C-conjugated AuNPs would not affect cell viability (Figure 5c). Having seen that viability was not affected, we assessed AuNP uptake. We used K7C-AuNPs to treat RAW 264.7 cells that we then imaged using confocal scanning laser microscopy (CLSM) (Figure 3.5e). We have previously shown that AuNP uptake by cells can be visualized by CLSM based on the scattering caused by AuNPs.[21,32,34] We observed that our CLSM images possess a clear scattering signal associated with AuNPs internalized by the cells, indicating that CTAC-capped AuNPs modified to have K7C surface chemistry demonstrate similar uptake compared to the more commonly applied citrate-capped AuNPs.[144,145]

We then quantified this uptake using ICP-MS methods. In preparing our samples, we noted that CLSM detected an AuNP signal that was not associated with cells. We attribute this signal to AuNPs that stuck to the surface of the coverslip due to the strong

positive charge on the AuNP surface from K7C. To remove this background signal for our ICPMS analysis, we washed cells with a dilute gold etchant (KI/I_2) solution. Further, we prepared separate wells without cells that received the same treatment and washing steps. We quantified the gold content of these wells with the gold content of the treated wells that contained cells. We used the measurements from the wells with no cells as the background signal that was subtracted from the signal measured from the wells with cells. Our ICP-MS results demonstrated that RAW 264.7 cells interacted with originally CTAC-capped AuNPs at identical rates ($p>0.05$) to originally citrate-capped cells for both mPEG-SH and K7C surface chemistries (Figure 3.5d). With this, we show that CTAC-capped AuNPs can be applied in bioanalytical and biomedical settings and resolve similar effects to citrate-capped AuNPs.

It is worth considering that the relative number of AuNPs inside cells is dependent on calculations that assume uniform AuNP diameter. ICP-MS measures the mass of Au in each sample, which is then translated into the number of AuNPs using calibration curves and assuming that each individual AuNP possesses the same shape and size (Figure C3.9). Thus, the calculations for 60-nm AuNPs tend to be more accurate for CTAC-capped AuNPs than for citrate-capped AuNPs, as demonstrated by the differences in the size distributions we measured in this study. When considering if exact quantification of the number of AuNPs/cell is needed, researchers may look into using CTAC-capped AuNPs for more accurate measures.

3.5 Conclusions

In this study, we demonstrated a significant difference between the size distribution (i.e. monodispersity) of AuNPs synthesized by two different methods – citrate-capped and CTAC-capped synthesis. The AuNPs synthesized by the CTAC-capped method demonstrated a significantly narrower size distribution than AuNPs synthesized by the citrate-capped method, indicating a higher degree of monodispersity. While CTAC-capped AuNPs are innately cytotoxic and thus incompatible with many bioanalytical and biomedically relevant systems, we provide a method by which CTAC can be physically replaced with biocompatible PEG molecules without changing the monodispersity of the AuNPs. The PEG molecules used in this process impart biofunctionalization to the AuNPs the PEG is conjugated to, as we showed using maleimide-PEG that conjugates to thiolated peptides or nucleic acids. Compared to the often-used citrate-capped AuNPs, we showed that CTAC-capped AuNPs demonstrate the same uptake behavior in cells when modified to possess the same surface chemistry. Our work additionally demonstrates the value of SP-ICP-MS in assessing monodispersity between AuNPs synthesized using various methods. Further, we demonstrated a possible method by which cytotoxic CTAC ligands may be removed from the surface of monodisperse CTAC-capped AuNPs, increasing their viability for bioanalytical and biomedical research. Continued studies into the utility of SP-ICP-MS for nanoparticle population comparisons are encouraged. We propose that researchers consider using appropriately modified CTAC-capped AuNPs for bioanalytical and biomedical studies, given their high degree of monodispersity. In particular, we encourage further investigations into alternative surface chemistry modification and ligand functionalization options for CTAC-capped AuNPs.

3.6 Acknowledgements and Funding

The authors acknowledge the assistance of Dr. Steven Foster, Dr. Preston Larson, Dr. Julian Sabisch, and Dr. Ben Fowler. Additionally, the authors acknowledge the University of Oklahoma (OU) Samuel Roberts Noble Microscopy Laboratory (SRNML), the OU Mass Spectrometry, Proteomics & Metabolomics (MSPM) Core, and the Oklahoma Medical Research Foundation (OMRF) Imaging Core Facility for assistance. The authors would like to thank Sarah Butterfield, Majood Haddad, Luke Whitehead, Nathan Mjema, Abigail Thomas, and Sam Ferguson for their help synthesizing nanoparticles.

This work was supported in part by awards from NIH COBRE (P20GM135009), NSF CAREER (2048130), and OCAST (HR20-106) and by the University of Oklahoma Vice President for Research and Partnerships SRNML Voucher Program.

Chapter 4 – Single Particle ICP-MS for Modeling Gold Nanoparticle Synthesis, Scaling, and Kinetics

4.1 Abstract

Given their relative ease of synthesis and characterization, gold nanoparticles have been used for decades as model and functional materials in nanomedicine. Seed-mediated growth of gold nanoparticles is a commonly applied synthesis method given the improved monodispersity compared to other methods. Currently, seed-mediated growth for specific sizes of gold nanoparticles is limited by a lack of standard models relating reaction components to final predicted diameter. In this study, we use transmission electron microscopy (TEM) and single particle inductively coupled plasma mass spectrometry (SP-ICP-MS) to identify the mathematical relationship between the moles of precursor ionic gold and the moles of nanoparticle seeds in a given gold nanoparticle seed-mediated growth reaction. We identified this relationship for two different gold nanoparticle seed-mediated growth reactions – citrate-based and cetyltrimethylammonium chloride (CTAC)-based. We tested our model by synthesizing gold nanoparticles of different target diameters and found the resulting mean diameters to be significantly similar to the target diameter. We also estimated the yield of each growth reaction for different target diameters and demonstrate how our mathematical models allow for easy reaction scale-up. Finally, we show how SP-ICP-MS can be used to measure the growth kinetics of CTAC-based AuNPs and how the rate of AuNP growth is dependent upon target final diameter. Combined, these results provide tools and methods by which gold nanoparticles of different core type and diameter may be readily synthesized based on well-defined mathematical relationships.

This chapter is being prepared as a manuscript for submission to *Nano Letters* – IF 12.262 – as:

Frickenstein A, Harcourt T, Malik Z, Means N, Taffe H, Longacre L, Wilhelm S, “Single Particle ICP-MS for Modeling Gold Nanoparticle Synthesis, Scaling, and Kinetics,” *Nano Letters,* Aug. 2023

Author contributions to this work:

Alex Frickenstein – Project leader, primary experiment coordinator and performer, primary writer

Tekena Harcourt – Assisted with making and characterizing nanoparticles as well as mathematical model testing

Zain Malik – Assisted with making and characterizing nanoparticles as well as mathematical model testing

Nathan Means – Assisted with making and characterizing nanoparticles

Haley Taffe – Assisted with making and characterizing nanoparticles

Logan Longacre – Assisted with making and characterizing nanoparticles

Stefan Wilhelm – Project adviser and corresponding author

4.2 Introduction

Presiding at the forefront of investigative and clinical nanomedicine, gold nanoparticles (AuNPs) have been used extensively to understand the interactions between nanoparticles and cells.[146-148] Studies with AuNPs have helped reveal that, among other factors, nanoparticle size is a critical component of determining cellular uptake of nanoparticles. It is well-established that AuNPs can be synthesized using multiple different methods.[149] One commonly-used approach for making relatively monodisperse and innately biocompatible AuNPs was developed by Perrault and Chan whereby AuNPs are synthesized using a seed-mediated growth reaction facilitated by hydroquinone (HQ) reduction of Au^{3+} in the presence of small (~14 nm) AuNP seeds.[118] In addition to showing that HQ reduction provided more monodisperse size and shape across synthesized AuNPs compared to using citrate reduction alone, Perrault and Chan indicated the final AuNP size after the growth reaction is dependent upon the number of AuNP seeds used.[118]

Of note, the findings of Perrault and Chan focused on citrate-based synthesized AuNPs, which are immediately ready for use in nanomedicine given their innate biocompatibility and relative ease of surface modification.[102,150] We have previously shown that AuNPs synthesized by an alternative method, one using cetyltrimethylammonium chloride (CTAC), are more monodisperse in colloidal suspension compared to citrate-synthesized AuNPs. Additionally, we demonstrated how CTAC-capped AuNPs can be made biocompatible and biofunctional using physical replacement techniques for PEGylation.[31] Currently, no model exists to relate the reaction components used for CTAC-capped synthesis and the final predicted diameter,

complicating future synthesis and indicating of lack of clear definition between reaction inputs and final diameter output. There is a need for such models to be designed in order to a) provide clear guidelines for homogenizing AuNP synthesis approaches and b) provide models that improve confidence in final synthesis outcomes.

In order to characterize AuNPs and determine mean final diameter at a single nanoparticle level, transmission electron microscopy (TEM) and single particle inductively coupled plasma mass spectrometry (SP-ICP-MS) emerge as primary analysis methods. Batch analysis methods of AuNPs are insufficient for acquiring accurate measurements of exact AuNP diameter and monodispersity measurements. Further, while TEM is a valuable method for visualizing nanoparticles, it is a low-throughput technique that requires careful sample preparation to collect images. We have previously reported on the benefits of SP-ICP-MS for assessing nanoparticles in terms of colloidal stability, reaction kinetics, and size distributions.[21,31,116,117] Thus, when considering a method for rapidly quantifying synthesized AuNP diameter, SP-ICP-MS is an ideal choice.

In this study, we identify and quantify the relationship between the number of AuNP seeds used during growth reactions and the final AuNP diameter. We quantify the relationship for two different AuNP growth reactions – citrate-based and CTAC-based – in terms of the final AuNP diameter and the ratio of moles of AuNP seeds to moles of precursor ionic gold (Au^{3+}). We then test our models by synthesized three different sizes of each AuNP and quantifying the results by SP-ICP-MS. We further measure the approximate reaction yield by SP-ICP-MS. By defining the relationship between final diameter and the discussed ratio of moles, we provide opportunity for ease of scaling up reactions per core engineering principles. Finally, we use SP-ICP-MS to measure the

growth kinetics of CTAC-based AuNPs. Together, our methods and findings pave the way for ease-of-access of AuNP synthesis by citrate- and CTAC-based methods while also outlining approaches by which others may similarly design mathematical models for nanoparticle synthesis outcomes.

4.3 Experimental Section

4.3.1 Synthesis of Citrate-based AuNPs

Prior to any synthesis, we cleaned glassware using ~100 mL of aqua regia comprised of a 3:1 v/v mixture of hydrochloric acid (HCl, SigmaAldrich ACS reagent 37%) and nitric acid (HNO_3, SigmaAldrich ACS reagent 70%). We rinsed aqua regia-treated glassware thoroughly with nanopure water before synthesis. To synthesize citrate-based AuNPs using the established HQ reduction method, we first made ~14 nm AuNP seeds based on the well-established Trukevich method.[118,122] We added 1 mL of 30-mg/mL (0.102 M) aqueous sodium citrate tribasic dihydrate (SigmaAldrich) to ~100 mL of nanopure water inside the cleaned glassware. We mixed the solution gently using a Teflon magnetic stir bar and brought the solution to a boil. We then added100 µL of a 98.5 mg/mL (0.25M) solution of $HAuCl_4$ (SigmaAldrich) and stirred the solution vigorously for 7 min. After 7 min., we cooled the solution to room temperature, quenching the reaction, by placing the glassware on an ice bath. Once cooled to room temperature, we characterized the resulting AuNPs by dynamic light scattering (DLS) and ultraviolet spectrophotometry (UV-Vis) and stored at 4°C prior to use. We took a 1 mL aliquot of these AuNP seeds and added 11 µL of a 10% Tween20 (SigmaAldrich) solution such that the final Tween20 percentage was 0.01%. We centrifuged this aliquot at 15,000 relative centrifugal force (rcf, 1x rcf = 1x g-forge) for 30 min. at 4°C and removed the supernatant. The resulting pellet was dropped onto a copper TEM grid with coper film (Ted Pella) for TEM imaging to determine exact AuNP seed diameter.

We then synthesized >14 nm AuNPs of different target sizes. Across all syntheses performed, we kept the mole amounts of $HAuCl_4$, sodium citrate tribasic dihydrate, and

hydroquinone (HQ, SigmaAldrich) the same and only varied the moles of ~14 nm AuNP seeds added. In this way, we define the predicted final AuNP diameter resulting from the citrate-based growth reaction in terms of the ratio of the moles of ~14 nm AuNP seeds added and of the moles of ionic gold (Au^{3+}) added, henceforth referred to as the AuNP/Au ratio. We chose this ratio as our independent variable as it allows for easy reaction scaling based on the target number of AuNPs needed from a given reaction.

We rationally selected AuNP/Au ratio values based on prior literature.[31,118,128] We targeted final predicted diameters of less than or equal to 100 nm based on relevance of nanoparticle size in biomedical applications and nanoparticle *in vivo* behavior.[5,97,151] Selected ratio values are reported in Table 4.1. We used established methods as a guide for our syntheses.[118] Prior to synthesis, we measured the approximate concentration of the previously synthesized ~14 nm AuNP seeds using UV-Vis. Once we knew the concentration of the ~14 nm AuNP seeds, we calculated the milliliter volume of the ~14 nm AuNP seeds to add to the reaction vessel that would contain 1 mL of 0.025 M $HAuCl_4$ based on the target ratio value. Then, to a flask cleaned with aqua regia as previously described, we added (in order) chilled nanopure water, 1 mL of 0.025 M $HAuCl_4$, 1 mL of 0.015 M sodium citrate tribasic dihydrate, the calculated mL volume of ~14 nm AuNP seeds, and 1 mL of 0.025 M HQ under stirring such that the final solution volume in the flask was 100 mL. We let this reaction run overnight prior to characterization by DLS and UV-Vis. To remove excess reactants and smaller AuNPs resulting from new nucleation [118], we added 1mL of 10% Tween20 to the flask after the reaction was completed. After 10 min., we centrifuged for 90 min. at 4°C. We removed the resulting supernatant and suspended the pellet in ~10 mL of a 0.1% Tween20 0.01% sodium citrate tribasic

dihydrate solution. We split the solution into 1.5 mL tubes and centrifuged again for 30 min. at 4°C. We removed the supernatant and combined the pellets, diluting to a final volume of ~1 mL. We adjusted the centrifugation speed based on estimated AuNP diameter (see Table 4.1). The purified AuNPs were characterized by DLS, UV-Vis, TEM, and SP-ICP-MS.

4.3.2 Synthesis of CTAC-based AuNPs

Prior to any synthesis, any glassware was cleaned using aqua regia as described in Section 4.3.1. The synthesis of CTAC-based AuNPs occurs in multiple steps according to established protocols.[31,119,124] First, we synthesized precursor Au-clusters that would be used to make the ~10 nm CTAC AuNP seeds for later reactions. To make Au-clusters, we added 9.5 mL of a 38 M cetyltrimethylammonium bromide (CTAB) solution and 500 µL of a 5 mM $HAuCl_4$ solution to a 20-mL cleaned scintillation vial. We heated the vial with the solution to 30°C and stirred using a Teflon-coated magnetic stir bar for 5 min. We then added 600 µL of a freshly prepared ice-cold 0.1 M $NaBH_4$ solution to the vial under vigorous stirring. After mixing for 2 min., we let the reaction rest at 30°C for 3 hours before measuring the Au-cluster extinction spectrum using UV-Vis. Per prior methods, we used the extinction value at a wavelength of 390 nm to estimate the volume of Au-clusters to add for the next step.[31]

Compared to established protocols, we scaled-up our synthesis of ~10 nm CTAC AuNP seeds by 25x to ensure we had enough for subsequent experiments. To a clean 250-mL flask, we added 75 mL of a 110 M CTAC solution, 10.575 mL of a 0.17 M L-ascorbic acid (SigmaAldrich) solution, and 2246 µL of the previously synthesized Au-clusters. We determined the Au-cluster volume to add based on the extinction value (0.44) at the extinction wavelength of λ = 390 nm per prior methods.[31] We mixed the resulting solution for 5 min at 25°C before rapidly adding 25 mL of a 1 mM solution of $HAuCl_4$. We allowed the solution to continue mixing for 15 min. before centrifuging for 90 min. at 21,000 rcf and 4°C. We removed the supernatant after centrifugation and resuspended the AuNP pellet in nanopure water. We repeated centrifugation one more

time, this time resuspending the AuNP pellet in a 20 mM solution. The final solution was diluted to a AuNP concentration of ~5.9 nM as measured by UV-Vis. We characterized the final ~10 nm CTAC AuNP seeds by DLS, UV-Vis, and TEM to estimate colloidal stability and actual diameter. SP-ICP-MS could not be used to characterize CTAC AuNP seeds based on the limits of detection of the method.[30,138]

Using the ~10 nm CTAC AuNP seeds we synthesized, we proceed to investigate the relationship between the AuNP/Au ratio and the final diameter following CTAC-based growth reaction (see Table 4.2). We rationally selected AuNP/Au ratio values based on prior literature, targeting a similar range of diameters as discussed in Section 4.3.1.[31,119,124] To perform CTAC-based synthesis, we placed a cleaned 250-mL flask onto a hot plate set for 35°C. Separately, we prepared three solutions. Our first solution (Solution A) was a 20 mM CTAC solution that contained the ~10 nm CTAC AuNP seeds. The volume of seeds used for each synthesis was determined based on the target AuNP/Au compared to the measured concentration of the stock CTAC AuNP seed solution. We set the final volume of Solution A to be 20 mL. We sonicated Solution A for 10 min. before adding it to the 250-mL flask to pre-heat. Our next solution (Solution B) was a 22 mL 0.625 mM $HAuCl_4$ solution. We loaded Solution B into a 30 mL plastic syringe, which was mounted on a Harvard Apparatus PHD ULTRA syringe pump (Harvard Apparatus). The final solution (Solution C) was a 10 mM solution of L-ascorbic acid, which serves as the reducing agent for CTAC-based growth reactions. We added 1.3 mL of Solution C to the flask containing Solution A and gently mixed for 1 min. using a Teflon-coated magnetic stir bar. After 1 min., we started the Harvard syringe pump to begin dropwise addition of Solution B. We set the syringe pump to add solution at a rate

of 20 mL/hr for 1 hour. After 1 hour, we allowed the reaction to continue for 15 min. before the AuNP solution was immediately centrifuged. As with the citrate-based synthesis, we varied the centrifugation speeds based on estimated AuNP diameter (see Table 4.2). For the first round of centrifugation, we centrifuged for 90 min. at 4°C. We then removed the supernatant, resuspended the AuNP pellet in ~10 mL of nanopure water, split the solution into 1.5 mL tubes, and centrifuged one more time for 30 min. at 4°C. After this centrifugation, we combined AuNP pellets and resuspended to ~1 mL using a 20 mM CTAC solution. We characterized the purified AuNPs by DLs, UV-Vis, TEM, and SP-ICP-MS.

4.3.3 Characterization of AuNPs and Model Development

Immediately after synthesis and centrifugation, we characterized AuNPs by dynamic light scattering (DLS) and ultraviolet-visible spectrophotometry (UV-Vis) to estimate AuNPs hydrodynamic diameter (HDD), peak absorption wavelength, and concentration in solution. We collected 20 - 100 µL aliquots of purified and concentrated AuNPs, centrifuged them at a speed appropriate for their estimated diameter, and dropped 5 µL of the resulting pellet onto a copper TEM grid with carbon film. We collected TEM images using a JEOL-Zeiss 2010F. We analyzed all collected images using ImageJ to estimate the mean diameter of each synthesized AuNP population.

SP-ICP-MS allows for high-throughput analysis of individual nanoparticles in solution with single nanoparticle resolution. We have previously used SP-ICP-MS to characterize AuNP diameter as well as to identify differences in AuNPs based on colloidal stability or synthesis method.[31,117] We used these same methods to identify the mean diameter estimate and relative monodispersity of all synthesized CTAC-based AuNPs. All SP-ICP-MS measurements of AuNPs were performed using a PerkinElmer NexION 2000 using the methods and conditions described in Section 3.3.3 and Appendix B.

We compared mean diameter estimates collected from TEM imaging and from SP-ICP-MS data against each other and against the target AuNP/Au ratio values used during AuNP synthesis for both citrate- and CTAC-based syntheses. We plotted the data and used GraphPad PRISM to identify non-linear regression results linking the independent variable (AuNP/Au ratio) to the dependent variable (final AuNP diameter). We performed additional analysis using collected data to identify possible correlations between estimated mean diameter and measured hydrodynamic diameter as determined from

DLS measurements. Additionally, we compared mean diameter estimates from TEM and SP-ICP-MS to identify any significant differences between the results from the two single particle analysis methods.

4.3.4 AuNP Predictive Growth Model Testing

After generating the predictive growth models for both citrate-based and CTAC-based AuNP synthesis, we sought to test the apparent accuracy of our models. Using the AuNP growth reaction procedures outlined in Section 4.3.1 and Section 4.3.2, we synthesized citrate-based and CTAC-based AuNPs with targeted diameters of 30 nm, 60 nm, and 90 nm. We used our predictive growth models to determine the volume of either ~14 nm citrate AuNP seeds or ~10 nm CTAC AuNP seeds to use in our respective synthesis approaches. Following synthesis, we purified the AuNPs using centrifugation, as previously described. We quantified the diameter distribution of the resulting synthesized AuNPs using SP-ICP-MS to compare how the final estimated mean diameter compared with the diameter predicted from our models.

4.3.5 AuNP Growth Reaction Scale-up

As previously described, the final diameter of AuNP growth synthesis reactions can be predicted based on the AuNP/Au molar ratio. By defining this relationship in terms of molar ratios, we present an opportunity to easily scale-up AuNP growth synthesis reactions to increase total number of synthesized particles. This approach may prove especially valuable for studies that require large numbers of AuNPs, such as animal studies. To validate that our predictive models remain accurate for scale-up reactions, we synthesized 60 nm target diameter AuNPs using both citrate- and CTAC-based growth reactions. We scaled-up reactions five times (5x) by volume compared to the normal reaction scale as described in Section 4.3.1 and Section 4.3.2. Following purification, we quantified AuNP diameter using SP-ICP-MS and compared the mean estimated diameter to the target of 60 nm.

4.3.6 SP-ICP-MS Measurement of CTAC-based AuNP Growth Reaction Kinetics

As described in Section 4.3.2, our CTAC-based AuNP growth reaction occurs over a time span of ~75 min. During this time, the color of the solution changes, indicated a change in the size of suspended AuNPs. To characterize the growth of AuNPs during the reaction, we synthesized CTAC-based AuNPs of target diameters 30 nm, 60 nm, and 90 nm as described in Section 4.3.2. We used our predictive model generated as described in Section 4.3.3 to determine the volume of ~10 nm CTAC seed solution to use for each synthesis. During the reaction, we collected 100 µL of the reaction solution at t = 1 min., 5 min., and every 5 min. after until t = 75 min. We used UV-Vis spectrophotometry with quartz cuvettes to measure the change in reaction solution extinction spectrum with time. Additionally, for the 60 nm AuNP synthesis, we used SP-ICP-MS to track the changes in mean mass with time and identify AuNP growth kinetics. For SP-ICP-MS measurements, we applied thresholds per prior protocols to remove signal from small AuNPs (i.e., new or original seed nuclei) to better measure the change in AuNP mass with time.[21]

4.4 Results and Discussion

4.4.1 Citrate- and CTAC-based AuNP Predictive Growth Models

We performed seed-mediated AuNP growth using both citrate-based and CTAC-based methods based on prior protocols. We acquired the mean estimated diameter of synthesized ~14 nm AuNP citrate seeds (Figure C4.1) and ~10 CTAC AuNP seeds (Figure C4.2) using TEM. We selected TEM based on its high resolution and due to concerns about the limit of detection of SP-ICP-MS for smaller AuNPs.[138]

Accurate determination of the diameter of seeds used during seed-mediated synthesis is vital to accurate prediction of final nanoparticle size. We used UV-Vis to estimate the concentration of our AuNP seeds based on Beer-Lambert's Law.[31,118,135,136] Prior studies have shown that the molar extinction coefficient used to estimate nanoparticle concentration is heavily dependent upon the diameter of the nanoparticle. As such, small differences in nanoparticle diameter can result in large changes in estimated concentration. When considering that our predictive models are reliant upon the AuNP/Au ratio, where the mole amount of AuNP seeds added is a vital component of the ratio value, accurate seed concentration is necessary to ensure model accuracy. Given this, we advise that synthesized AuNP seeds be full characterized by TEM for an accurate diameter measurement prior to any seed-mediated synthesis. Additionally, we recommend measuring the concentration of AuNP seed solution prior to each seed-mediated synthesis performed as the concentration of AuNP seeds in solution can change with time or repeated use of seed stock solutions.

We synthesized AuNPs using both citrate- and CTAC-based growth synthesis methods while varying the AuNP/Au ratios through using different volumes of ~14 nm

citrate AuNP seeds (Figure C4.1) or ~10 nm CTAC AuNP seeds (Figure C4.2) of known concentration, respectively. By measuring the HDD using DLS (Figure C4.3) as well as the estimated mean diameter using TEM (Figure C4.4, C4.5) and SP-ICP-MS (Figure C4.6 – C4.9, Table D4.1), we were able to correlate the final estimated AuNP diameter of each reaction with the AuNP/Au ratio used during synthesis. We began by considering the data from the citrate-based synthesis as this reaction is currently more widely used and we could use similar data from prior reports as a guide and for comparison points.[118] We report our results for citrate-based AuNPs in Figure 4.1 and Table 4.1.

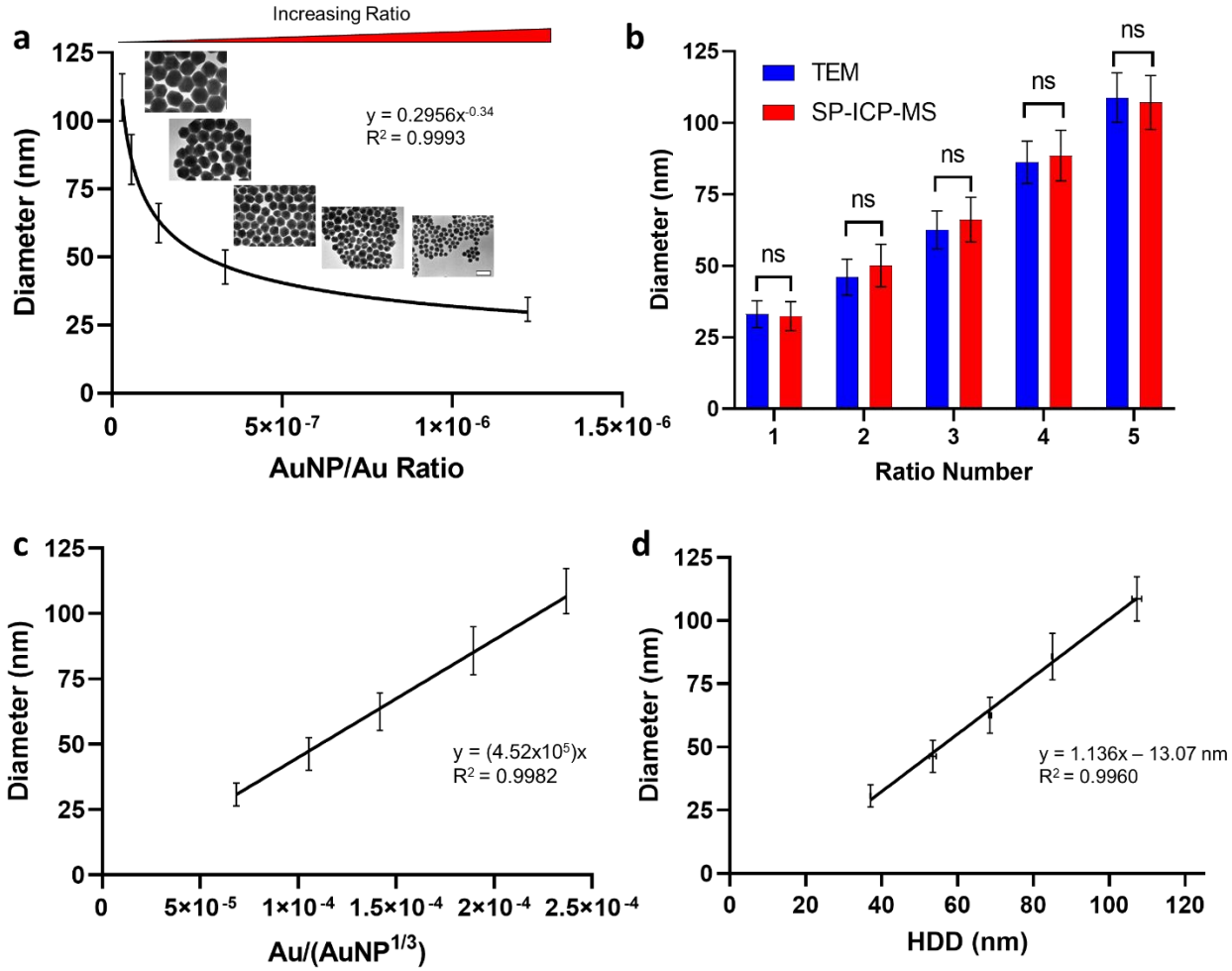

Figure 4.1: Predictive modeling of citrate-based AuNPs. a) The plot of measured AuNP diameter as determined by TEM and SP-ICP-MS against the ratio of moles of 14 nm AuNP seeds used to the moles of Au^{3+} ions used reveals a strong power function correlation between the two variables. Mean diameter values were plotted with error bars representing standard deviation. Inset TEM images show AuNPs from all five different ratio numbers and demonstrate an increase in AuNP diameter with decreasing ratio value. Scale bar is 100 nm. **b)** Mean AuNP diameter as measured by TEM is not statistically significantly different from the mean diameter measured by SP-ICP-MS. Values plotted are mean diameter estimates with error bars representing the standard deviation. Kolmogorov Smirnov statistical analysis was performed on diameter distributions from TEM and SP-ICP-MS for each ratio. ns = no statistical significance **c)** Linear form of the relationship between moles of AuNP seeds and moles of Au^{3+} ions used during the citrate-based growth reaction. **d)** The plot of measured AuNP diameter as determined by TEM and SP-ICP-MS against hydrodynamic diameter (HDD) as measured by DLS reveals a strong linear correlation between the measurements. Mean values for hydrodynamic diameter and actual diameter are shown with error bars representing standard deviation.

Table 4.1: DLS, TEM, and SP-ICP-MS Measurements of Citrate-based AuNPs

Ratio Number	AuNP/Au Ratio Value (mols AuNP/mols Au3+)	Centrifugation Speed (rcf)	HDD (nm)[#]	TEM Diameter (nm)[#]	SP-ICP-MS Diameter (nm)[#]
1	1.22E-06	3500	37.1 ± 0.1	30.7 ± 4.5	33.1 ± 4.7
2	3.33E-07	2000	53.5 ± 0.9	46.3 ± 6.3	50.1 ± 7.4
3	1.37E-07	1200	68.6 ± 0.4	62.5 ± 7.2	66.2 ± 7.8
4	5.75E-08	900	85.0 ± 0.2	85.8 ± 9.2	88.5 ± 8.9
5	2.94E-08	800	107.3 ± 1.3	108.6 ± 8.7	107.1 ± 9.5

[#] Mean value ± standard deviation.

From our results for citrate-based synthesis, we see a strong correlation between the AuNP/Au ratio and the final AuNP diameter as measured by TEM and SP-ICP-MS (Figure 4.1a). SP-ICP-MS measurements are reported as the frequency of AuNPs of specific masses. We converted these measurements into diameter frequency values and a correlating AuNP size distribution using Equation 3.3 (see section 3.4.1). Our results align with data from Perrault and Chan, which showed a similar trend between the final AuNP diameter and the number of AuNP seeds used in the reaction.[118] Additionally, we show that the AuNP diameter can be measured using either TEM or SP-ICP-MS with similar results (Figure 4.1b). TEM is advantageous for collecting images of synthesized AuNPs, while SP-ICP-MS allows for high-throughput measurement of AuNPs with relatively less sample preparation and data processing. By taking the inverse cubic root of the number of moles of AuNPs used in the reaction, we identify a possible linear correlation between reaction input and final estimated diameter (Figure 4.1c). We performed this operation based on the cubic relation between the mass of AuNPs and the diameter of AuNPs, as well as similar reporting methods from other literature.[21,31,117] We also quantified the relation between measured HDD by DLS and AuNP diameter (Figure 4.1d). It is expected that HDD is larger than actual core AuNP diameter based on sphere of hydration effects.[134,152] This phenomenon is observed in our collected data. Our results provide a guide by which the AuNP core diameter may be estimated from the DLS data without needing to use complex instrumentation as with TEM or SP-ICP-MS. That being said, we acknowledge that HDD measurements can change based on environmental or instrument settings.[153] We advise considering these factors when applying our results to future collected DLS data. Experimentation across environmental

and instrument conditions is recommended to characterize differences in reported HDD from synthesized AuNPs but is outside the scope of this study.

We applied the same analysis and modeling techniques to our CTAC-based AuNP synthesis results. We report our findings in Figure 4.2 and Table 4.2.

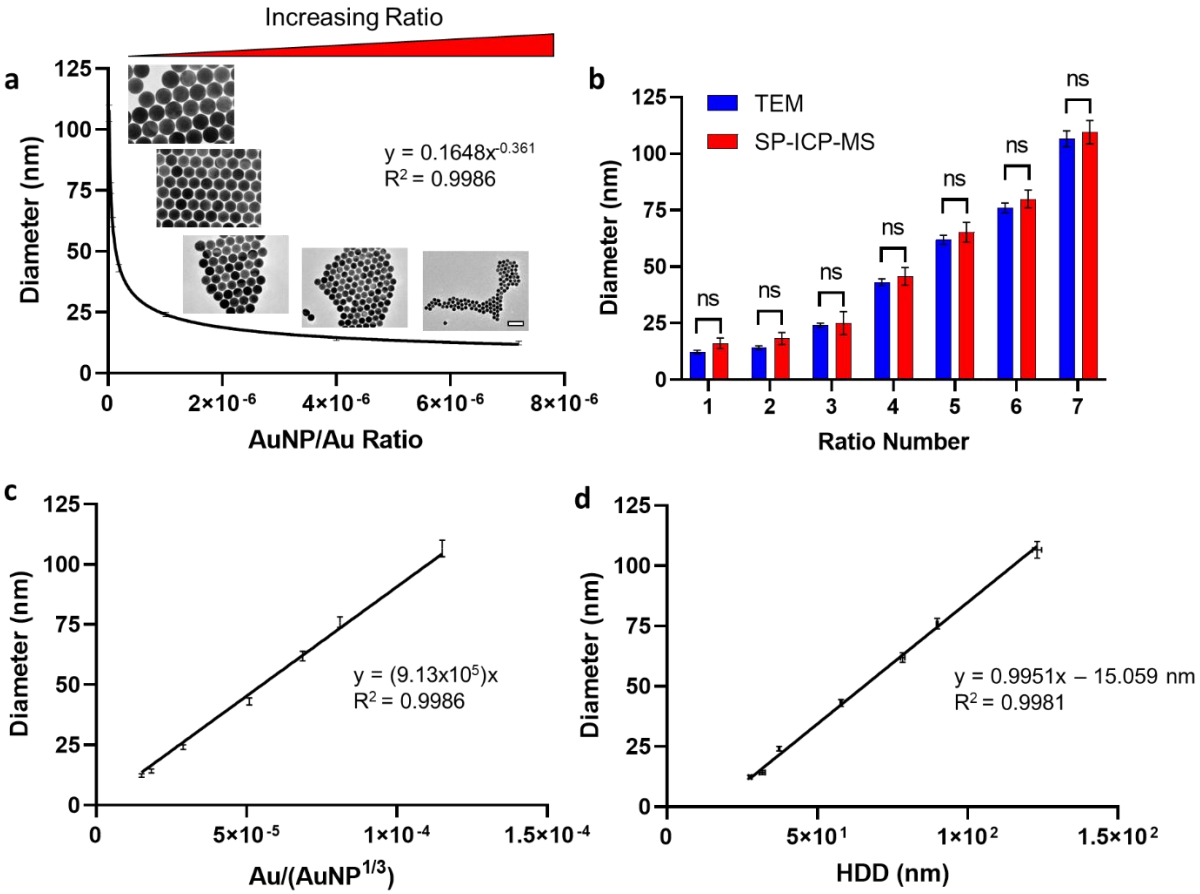

Figure 4.2: Predictive modeling of CTAC-based AuNPs. a) The plot of measured AuNP diameter as determined by TEM and SP-ICP-MS against the ratio of moles of ~10 nm CTAC AuNP seeds used to the moles of Au^{3+} ions used reveals a strong power function correlation between the two variables. Mean diameter values were plotted with error bars representing standard deviation. Inset TEM images show AuNPs from ratio numbers 3, 4, 5, 6, and 7 and demonstrate an increase in AuNP diameter with decreasing ratio value. Scale bar is 100 nm. **b)** Mean AuNP diameter as measured by TEM is not statistically significantly different from the mean diameter measured by SP-ICP-MS. Values plotted are mean diameter estimates with error bars representing the standard deviation. Kolmogorov Smirnov statistical analysis was performed on diameter distributions from TEM and SP-ICP-MS for each ratio. ns = no statistical significance **c)** Linear form of the relationship between moles of AuNP seeds and moles of Au^{3+} ions used during the CTAC-based growth reaction. **d)** The plot of measured AuNP diameter as determined by TEM and SP-ICP-MS against hydrodynamic diameter (HDD) as measured by DLS reveals a strong linear correlation between the measurements. Mean values for hydrodynamic diameter and actual diameter are shown with error bars representing standard deviation.

Table 4.2: DLS, TEM, and SP-ICP-MS Measurements of CTAC-based AuNPs

Ratio Number	AuNP/Au Ratio Value (mols AuNP/mols Au3+)	Centrifugation Speed (rcf)	HDD (nm)[#]	TEM Diameter (nm)[#]	SP-ICP-MS Diameter (nm)[#]
1	7.20E-06	15000	27.6 ± 0.5	12.3 ± 0.8	16.1 ± 2.3
2	4.00E-06	12000	31.7 ± 1.0	14.2 ± 0.9	18.3 ± 2.7
3	1.01E-06	3500	37.3 ± 0.2	24.1 ± 0.9	25.1 ± 5.1
4	1.85E-07	2000	57.9 ± 0.3	43.1 ± 1.5	45.7 ± 3.9
5	7.56E-08	1200	78.4 ± 0.7	61.9 ± 2.0	65.2 ± 4.4
6	4.60E-08	900	89.9 ± 0.3	76.0 ± 2.2	80.0 ± 3.9
7	1.60E-08	600	123.1 ± 1.5	106.6 ± 3.5	109.5 ± 5.1

[#] Mean value ± standard deviation.

As seen from our results, the relationship between the AuNP/Au ratio and the final mean diameter is well-correlated for CTAC-based AuNPs (Figure 4.2a). The trend is similar to that observed with citrate-based AuNPs, implying a similar relationship between the molar ratio and the final diameter despite synthesis methods being different. Given that both AuNP types grow by the reduction of Au^{3+} (aq) to Au^{0} (s) onto the surface of the AuNP seeds or via new nucleation, it is not too surprising to find similar trends in our predictive models. As with citrate-based AuNPs, we compared the diameter results from TEM and SP-ICP-MS and found no statistically significant difference between them, indicating that either method will give similarly accurate measures of AuNP diameter (Figure 4.2b). We should note that for smaller AuNP diameters, SP-ICP-MS will lose some accuracy as a result of instrument limits of detection.[138] As such, we advise using TEM for smaller AuNPs (<= 15 nm) given the improved effective "resolution" compared to SP-ICP-MS. For all other sizes, SP-ICP-MS is recommended given its high-throughput analysis approaches. As with our citrate-based analysis, we determined a linear correlation between a modified AuNP/Au ratio and mean diameter by taking the inverse cubic root of the mole number of ~10 nm CTAC AuNP seeds (Figure 4.2c). Finally, we plotted the measured HDD from DLS with the measured mean diameter (Figure 4.2d). We should note that in the case of CTAC-based AuNPs, the HDD estimate accounts for the CTAC bilayer that is present on the surface of the AuNPs.[31] Thus, the HDD is even further from the actual core diameter estimate compare to with citrate-based AuNPs given the relative size difference between CTAC and citrate molecules. We should also note that for smaller CTAC-based AuNPs, the linear model shown in Figure 4.2d becomes less accurate. We attribute this phenomenon to the reduced scattering seen from smaller

nanoparticles. The CTAC bilayer present on the surface of the AuNPs contributes to the HDD estimate. The smaller the core diameter of the AuNP, the more weight the CTAC will carry in the light scattering that occurs during DLS measurements, “masking” the scattering caused by AuNPs. This phenomenon has been shown to affect other smaller nanoparticles as well.[154] As such, for smaller AuNPs (<=15 nm) that are citrate- or CTAC-based AuNPs, we recommend using TEM imaging over other methods for accurate diameter measurements.

Having demonstrated the high degree of correlation in our models between AuNP/Au ratio and final AuNP diameter, we sought to test the accuracy of our models. We synthesized citrate- and CTAC-based AuNPs with target diameters of 30 nm, 60 nm, and 90 nm to demonstrate model accuracy across a wide range of target sizes. We characterized synthesized AuNPs using SP-ICP-MS exclusively (Figure 4.3, Figure C4.10). We chose to only perform SP-ICP-MS analysis of these AuNPs given the high-throughput nature of SP-ICP-MS and the lack of statistically significant different results between TEM and SP-ICP-MS, as demonstrated earlier in this section.

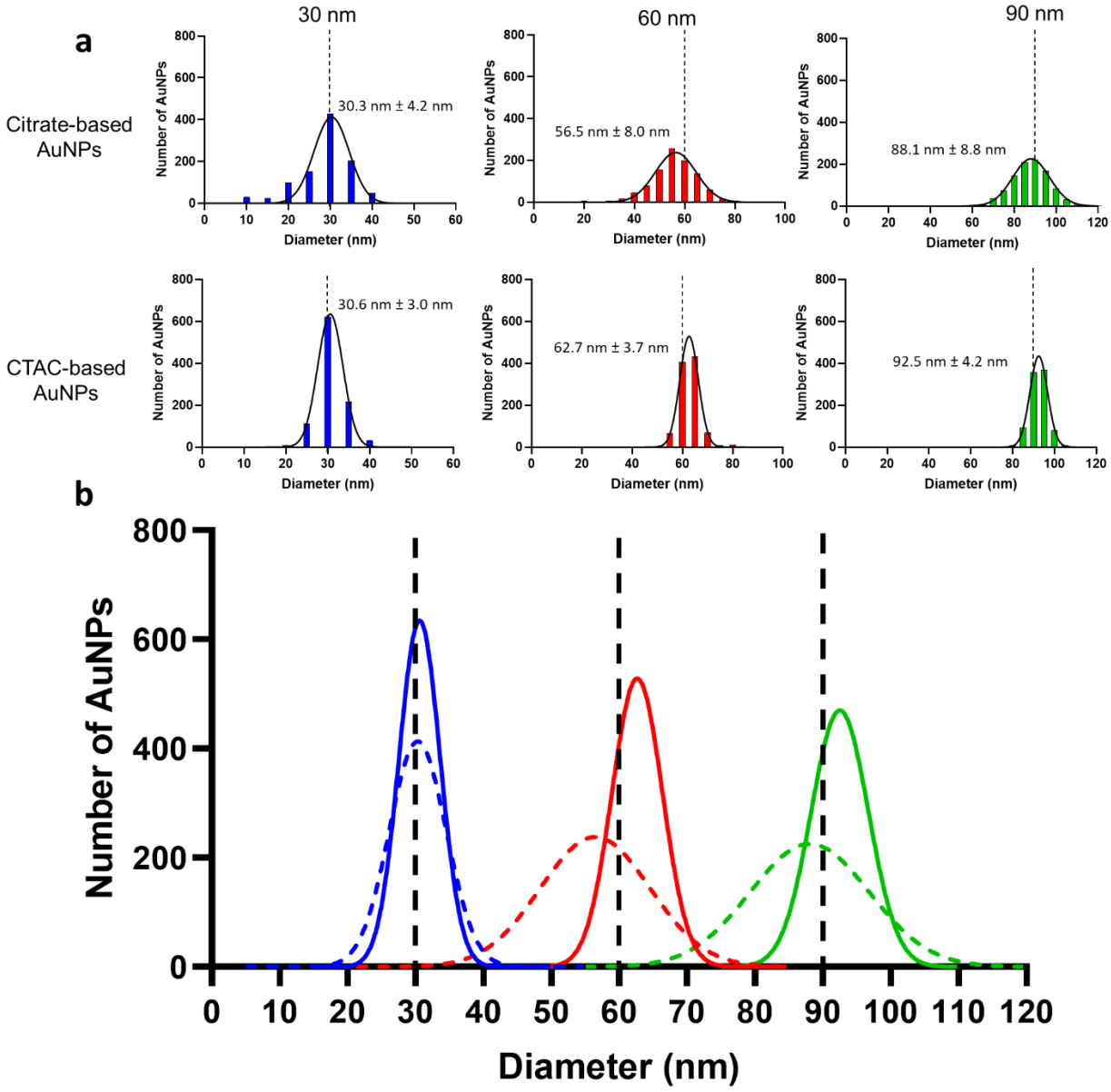

Figure 4.3: Testing of citrate- and CTAC-based AuNP predictive growth models using SP-ICP-MS. a) 30 nm, 60 nm, and 90 nm AuNPs synthesized using citrate-based and CTAC-based AuNP approaches were quantified by SP-ICP-MS to test model accuracy. Dotted black lines indicate target diameter. N > 1000 AuNPs for each population. Colored lines represent Gaussian normal fit of the distribution. Resulting mean diameter estimates are within 5% of the target diameter for all synthesized particles. **b)** Overlap of Gaussian normal fits of each synthesized group show increased monodispersity of CTAC-based AuNPs compared to citrate-based AuNPs. Solid lines represent CTAC-based AuNPs, dashed lines indicate citrate-based AuNPs. For citrate-based AuNPs, areas of distribution overlap are observed.

Based on the mean diameter estimates from our SP-ICP-MS measurement results, we conclude that our models are accurate to within <= 5% of the target diameter. At this level of difference from the target diameter, we argue that there is minimal difference in nanoparticle size-based behavior. Thus, we are confident our models provide a valuable and accurate guideline for future AuNP synthesis of either citrate-based or CTAC-based AuNPs so long as the recommendations and advice discussed in this section are taken into consideration. Additionally, in Figure 4.3b, we show the increased monodispersity of CTAC-based AuNPs compared to citrate-based AuNPs. We also show in Figure 4.3b areas where citrate-based AuNP distributions overlap, whereas CTAC-based AuNP distributions remain disparate. This phenomenon can be controlled by selecting

4.4.2 AuNP Growth Reaction Yield and Scale-up

During analysis of our 30 nm, 60 nm, and 90 nm model testing populations, we measured the estimated yield of each AuNP reaction in terms of the number of AuNPs that were “on-target” relative to the predicted nanoparticle diameter from each synthesis. In this care, we define “on-target” nanoparticles as being <= 5% different from the target predicted diameter value. We also estimated the yield based on the “accurate target yield” which provides an estimate of the number of AuNPs that were actually of the targeted diameter. We report our results in Table 4.3.

Table 4.3: Estimated "On-Target" Yield of AuNP Reactions

Synthesis Method	Target Diameter (nm)	"On-Target" Yield (%)[#]	"Accurate" Target Yield (%)[*]
Citrate	30	28.6	28.6
	60	30.5	20.1
	90	40.3	22.3
CTAC	30	42.6	38.9
	60	57.5	40.9
	90	67.4	62.3

[#] "On-target" AuNPs defined as AuNPs that are within <= 5% of the target diameter

[*] "Accurate" AuNPs defined as AuNPs that match the target diameter

As seen in Table 4.3, there is a significant difference in the yield values between citrate-based and CTAC-based synthesis approaches. We also show the differences in monodispersity between the citrate-based and CTAC-based AuNPs in Table D4.2. This level of analysis is only possible with single-nanoparticle analysis as we can get an accurate distribution of the diameter of AuNPs in the solution. While TEM is a viable method for similar analysis, SP-ICP-MS is better suited given its high-throughput rapid quantification of nanoparticles. Thus, we recommend using SP-ICP-MS measurements of AuNP concentration in cases where exact particle number need to be known, though the limit of detection of SP-ICP-MS must be considered relative to the predicted size of the nanoparticles.

Importantly, our results in Table 4.3 reveal that CTAC-based AuNP reactions produce more AuNPs that are “on-target” or that are of the actual target diameter compared to citrate-based AuNPs. This analysis raises two points worth considering for future nanomedicine research. The first of these is determining what percentage of administered AuNP dose is responsible for inducing the effect observed. While population-based analysis makes conclusions assuming that 100% of administered AuNPs are of the target size, our analysis reveals that in the case of citrate-based AuNPs, <= 40% of administered AuNPs are “on-target” for the desired diameter. By comparison, 40% - 70% of CTAC-based AuNPs are “on-target” for the desired diameter, revealing a more accurate AuNP population relative to the 100% assumption mentioned earlier. Based on these differences in yield of “on-target” AuNPs, we conclude that using CTAC-based AuNPs are a better model for nanoparticle-size-based nanomedicine experiments that use AuNPs as model nanoparticles. Additionally, our data reveals that there is a need

to understand how the different sizes within the size distribution of a given AuNP dose contribute differentially to observed biodistribution and/or effect. If this differential effect can be understood, nanoparticles may be better engineered to either a) design or improve synthesis methods to better approach the assumed 100% “on-target” diameter or b) understand how the distribution of sizes may impact nanoparticle fate and subsequent therapeutic effect following dose administration. This opens up a new way of defining AuNP dose as well, which is a dosing approach that is based on the concentration of on-target AuNPs understanding that < 100% of administered dose is of the target size. We leave it to future studies to further investigate these opportunities.

Our models are designed using a molar ratio (AuNP/Au) as the independent variable. Per core engineering principles, this allows for easy translation of our models to scale-up of AuNP reactions.[155] Scale-up of AuNP reactions is especially necessary for large *in vitro* or *in vivo* analysis, so demonstrating that our models apply to scaled-up reactions is inherently valuable. To test the model accuracy for scale-up reactions, we performed 5x scale-up synthesis of targeted 60 nm AuNPs for both citrate-based and CTAC-based AuNPs. We scaled up the reactions by volume only, keeping the concentration of all reaction components the same as if for standard (i.e., 1x scale) synthesis as described in Section 4.3.1 and Section 4.3.2. We purified the synthesized AuNPs by centrifugation and measured the mean diameter using SP-ICP-MS (Figure 4.4, Figure C4.11, Table D4.2).

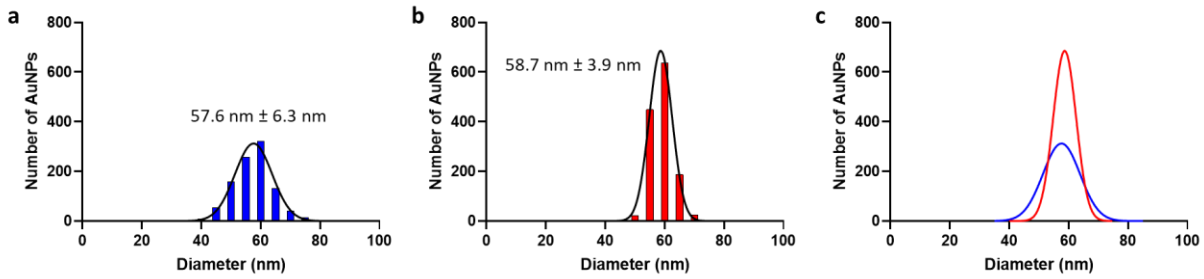

Figure 4.4: Predictive model accuracy of 5x scale-up synthesis as measured by SP-ICP-MS. a) SP-ICP-MS size distribution analysis of 5x 60 nm citrate-based AuNPs. **b)** SP-ICP-MS size distribution analysis of 5x 60 nm CTAC-based AuNPs. **c)** Overlay of 5x 60 nm citrate-based (blue) and CTAC-based (red) AuNPs Gaussian normal distribution from SP-ICP-MS measurements.

As with our 1x scale results, our 5x scale AuNPs are within <= 5% of the targeted diameter of 60 nm. From this, it is reasonable to conclude that our predictive models remain accurate for scaling factors applied to citrate- and CTAC-based synthesis. We note that scaling by volume, by concentration, or by both volume and concentration is possible. We advise that significant changes in reaction concentration could result in off-target AuNP product following synthesis due to either unfavorable reaction kinetics if the concentration in solution is too low or due to nanoparticle aggregation due to the concentration being too high. Given this, we advise scaling primarily by volume whenever possible.

4.4.3 CTAC-based AuNP Size-dependent Growth Reaction Kinetics

We have previously reported on the use of SP-ICP-MS to quantify reaction kinetics for gold-silver alloy nanoparticles.[116] Given the length of time over which CTAC-based AuNP synthesis occurs, we sought to measure the growth kinetics of CTAC-based AuNPs using SP-ICP-MS. We focused specifically on CTAC-based AuNPs as the kinetics of citrate-based AuNPs have been previously reported.[118] Additionally, the short timescale over which citrate-based AuNP synthesis occurs due to the rapid reduction action of hydroquinone is not well-suited for characterization by SP-ICP-MS measurements.[118] The kinetics of CTAC-based AuNP growth have been previously reported using UV-Vis and TEM methods, but SP-ICP-MS analysis has not yet been performed.[156] Further, identifying kinetic trends across different target AuNP diameters has not been explored, indicating an area where our predictive models can be used to inform size-based growth kinetics.

We collected aliquots from the reaction solution at varying timepoints throughout the CTAC-based growth reaction for 30 nm, 60 nm, and 90 nm target diameters of produced AuNPs. Aliquots were characterized by UV-Vis to measure the change in extinction spectra as the reaction progressed (Fig. 4.5a-4.5e). We chose this method of characterization given the color change observed during the reaction. We also measured the change in mean mass of 60 nm AuNPs in solution using SP-ICP-MS (Figure 4.5f). 60 nm AuNPs were chosen given the expected rate of growth compared to the frequency of small AuNP species in the early stages of growth that may be below the instrument limit of detection (in the case of not choosing 30 nm) and the likelihood of detecting a sufficient

number of AuNPs to acquire accurate mean mass estimations (in the case of not choosing 90 nm).

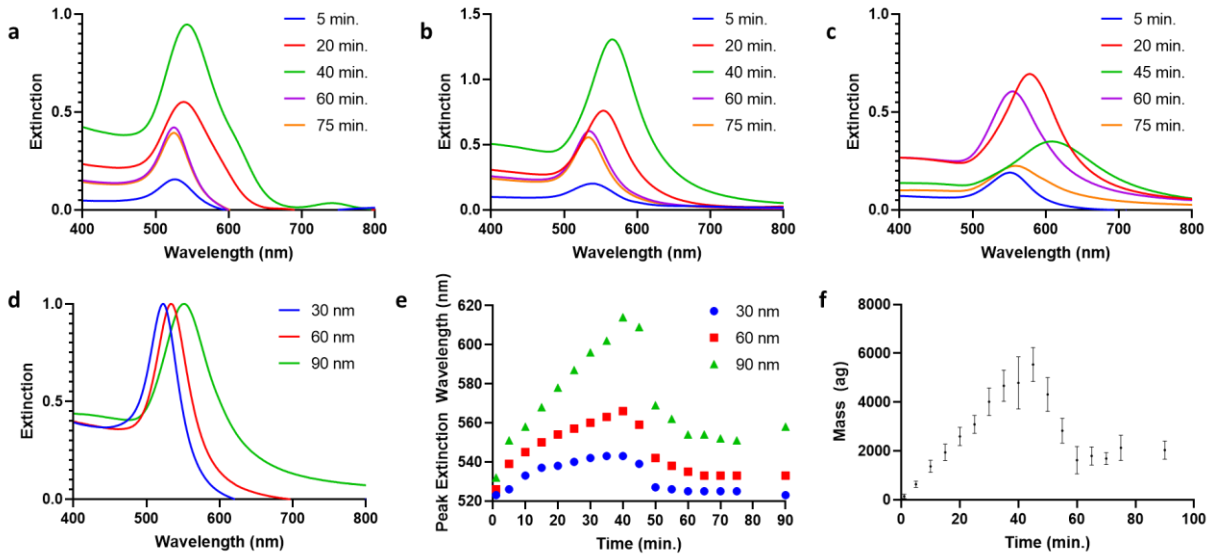

Figure 4.5: CTAC-based AuNP growth kinetics measurements. a-c) Change in UV-Vis extinction spectra with time for 30 nm, 60 nm, and 90 nm CTAC-based AuNPs during growth reaction. **d)** Final UV-Vis extinction spectra for synthesized AuNPs from kinetic analysis. **e)** The peak extinction wavelength changes with time for each synthesized CTAC-based AuNP. The 90 min. data is representative of the peak extinction wavelength after centrifugation. **f)** For 60 nm CTAC-based AuNPs, the mean mass (error bars = standard deviation) measured by SP-ICP-MS changes with time. The 90 min. data is representative of the mean mass after centrifugation.

As seen from our results, both UV-Vis and SP-ICP-MS can track changes in the AuNPs in solution based on changes in measured extinction spectra, peak extinction wavelength, or measured mean mass. Any data indexed at t = 90 min. represents measurements taken from the AuNPs after centrifugation. For all three UV-Vis spectra (Figure 4.5a-4.5c), we see the same general trend. The observed trend matches trends seen in a prior study for a single AuNP diameter, save for the timepoint at which the switch from growth to etching is earlier in the reaction..[156]

We observe that the peak extinction wavelength increases and the spectrum width increases until t ≈ 40 min. Then, we observe the peak extinction wavelength decrease and the spectrum narrow. The final peak extinction wavelength (t = 75 min.) matches the peak extinction wavelength value after centrifugation (Figure 4.5d). In terms of how the peak extinction wavelength changes with time, the trend is very similar across all three sizes (Figure 4.5e), the primary difference being the magnitude of the overall change in wavelength with time. The difference in magnitude is expected given that larger AuNPs possess larger extinction wavelengths. Interestingly, the trends observed for both peak extinction wavelength and mean particle mass are very similar in behavior, showing an increase in value up to t ≈ 40 min. then a decrease to a final value that stabilizes starting as early as t ≈ 60 min.

Per earlier studies, we attribute the observed trends to the behavior of $AuCl_4^-$ ions in solution during the reaction. It has been identified that CTAC-based AuNPs undergo a growth phase followed by an etching phase based on the balance between $AuCl_4^-$, CTAC, and AA in solution.[156] During the growth phase, AuNP diameter increases, as shown from our data indicating an increase in UV-Vis peak extinction wavelength and an

increase in SP-ICP-MS measured mass up to t = 40 min. This growth is a result of the reducing action of AA on Au^{3+} being added to the reaction in the form of $HAuCl_4$. After this time, the action of AA is diminished in solution and $AuCl_4^-$ interacts with CTAC to form an Au etching compound that acts on AuNPs in solution.[156] The etching of AuNPs results in loss of Au content from their structures. We observe this in our results based on the decrease in UV-Vis peak extinction wavelength and in SP-ICP-MS measured mass after t = 40 min. From our UV-Vis results, we see an evident difference in the rate of both growth and etching based on target AuNP diameter, whereby the larger the target diameter, the more rapidly both growth and etching appear to occur. SP-ICP-MS analysis of other target diameters will illuminate additional relations between target diameter and growth/etching kinetics.

It should be noted the time at which our reaction switches from growth to etching occurs earlier than prior studies.[156] We attribute this to differences in reaction conditions such as reaction temperature. We would also like to note how our findings indicate the importance of purifying CTAC-based AuNPs immediately after synthesis to avoid continued etching and loss of confident in predicted AuNP diameter per the predictive models developed in this study. TEM imaging has been identified as a viable option to further confirm our observations and to further clarify the relation between target AuNP diameter and growth/etching kinetics. We are excited to perform TEM and SP-ICP-MS analysis to add value to this study and provide insight into the growth and etching of CTAC-based AuNPs at the single particle level.[127]

4.5 Conclusions

In this study, we demonstrated how the mean diameter of AuNPs synthesized using citrate-based or CTAC-based seed-mediated growth methods can be predicted based on models relating final diameter with AuNP/Au ratio values. SP-ICP-MS was critical to our analysis as it permitted rapid and accurate measurement of AuNP diameter. Additionally, SP-ICP-MS provided accurate measurements of “on-target” yield of AuNPs in solution, revealing that CTAC-based AuNPs possess more AuNPs of the target diameter across multiple sizes. This revelation, made possible by the single-nanoparticle resolution of SP-ICP-MS technology, points out new research avenues based around identifying how size distribution produces variance in nanoparticle effect in biomedical studies. In our study, we also demonstrated how our models remain accurate in predicting final diameter for scaled up AuNP growth reactions. We concluded by demonstrating how UV-Vis and SP-ICP-MS can be used to measure the change in AuNP size for CTAC-based AuNPs. Our approach to nanoparticle synthesis reaction mathematical model development and nanoparticle growth kinetics quantification can be translated to other nanoparticle synthesis reactions. In time, our hope is that nanoparticle syntheses may be studied in a similar manner for other nanoparticle formulations. In doing so, we may provide greater confidence and uniformity of nanoparticle synthesis and analysis approaches that pave the way for enhanced collaboration and normalized preparation methodologies in nanomedicine studies.

4.6 Acknowledgements and Funding

The authors would like to acknowledge the support of Dr. Steven Foster with the OU Mass Spectrometry, Proteomics & Metabolomics (MSPM) Core for assistance with ICP-MS data collection and instrument access. The authors would also like to acknowledge the support of Dr. Andrew Madden, Dr. Preston Larson, and Dr. Julian Sabisch with the University of Oklahoma (OU) Samuel Roberts Noble Microscopy Laboratory (SRNML) for support with collecting TEM images for this study.

This work was supported in part by awards from NIH COBRE (P20GM135009), NSF CAREER (2048130), and OCAST (HR20-106).

Chapter 5 – Replacing CTAC with Citrate Enables Nanomedicine Applications of Monodisperse Gold Nanoparticles

5.1 Abstract

Citrate-based AuNPs have been commonly employed in nanomedicine studies due to the ease of characterization of gold, the multifunctional nature of AuNPs, and the ease of replacement citrate provides, allowing for easy surface modification. These advantages come at the cost of a wide size distribution that confounds determination of size correlation with observed nano-bio interactions. We have previously shown how CTAC-based AuNPs possess a narrow size distribution. In this study, we have developed a method by which cytotoxic CTAC is replaced with biocompatible citrate using physical replacement methods. Using multiple methods, we confirm the successful removal of CTAC, allowing for ease of surface modification of originally CTAC-based AuNPs. Additionally, we identify differences in surface topology between citrate-based AuNPs and CTAC-based AuNPs. We investigate whether these differences result in changes in surface conjugate saturation density or interactions with serum proteins. Finally, we demonstrate how our modified AuNPs demonstrate biocompatibility based on preliminary cell viability and cell uptake studies. Our results pave the way for a new class of highly monodisperse, highly biocompatible, and highly modifiable AuNPs to be used as the new standard of AuNP model for nanomedicine studies.

This chapter is being prepared as a manuscript for submission to *The Journal of the American Chemical Society* (JACS) – IF 16.383 – as:

Frickenstein A, Whitehead L, Means N, Taffe H, Longacre L, He Y, Sheth V, Butterfield S, Wang L, Wilhelm S, "Ligand Replacement Enables Nanomedicine Applications of Monodisperse Gold Nanoparticles," *JACS*, Jul. 2023

Authors contributions

Alex Frickenstein – Project leader, primary experiment coordinator and performer, primary writer

Luke Whitehead – Original investigator into citrate-PR methodology

Nathan Means – Assisted with nanoparticle synthesis, modification, and ligand conjugation

Haley Taffe – Assisted with nanoparticle synthesis, modification, and ligand conjugation

Logan Longacre – Assisted with nanoparticle synthesis, modification, and ligand conjugation

Yuxin He – Assisted with XTT cell viability, SDS-PAGE, and BCA assay

Vinit Sheth – Assisted with confocal microscopy analysis

Sarah Butterfield – Assisted with batch ICP-MS sample preparation and data collection

Lin Wang – Assisted with collecting SDS-PAGE images

Stefan Wilhelm – Project adviser and corresponding author

5.2 Introduction

Gold nanoparticles (AuNPs) serve as valuable models and multifunctional agents in the field of nanomedicine.[6,9,157] Their ease of synthesis, characterization, and modification allows for multiple methods of quantifying AuNP interactions with biological systems, such as cells. Currently, one of the most commonly used AuNPs in nanomedicine is citrate-based, often synthesized using methods developed by Perrault and Chan.[118] These citrate-based AuNPs are valuable for their innate biocompatibility given the nontoxic nature of citrate molecules on AuNP surface.[158] Some studies have also shown that citrate-based AuNPs can be used as cancer-disrupting agents.[159,160] These advantages of biocompatibility and biofunctionality come at the cost of a wide size distribution resulting from the rapid nature of the reduction that occurs during citrate-based AuNP synthesis. This size distribution can confound analysis of nanoparticle-cell interactions at the single-particle or single-cell level while subsequently complicating expected fate of nanoparticle doses after injection.[161] Implementation of more monodisperse AuNPs for model nanoparticles or clinical application is recommended to increase confidence in expected *in vivo* nanoparticle behavior.

We have previously shown how AuNPs synthesized using an alternative technique that uses cetyltrimethylammonium chloride (CTAC) as a shaping and stabilizing agent possesses improved size monodispersity compared to citrate-based AuNPs. We have provided methods by which CTAC-based AuNPs can be readily synthesized with a high degree of confidence in final AuNP diameter and yield.[Chapter 4] Further, we have shown how CTAC-AuNPs can be modified with PEG using a physical replacement method to impart biocompatibility and biofunctionality on otherwise cytotoxic AuNPs.[31]

While our PEGylation approach of CTAC-based AuNPs is effective, rising concerns about the growing prevalence of PEG immunogenicity warrant investigation into alternative surface modification options for CTAC-based AuNPs.[162,163] In particular, designing a method by which CTAC can be replaced with citrate provides opportunity for more direct comparisons between originally citrate-based AuNPs and originally CTAC-based AuNPs. While other methods for replacing CTAC, or similar molecules like CTAB, with other molecules exist, they are either extremely specific to the molecule replacing CTAC or require intermediate molecules or chemistry that may complicate downstream AuNP modification or biomedical applications.[164-167] A direct way of removing CTAC and replacing it with citrate is necessary for rapid and effective translation of CTAC-based AuNPs into biomedical investigations.

In this study, we identify and incorporate a physical replacement method that effectively removes CTAC from the surface of CTAC-based AuNPs and replaces it with biocompatible citrate molecules. Our method, deemed “citrate physical replacement” (citrate-PR), bears a strong resemblance to our previously used methods for adding PEG to CTAC-based AuNPs but with changes to the replacement solution and the timing of method steps. We demonstrate successful removal of CTAC by multiple means. We similarly show how AuNP monodispersity is maintained throughout our citrate-PR process. Additionally, we show how after CTAC removal, AuNP modification can be performed using standard methods. With CTAC removed, we demonstrate how direct comparison between citrate-based and original CTAC-based AuNPs is more attainable due to having similar surface chemistries. Finally, we show how citrate-PR imparts biocompatibility to originally CTAC-based AuNPs through cell viability and cell uptake

experiments. These results provide the baseline for future studies to use highly monodisperse CTAC-based AuNPs in nanomedicine studies based on the removal of cytotoxic elements being replaced by biocompatible and biofunctional citrate.

5.3 Experimental Section

5.3.1 Synthesis of Gold Nanoparticles

Citrate-based AuNP synthesis was performed using previously detailed methods (Section 4.3.1).[31,118] To have enough material for experimentation, we performed synthesis using 5x scale by volume. We purified AuNPs with two rounds of centrifugation at 1,200 rcf and 4°C. The first centrifugation round was 90 min. using 50 mL centrifugation tubes, the second centrifugation round was 30 min. using 1.5 mL centrifugation tubes. After both rounds of centrifugation, we suspended AuNP pellets in 0.1% Tween20 and 0.01% sodium citrate tribasic dihydrate solutions. We characterized AuNPs using DLS, UV-Vis, and SP-ICP-MS after synthesis.

CTAC-based AuNP synthesis was performed using previously detailed methods (Section 4.3.2.).[31,119] to acquire enough material for experimentation, we performed synthesis using 20x scale by volume. We purified AuNPs with two rounds of centrifugation at 1,200 rcf and 4°C. The first centrifugation round was 90 min. using 50 mL centrifugation tubes, the second centrifugation round was 30 min. using 1.5 mL centrifugation tubes. We resuspended AuNP pellets after the first round of centrifugation using nanopure water. After the second round of centrifugation, we resuspended AuNP pellets in a 20 mM CTAC solution. We characterized AuNPs using DLS, UV-Vis, TEM, and SP-ICP-MS after synthesis.

Previous studies have demonstrated the difference in size and shape between citrate- and CTAC-based AuNPs in two dimensions using TEM.[31,117] From our synthesized and purified citrate- and CTAC-based AuNPs, we concentrated aliquots of AuNP solutions to collect scanning electron microscopy (SEM) images, allowing for

comparison of AuNP size and shape in three dimensions. Concentrated AuNP solutions were dropped onto silicon wafers and imaged using a Zeiss NEON 40 EsB scanning electron microscope.

5.3.2 CTAC removal via Citrate-PR

To remove CTAC and replace it with biocompatible citrate, we modified our previously used method of physical replacement PEGylation (see Section 3.3.4).[31] 60 nm CTAC AuNPs were aliquoted into 1.5 mL centrifuge tubes to a volume of 1000 µL and a concentration of 0.2 nM in 0.1% Tween20. We centrifuged each tube at 1200 rcf for 30 min. at 4°C. After removing supernatant, we added 250 µL of a 1% Tween20 0.005% sodium citrate tribasic dihydrate solution (0.17 mM) to each pellet and sonicated for 10 min. We then vigorously vortexed (~3200 rcf) each tube for 2 min. before adding 750 µL of 1% Tween20 to each tube. This process of centrifugation, sonication, and vortexing was repeated two more times before centrifuging AuNPs one final time before removing supernatant, combining pellets, and resuspending in 0.1% Tween20 0.01% sodium citrate tribasic dihydrate. We collected approximately 500 µL of across multiple tubes at each stage of this process to characterize AuNPs by zeta potential analysis, UV-Vis, and SP-ICP-MS to identify changes in surface chemistry resulting from CTAC removal and citrate presence. Prior to using AuNPs for further experiments, AuNPs were then washed two more times by centrifugation using 0.1% Tween20 and 0.01% sodium citrate tribasic solution for resuspension.

5.3.3 AuNP Characterization During Citrate-PR

There are two principal characteristics we were looking for from AuNPs that had undergone citrate-PR. The first of these was maintained monodispersity expected from CTAC-based AuNPs. During citrate-PR, we characterized AuNPs by DLS to measure any changes in HDD or PDI. Additionally, we measured the extinction spectrum of AuNPs throughout the citrate-PR process as another way of detecting possible AuNP aggregation. We also collected TEM images of post-PR AuNPs to visually observe any differences in AuNP shape, size, stability, or size distribution. Finally, we performed SP-ICP-MS on AuNPs collected before, during, and after the citrate-PR process to identify any possible changes in colloidal stability or size distribution.

The second principal characteristic we examined was extent of CTAC removal following citrate-PR. Given that CTAC is positively charged at neutral pH in water, the removal of CTAC from the surface of AuNPs could be detected by collecting zeta potential estimates of AuNPs. We measured the change in zeta potential throughout the citrate-PR process to determine the effective removal of CTAC and replacement with citrate, which is expected to be negatively charged at neutral pH in water. To further verify CTAC replacement with citrate, we performed agarose gel electrophoresis alongside citrate-based AuNPs of the same target diameter as a positive control. Agarose gel was run using previously established conditions.[32,34] Briefly, we prepared 0.5% agarose gel using 0.5x TBE buffer. We added ~2µL of 150 mg/mL Ficoll to ~10 µL of concentrated AuNP solutions. We added the Ficoll-AuNP mixtures to the wells of the agarose gel. We ran gel electrophoresis at 50 V for 40 min. before imaging the gel.

We also performed Fourier transform infrared (FTIR) spectroscopy to identify CTAC removal. CTAC possesses a quaternary amide group that would register as transmission peaks at wavelengths of 2700 – 3000 cm^{-1} using FTIR.[168-170] We analyzed 60 nm citrate-based AuNPs, 20 mM CTAC solution, as-synthesized 60 nm CTAC-based AuNPs, and post-citrate-PR CTAC-based AuNPs using FTIR to identify any changes in the transmission spectra after our citrate-PR process. FTIR analysis was performed using a Thermo Scientific Nicolet iS-50 with the Attenuated Total Reflection module. We collected a total of 64 scans with a resolution of 1 cm^{-1} for each analyzed sample. We analyzed the collected data using the Omnic Specta software. For each solution, we dropped 20 µL of solution onto the detector of the instrument and let the droplet air dry for 60-90 min. before running the instrument for data collection.

5.3.4 Surface Modification of AuNPs

After performing citrate-PR, the surface of originally CTAC-based AuNPs should be capped with citrate molecules and Tween2- surfactant. Based on prior literature, the surface modification of AuNPs with these surface ligands should be readily modifiable with polyethylene glycol (PEG) molecules that possess reactive sulfide groups, such as maleimide.[128] By comparison, CTAC-based AuNPs are resistant to standard PEGylation methods due to the CTAC bilayer present on the surface of CTAC-based AuNPs following synthesis.[129] To verify existing potential for surface modification, we PEGylated our post-PR CTAC-based 60 nm AuNPs using established methods.[128] We prepared a solution of 5kDa mPEG-SH dissolved in 0.1% Tween20 and added post-PR CTAC-based AuNPs to the solution. We incubated the PEG-AuNP solution for 30 min. at room temperature before characterizing. The concentration of the mPEG-SH and the AuNPs was such that the expected molecular surface density of PEG per nanometers squared (PEG/nm^2) of AuNP surface was 10 PEG/nm^2. We selected this target PEG density to ensure the complete saturation of the AuNP surface per prior literature.[128] We then measured the change in HDD using DLS to verify if PEGylation was successful.

Based on our collected TEM and SEM images, we identified that there was an apparent difference in the geometry and surface topology between citrate- and CTAC-based AuNPs. It is well-stablished that surface curvature of AuNPs can influence the binding density of conjugated surface ligands, such as PEG.[128,171] To determine if the topological differences we observed result in changes in ligand binding densities, we synthesized citrate- and CTAC-based AuNPs within different size ranges – <= 30 nm, between 50 – 70 nm, and => 90 nm – to identify if the surface ligand saturation point

between citrate- and CTAC-based AuNPs differs. These target size ranges were selected based on a prior study analyzing the relation between AuNP diameter and ligand saturation behavior.[128] We synthesized all AuNPs using methods described above. We used diameter predictive models during AuNP synthesis to determine the volume of AuNP seeds to add to achieve target diameter values.[Chapter 4] We performed citrate-PR on all CTAC-based AuNPs using the described method. We proceeded to PEGylate AuNPs as described, aiming for target ligand density values of 0, 0.01, 0.1, 0.5, 1, 2.5, and 5 PEG molecules per nanometers squared (PEG/nm^2). We selected these target PEG surface densities based on prior a prior performing similar analysis.[128] Across each nanoparticle core (citrate-based or CTAC-based), nanoparticle diameter, and targeted PEG density, samples were prepared in triplicate. We then measured the change in HDD for each sample using DLS. We compared the measured HDD value of PEGylated AuNPs to the HDD value of non-PEGylated AuNPs to quantify the change in HDD for each targeted PEG density. We plotted the resulting change in HDD values against targeted PEG density to identify differences in saturation point between citrate-based and CTAC-based AuNPs.

As an alternative surface ligand to PEG, we aimed to assess if heparosan (HEP) could be successfully conjugated onto the surface of post-citrate-PR CTAC-based AuNPs.[32,34,172] We used the pH-salt aging method according to prior literature to perform HEP-conjugation onto the surface of AuNPs.[32,34] We added HCl to nanopure water until the pH was 3.0 as determined by pH probe. We added 13kDa HEP to the acid water followed immediately by either citrate-based AuNPs or post-citrate-PR CTAC-based AuNPs such that the target surface area density of HEP was 10 HEP/nm^2. After

incubating at room temperature for 20 min., we added 3.43 M NaCl solution to the HEP-AuNP solution until the concentration of NaCl was 0.3 M and vortexed the solution. After incubating for 20 min. at room temperature, we added more 3.43. M NaCl solution until the final concentration of NaCl in the HEP-AuNP solution was 0.6 M. We vortexed the solution and incubated for 20 min. at room temperature. We then characterized AuNPs by DLS to verify successful conjugation.

5.3.6 SDS-PAGE and BCA Assays for Protein Corona Analysis

It is well-understood that citrate-based AuNPs can be defined as “quasi-spherical” while CTAC-based AuNPs trend more towards “perfectly spherical” by nature of their respective syntheses.[118,173-175] To identify differences in protein identity or relative protein concentration around the surface of citrate-based or post-citrate-PR CTAC-based AuNPs, we performed SDS-PAGE and the commercial bicinchoninic acid (BCA) assay analysis according to previous protocols.[19,32,34,176] We prepared stock solutions of 60 nm citrate-based AuNPs and post-citrate-PR CTAC-based AuNPs 60 nm. We took aliquots of these stock solutions and modified them with mPEG-SH or HEP as described previously. We prepared AuNPs with two different PEG surface ligand densities, 0.5 PEG/nm^2 or 10 PEG/nm^2, to allow for analysis of protein content on the surface of partially-PEG-saturated and fully-PEG-saturated AuNPs. We thus compared protein content analysis for eight different groups based on two different core nanoparticles (citrate- or CTAC-based) and four different surface chemistries (citrate, 0.5 PEG/nm^2, 10 PEG/nm^2, and HEP). After surface modification, AuNPs were centrifuged twice to remove excess ligand.

For each of the eight groups, we prepared three 1.5 mL tubes of AuNPs with a volume of 1500 µL and a concentration of 0.49 nM. We targeted a total AuNP surface area of 50 cm^2 for each tube to allow for sufficient protein content for analysis.[32,34] We centrifuged all tubes and removed the supernatant. We diluted the resulting AuNP pellets in 20 µL of nanopure water before pipetting the AuNP solutions into 1000 µL of 100% FBS solution in 1.5 mL LoBind tubes. We incubated the AuNP-protein mixtures for 2 hours at 37°C before washing by centrifugation 3 times to remove excess unbound protein. After

each centrifugation, supernatant was removed and the pellet was resuspended in a 1x PBS 0.05% Tween20 solution. After the third wash, we combined pellets from the same group, resuspended to a total volume 1000 µL using 1x PBS 0.05% Tween20 solution, and centrifuged one more time. After removing the supernatant following this centrifugation, we diluted each AuNP pellet using 50 µL of 1x PBS 0.05% Tween20 and we measured the AuNP concentration of each group using UV-Vis. We then diluted all pellets to the same nanomolar concentration using 1x PBS 0.05% Tween20 solution. To isolate bound protein from the surface of the AuNPs, we added 4 µL of 500 mM DTT and 8 µL of 4x LDS to each AuNP solution for every 15 µL of dilute AuNP solution. We then incubated AuNP solutions for 1 hour at 70°C before pelleting the AuNPs by centrifuging at 5,000 rcf for 20 min. at 4°C. We recovered the supernatant from each sample to use in our SDS-PAGE and BCA analysis.

For SDS-PAGE analysis, we used 4-12% NuPAGE™ Bis-Tris precast 1.0 mm protein gels with 12 wells. We mixed 15 µL of the recovered protein supernatant with 6 µL 4x LDS and 3 µL 500 mM DTT (total final volume of 24 µL). A 2% v/v FBS control solution was similarly prepared. We heated the resulting solution to 95°C for 5 min. to denature present protein. We then injected samples into separate wells in the gel. We ran the gel for 55 min. at 200 V before transferring the gel to a fixing solution comprised of 10% acetic acid v/v and 40% ethanol solution v/v. We let the gel fix for 2 hours before rinsing with DI water and staining the gel using 1x SYPROTM Tangerine Protein Gel Stain. We allowed the stain to act on the gel in a light-protected environment for 1 hour. After 1 hour, we rinsed the gel with DI water before imaging the gel using an Azure C600 imaging system.

Before BCA analysis of recovered protein supernatant, we first collected 4 separate 25 µL aliquots of each of the 8 groups (32 total samples) from the original protein supernatant solutions. We added 950 µL of a 10% w/v trichloroacetic acid (TCA) in acetone solution to each aliquot and incubated the resulting solutions overnight at -80°C. We centrifuged the resulting protein precipitates at 18000 rcf for 15 min. at 4°C, removing the supernatant immediately afterwards. We dissolved the newly formed protein pellets using 500 µL of a 0.03% w/v sodium deoxycholate in water solution, vortexing to ensure complete pellet dissolution. We precipitated the protein again by adding 100 µL of a 72% w/v TCA solution in water before incubating the solutions on ice for 30 min. We recovered the protein pellets by centrifuging at 18000 rcf for 15 min. at 4°C, discarding the supernatant. We dissolved the protein pellets once more in 1000µL of chilled 100% acetone and incubated at -80°C for 1 hour. We centrifuged protein solutions one more time at 18000 rcf for 15 min. at 4°C before removing the supernatant and air drying the tubes for ~10 min.

We added 28 µL of a 2% SDS solution in 1x PBS to each dried protein pellet. We added 10 µL of each sample to separate wells of a 96-well plate. We added 50 µL of serially diluted BSA to serve as the protein standard curve. We then added 200 µL of working BCA assay solution to all solution-containing wells of the plate before incubating the plate for 1 hour at 37°C. We used a BioTek Synergy Neo2 Multi-Mode Plate Reader to measure the 562 nm absorbance of each well, comparing our sample measurements against the BSA concentration serial dilution standard curve measured alongside our samples.

5.3.7 Cell Viability and Uptake

CTAC is innately cytotoxic.[120,121] By removing CTAC and replacing it with citrate using our citrate-PR method, we hypothesized there would be a significant difference in cell viability compared to as-synthesized CTAC-based AuNPs. To test this, we performed an XTT cell viability assay. We seeded 10,000 cells/well of RAW 264.7 murine macrophages into a 96 wells plate in 100 µL of DMEM with 1% pen-strep and 10% FBS. We let the cells incubate overnight before adding 150 µL of 0.1 nM AuNP solution to each well. For this assay, we used the following AuNP groups: unmodified citrate-based AuNPs, PEGylated citrate-based AuNPs (10 PEG/nm^2 target surface density using 5 kDa mPEG-SH), and HEP-conjugated citrate-based AuNPs (10 HEP/nm^2 target surface density using 13 kDa HEP), as-synthesized CTAC-based AuNPs, citrate-PR CTAC-based AuNPs, PEGylated citrate-PR CTAC-based AuNPs (10 PEG/nm^2 target surface density using 5 kDa mPEG-SH), and HEP-conjugated citrate-PR CTAC-based AuNPs (10 HEP/nm^2 target surface density using 13 kDa HEP). For all AuNP formulations, we used 60 nm target diameter AuNPs. We washed all AuNP groups 2 times by centrifugation prior to treating cells to ensure complete removal of any excess unbound ligand molecules. Before adding AuNP doses to cell wells, we incubated the AuNPs in media for 30 min. at 37°C. After incubating cells with AuNP doses for 24 hours, we removed the AuNP-containing media and rinsed each well with 1x PBS two times. We used the XTT assay (2,3-Bis-(2-Methoxy-4-Nitro-5-Sulfophenyl)-2H-Tetrazolium-5-Carboxanilide) method according to the manufacturer's instructions to assess cell viability by measuring the absorbance of formazan in dimethyl sulfoxide (DMSO) at 570 nm using a plate reader. We normalized absorbance values from each AuNP group to the cell-only

group after subtracting background absorbance resulting from the well-plate or remaining media.

To collect qualitative images supporting our XTT viability data, we prepared samples for confocal laser scanning microscopy (CLSM) according to prior methods.[25] We used ~20 mL of a 3:1 v/v mixture of sulfuric acid and hydrogen peroxide to clean 18 mm round microscopy coverslips by immersing the coverslips in the solution for ~15 min. We rinsed the clean coverslips by thorough rinsing with nanopure water before placing them in a 12-well plate. We treated the 12-well plate with the coverslips using UV light for 10 min before adding 20,000 cells/well to each well with a coverslip. We added the cells in 500 µL of DMEM with 1% pen-strep and 10% FBS. We gave the cells 24 hours to adhere to the coverslips before adding 150 µL of 0.01 nM AuNP solution. We matched the AuNP solutions and media incubation time from our XTT assay analysis, but we did not include as-synthesized CTAC-based AuNPs as an experimental group. We incubated the cells with AuNPs for 24 hours before media was removed and washed coverslips three times with 1x PBS. We added 500 µL 4% paraformaldehyde at room temperature for 10 minutes to fix cells before staining the cells using DAPI and WGA according to the manufacturer's protocols to label the cell nuclei and membrane, respectively. We used a ZEISS LSM 880 inverted confocal laser microscope with a 63x oil immersion objective (1.4 NA) to collect all images. We applied previously detailed light scattering principles of AuNPs to detect nanoparticle presence inside of imaged cells.[144,145]

5.4 Results and Discussion

5.4.1 Assessing Success of Citrate-PR Method

Removal of CTAC is vital to the biomedical applicability of CTAC-based AuNPs given the cytotoxic nature of CTAC.[120,121] Citrate is a prime choice for a replacement molecule given its innate biocompatibility and the relative ease with which citrate is removed from the surface of AuNPs when conjugating surface ligands.[118] The driving force behind our citrate-PR method is physically removing CTAC from the surface of CTAC-based AuNPs in an environment that supports colloidal stability and allows for citrate molecules to associate with the surface of the AuNPs. Towards this end, we utilize sonication and high speed vortexing to facilitate disruption of the CTAC bilayer around the surface of the CTAC-based AuNPs in a solution that has a high Tween20 content. Tween20 acts as a stabilizing agent to keep AuNPs from aggregating during the citrate-PR process. Simultaneously, the removal of CTAC by way of sonication, vortexing, and washing by centrifugation allows for Tween20 and citrate molecules to associated with the AuNP surface. Repeating this process several times increases confidence in the complete removal of CTAC and the assumed saturation of the AuNP surface with citrate molecules.

To fully validate success of our citrate-PR method, there are two characteristics we looked for. Firstly, we wanted to identify if the colloidal stability and monodispersity of AuNPs was altered during our citrate-PR process. To measure stability and monodispersity, we measured our CTAC-based AuNPs before and after citrate-PR using DLS, UV-Vis, TEM, and SP-ICP-MS (Figure 5.1). For our study, we synthesized CTAC-based AuNPs of target diameter 60 nm (Figure C5.1).

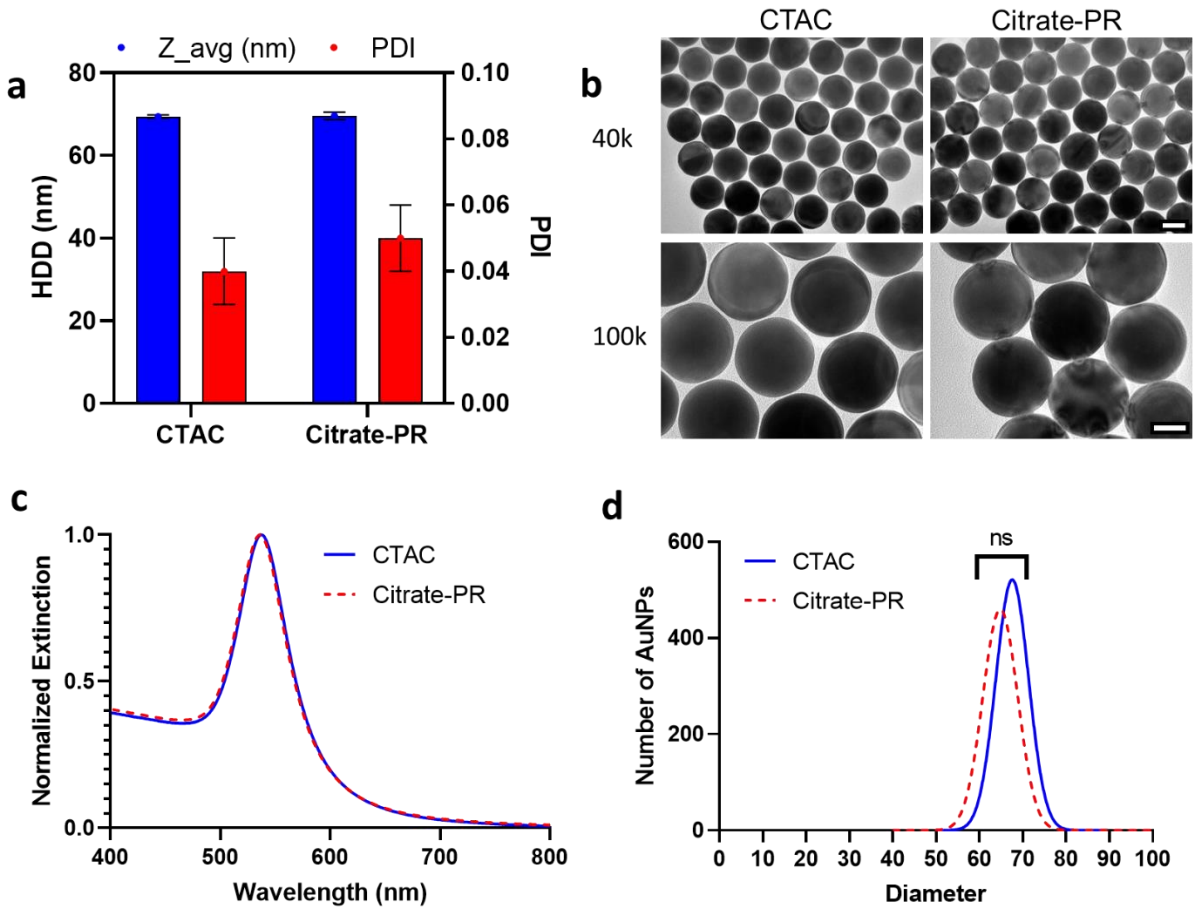

Figure 5.1: Measuring colloidal stability and monodispersity of AuNPs after citrate-PR. a) Representative HDD and PDI measurements of CTAC-based AuNPs before and after citrate-PR. Blue bars represent HDD measurements, red bars represent PDI estimates. Black bars indicate standard deviation. **b)** Low and high magnification TEM images of CTAC-based AuNPs before and after citrate-PR. 40k scale bar is 50 nm, 100k scale bar is 30 nm. **c)** UV-Vis normalized extinction spectra for CTAC-based AuNPs before and after citrate-PR. **d)** SP-ICP-MS normalized Gaussian distribution of AuNP diameter estimates of CTAC-based AuNPs before and after citrate-PR. N = 1000 for number of AuNPs measured. Kolmogorov-Smirnov statistical test run to determine if distributions differ in a statistically significant way. ns = no statistical significance.

Polydispersity index (PDI) is a preliminary indicator of changes in colloidal stability that result from aggregation of nanoparticles.[117,177] Based on our DLS measurements (Figure 5.1a), there is no observable difference between the HDD or PDI of our AuNPs before or after citrate-PR. While we may have expected the HDD to decrease slightly as a result of the CTAC bilayer being removed by our citate-PR process, we attribute the maintained HDD value to the presence of the surfactant Tween20, which is known to increase HDD based on measurement mechanics of DLS.[153] Similarly, no observable change in AuNP core shape or size is observed by TEM (Figure 5.1b). Interestingly, at higher magnification (100k), we observe the distance between AuNPs decreases after AuNPs undergo citrate-PR. Likely, this phenomenon is a result of the difference in size between citrate molecule and CTAC. The CTAC bilayer keeps nearby AuNPs further away compared to the smaller citrate molecules. Quantifying the relative distance between AuNPs before and after citrate-PR could prove an interesting exercise in studying inter-nanoparticle spaces and the correlating relationship between the size and steric hindrance of surface-associated molecules. UV-Vis analysis, which can show AuNP aggregation [117], corroborates lack of aggregation based on the maintained width of the normalized extinction spectrum (Figure 5.1c, Figure C5.2). Finally, SP-ICP-MS measurements of CTAC-based AuNPs before and after citrate-PR demonstrate no statistical significance in the AuNP diameter distribution (Figure 5.1d, Figure C5.3). By all of these metrics, we determine that our citrate-PR process successfully maintains the monodispersity of CTAC-based AuNPs. By this, CTAC-based AuNPs may be modified using our citrate-PR method to remove cytotoxic CTAC and replace it with biocompatible citrate while maintaining the narrow size distribution associated with CTAC-based AuNPs.

Having demonstrated successful maintaining of CTAC-based AuNP monodispersity, our next step was to verify complete CTAC removal. To accomplish these, we performed zeta potential measurements, agarose gel electrophoresis, and FTIR spectroscopy (Figure 5.2).

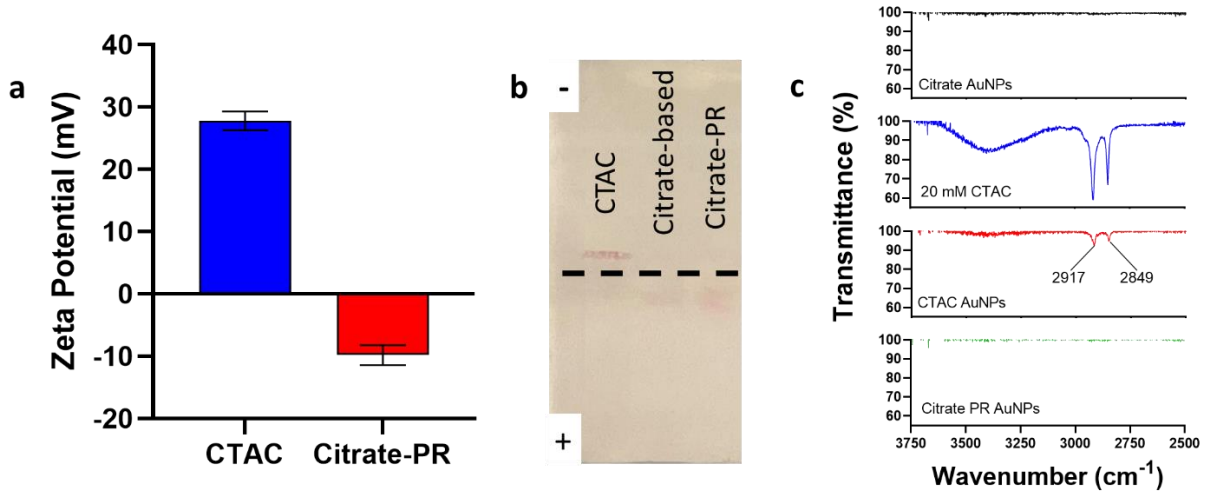

Figure 5.2: Assessing removal of CTAC following citrate-PR. a) Zeta potential measurements of CTAC-based AuNPs before and after citrate-PR. Black error bars indicate standard deviation. **b)** Agarose gel electrophoresis of CTAC-based AuNPs before and after citrate-PR. Citrate-based AuNPs of the same target diameter were used as a positive control. The negative sign denotes the cathode, and the positive sign denotes the anode. The dshed line indicates the location of the original gel wells. **c)** FTIR spectroscopy analysis of CTAC-based AuNPs before and after citrate-PR. Citrate-based AuNPs and 20 mM CTAC solution were also measured for a negative and positive control, respectively. The transmittance peak values noted in the CTAC AuNPs spectrum are also observed in the 20 mM CTAC spectrum, with the latter having similar transmittance peak values.

Similar to results from prior studies, our zeta potential data demonstrates a decrease in zeta potential, going from a positive to a negative value (Figure 5.2a, Figure C5.4).[31] Given the positive charge associated with CTAC, the decrease in zeta potential value is a strong indicator of CTAC removal from the surface of CTAC-based AuNPs as a result of our citrate-PR process. Our agarose gel electrophoresis results corroborate our zeta potential findings (Figure 5.2b). Here, we see that our as-synthesized CTAC-based AuNPs (left lane) aggregated upon running of the agarose gel electrophoresis. By comparison, both the citrate-based AuNPs and the CTAC-based post-citrate-PR AuNPs demonstrated similar distances moved and movement in the same direction (towards the positively charged anode). The combination of these results indicate that CTAC has been successfully removed from the surface and the post-citrate-PR CTAC-based AuNPs behave similarly to citrate-based AuNPs of the same target diameter. Finally, our FTIR spectroscopy confirms that CTAC is absent from the surface of CTAC-based AuNPs after they undergo our citrate-PR method (Figure 5.2c). The combination of these data suggests that CTAC is successfully removed from the surface of CTAC-based AuNPs that undergo citrate-PR. Further, in combination with our data from Figure 5.1, we recognize that this complete CTAC removal does not come at the cost of losing the superior monodispersity observed in CTAC-based AuNPs. Thus, through our data, we see that the two principle characteristics we sought to demonstrate following citrate-PR – maintained monodispersity and removal of CTAC – are present in post-citrate-PR CTAC-based AuNPs.

5.4.2 Identifying Possible Differences in Surface Behavior

The development of our citrate-PR method allows for more direct comparison between as-synthesized citrate-based and post-citrate-PR CTAC-based AuNPs. After citrate-PR, CTAC-based AuNPs can be assumed to possess the same surface chemistry as originally synthesized citrate-based AuNPs. Based on our SEM images (Figure 5.3a), we identified there are surface topological differences between citrate-based and CTAC-based AuNPs. We sought to identify if these topological differences result in any changes in surface ligand density saturation or in interactions between AuNPs and serum proteins (Figure 5.3). We used previously quantified 60 nm citrate-based AuNPs for our analysis (Figure 4.4). Conjugation of PEG and HEP was verified using DLS quantification of HDD (Figure C5.5, Table D5.1).

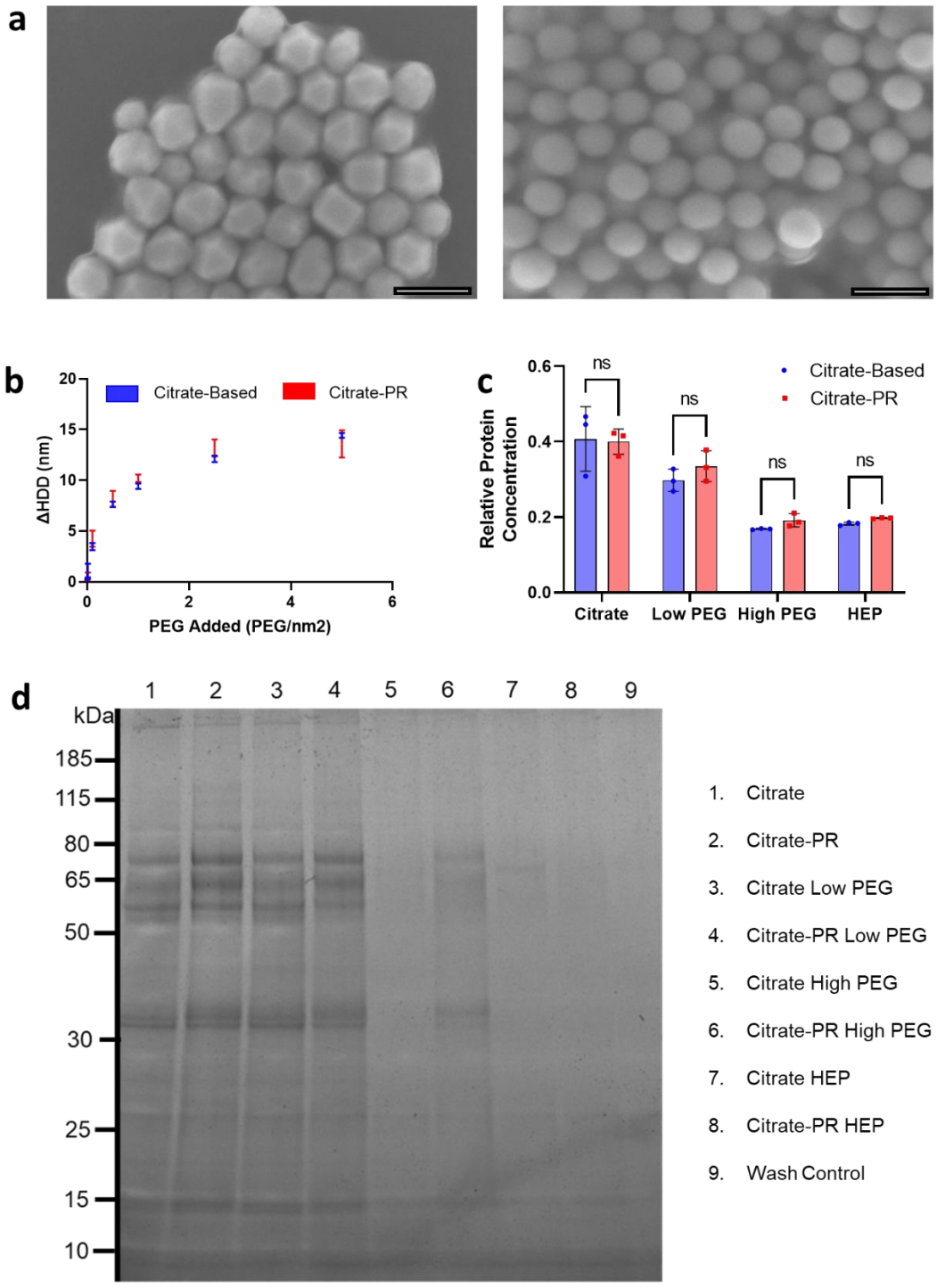

Figure 5.3: Assessing surface behavior differences between citrate-based AuNPs and post-citrate-PR CTAC-based AuNPs. a) SEM images of citrate-based (left) and CTAC-based (right) AuNPs. Scale bar is 100 nm. **b)** Change in HDD (ΔHDD) with increasing PEG added. Mean values with error bars are shown. **c)** BCA assay relative protein concentration for analyzed groups. One-way standard ANOVA was run to assess statistical significance. ns = no statistical significance. **d)** SDS-PAGE gel reveals protein content of analyzed samples. The legend on the right-hand side clarifies sample identity.

The surface topology difference between the AuNP types is clear from the SEM image (Figure 5.3a). Citrate-based AuNPs more resemble three-dimensional polygonal shaped, possessing faces, edges, and corners. In contrast, CTAC-based AuNPs are more spherical in shape, possessing round and curved surfaces. Largely, this difference in topology is most likely a result of the shaping effect of the CTAC bilayer during the synthesis of CTAC-based AuNPs.

To determine if the difference in surface topology influenced surface ligand density saturation, we performed PEG saturation analysis similar to prior studies.[128] We plotted our results in terms of the change in HDD with the change in PEG added. Based on the data, we conclude there is not significant difference between PEG saturation points between citrate-based and post-citrate-PR CTAC-based AuNPs. This lack of a difference could be attributed to a couple possible factors. Firstly, as we have previously shown, the size distribution of citrate-based AuNPs is very wide, making direct size-to-size comparison challenging. Secondly, DLS scattering is influenced more by larger particles in solution. Citrate-based AuNPs possess AuNPs larger than the target diameter by nature of their large size distribution. It is possible that these larger AuNPs shifts the HDD estimate higher. An alternative means of measuring PEG saturation could reveal possible differences between the two AuNP types, though DLS has historically proven an accurate method for such assessment.

Understanding protein interactions with nanoparticles of different surface properties can inform nanoparticle behavior and fate *in vivo.*[178] As with our PEG saturation curves, our results from the BCA assay (Figure 5.3c) and the SDS-PAGE gel (Figure 5.3d) seem to indicate no difference between the two AuNP populations across

multiple surface chemistries in terms of relative protein amount or in terms of relative protein composition. As with the PEG analysis, we are using batch-based methods of analyzing AuNP-protein interactions. Identifying a means of analyzing PEG-AuNP or protein-AuNP interactions at the single particle level may reveal more of a difference between the citrate-based and CTAC-based AuNPs based on the significant difference in size and shape distributions. Further analysis in this is recommended to identify if the difference in surface topology truly results in no statistical significance in terms of interactions between AuNPs and surface ligands or serum proteins.

5.4.3 Cell Viability and Cell Uptake

As a final verification of complete CTAC removal and confirmation of imparted biocompatibility, we performed *in vitro* analysis of cell viability and AuNP uptake by RAW 264.7 murine macrophages based on established protocols (Figure 5.4).

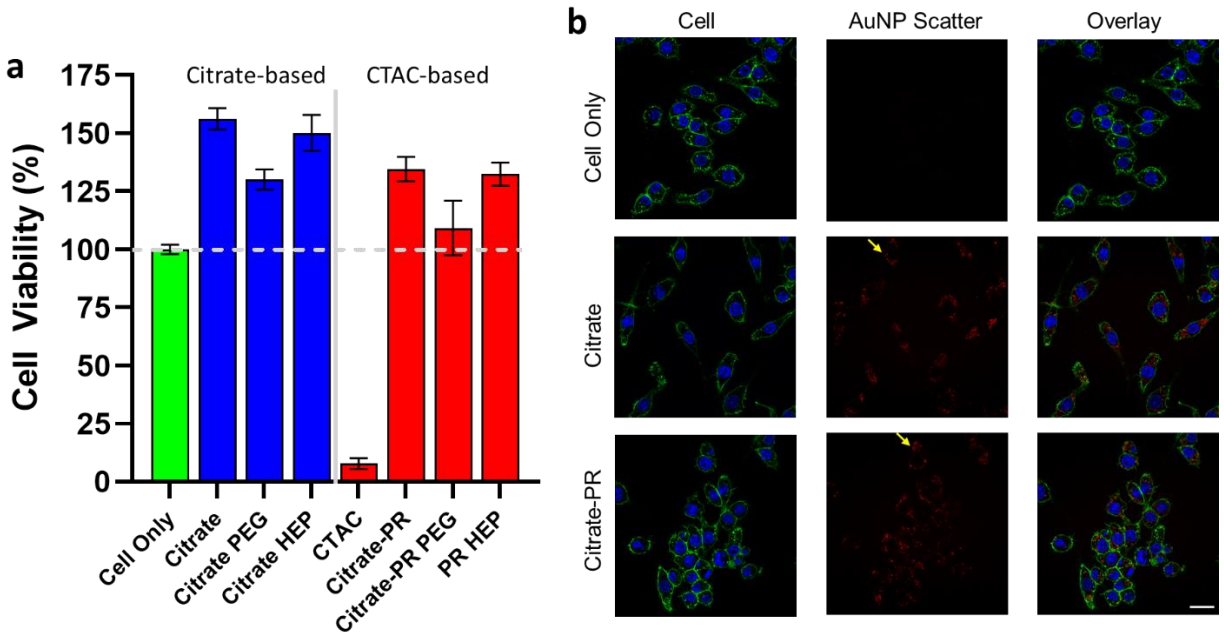

Figure 5.4: Cell Viability and Cell Uptake Analysis Post-Citrate-PR: a) XTT assay cell viability results. Green represents cell-only control, blue is for citrate-based AuNP groups, and red is for CTAC-based AuNP groups. Values shown are mean cell viability with black error bars representing standard deviation. **b)** CLSM images of RAW 264.7 murine macrophages treated with citrate-based AuNPs or post-citrate-PR CTAC-based AuNPs. Blue shows the cell nucleus (DAPI), green shows the cell membrane, and red shows scattering of light caused by AuNPs. Yellow arrows point to locations of scattering resulting from AuNP presence. Scale bar is 20 µm.

From our cell viability study (Figure 5.4a), it is clear that the citrate-PR group possesses a higher cell viability % value than as-synthesized CTAC-based AuNPs. From this, we can conclude that our citrate-PR method imparts biocompatibility to CTAC-based AuNPs. The data we observe across other sure chemistries is similarly promising, whereby trends in PEG- and HEP-coated AuNPs between citrate- and CTAC-based AuNPs are similar. It should be noted that the increased cell viability observed in most AuNP-treated groups is not necessarily representative of cells growing more favorably in environments with AuNPs. XTT assay data is collected by measuring absorbance, which AuNPs contribute to. Thus, what we are truly measuring is cell viability plus absorbance contributed from AuNPs. Additionally, it is worth noting that across all surface chemistries (citrate, PEG, and HEP), citrate-based AuNPs demonstrate higher mean cell viability % values. Based on our discussion of absorbance and what we know about the size distribution of citrate-based AuNPs from UV-Vis extinction data, it is reasonable to conclude the higher viability values stem from higher absorbance values associated with larger AuNPs within the size distribution of citrate-based AuNPs contributing greatly to the observed absorbance value. Given that such large AuNPs do not exist in the CTAC-based AuNP group due to the narrow size distribution of CTAC-based AuNPs, the apparent cell viability % values are seemingly lower.

CLSM imaging (Figure 5.4b, Figure C5.6) reveals qualitative nanoparticle uptake by the RAW 264.7 murine macrophages. Light scattering reveals the location and relative amount of AuNPs within cells.[25,144,145] Based on the apparent scattering in both citrate-based and citrate-PR groups, it appears the AuNP uptake behavior is similar between the two AuNP types. This further demonstrates that our citrate-PR is effective at a) removing

CTAC from the surface of CTAC-based AuNPs and b) promotes similar behavior to citrate-based AuNPs.

A more quantitative study to identify differences in AuNP uptake between citrate- and CTAC-based AuNPs is now possible based on our current discoveries. Performing a batch ICP-MS study to identify how the improved monodispersity of CTAC-AuNPs could reveal avenues for further demonstrating the advantages of CTAC-AuNPs narrow size distribution in a nanomedicine context. We note this exciting opportunity and look forward to exploring it more in the near future.

5.5 Conclusions

In this work, we developed a method by which CTAC can be removed from the surface of CTAC-based AuNPs. Through our testing, we identified that our citrate-PR method completely removes CTAC from the surface of CTAC-based AuNPs while maintaining the size monodispersity associated with CTAC-based AuNPs. We also demonstrated that despite the apparent differences in surface topology, there is no apparent difference using batch-based analysis (i.e., DLS, BCA assay) in either ligand conjugation saturation or in nanoparticle-protein interactions. That said, we did demonstrate that our citrate-PR method imparts biocompatibility to CTAC-based AuNPs based on qualitative cell-viability and cell uptake experiments. Additional work in quantifying the exact differences between citrate- and CTAC-based AuNPs on a nano-bio interaction level, such as through a quantitative cell uptake experiment, is an immediate future step for this study. Beyond this, exploring *in vivo* differences in biodistribution or clinical effect between the two AuNP types could reveal exciting new applications for our new class of highly monodisperse, biocompatible, and biofunctional AuNPs.

5.6 Acknowledgements

Special thanks to Dr. Paul DeAngelis for providing the heparoson used in this study. Thanks also to Dr. Steven Foster and the Mass Spectrometry, Proteomics, and Metabolomics (MSPM) Core for assistance in ICP-MS data collection. The authors would like to thank Dr. Preston Larson and Dr. Julian Sabisch for assistance in collecting TEM and SEM images used in this study. The authors also acknowledge Dr. Ben Fowler and the Oklahoma Medical Research Foundation (OMRF) for support in confocal microscopy.

This work was supported in part by awards from NIH COBRE (P20GM135009), NSF CAREER (2048130), and OCAST (HR20-106).

Chapter 6 – Conclusions and Future Directions

Through this work, I have shown the significant difference that exists between the AuNP core of citrate-based and CTAC-based AuNPs. I have also demonstrated multiple methods by which CTAC may be removed and replaced with more biocompatible and biofunctional alternatives. By encouraging the nanomedicine community to use CTAC-based AuNPs in place of the citrate-based AuNPs, nanomedicine researchers may use a more monodisperse AuNP model formulation that contains less size variance relative to the target synthesized diameter. This more accurate nanoparticle model could provide useful insight as the nanomedicine community continues to learn more about nano-bio interactions. Additionally, the narrower size distribution may have other uses such as with single-nanoparticle-based diagnostics.

There are several future directions for this research. In the short-term, we have identified that quantifying cellular uptake of post-PR AuNPs provides comparison between nano-bio interactions between citrate-based and post-citrate-PR CTAC-based AuNPs. This study would aim to measure how differences in AuNP monodispersity may influence magnitude or consistency in cellular uptake of AuNPs. The effects of size, surface chemistry, and concentration could all be measured and compared between citrate-based and CTAC-based AuNPs that have undergone our citrate-PR process. We hypothesize that the observed standard deviation in cellular uptake will significantly differ between citrate- and CTAC-based AuNPs across size, surface chemistry, and concentration for treated cells.

Longer-term, our outline for quantifying predictive models for AuNP growth can be applied to other nanoparticle synthesis approaches, allowing for uniformity in nanoparticle

synthesis approaches while increasing confidence in synthesis results based on reaction inputs. Over time, the development of more prevalent and accurate models could pave the way for more accessible and well-understood nanoparticle synthesis approaches across the field of nanomedicine.

Finally, the key discovery that incentivized this study was that CTAC-based AuNPs have a much tighter mass (and subsequent size) distribution compared to citrate-based AuNPs using single particle analytical techniques such as SP-ICP-MS. By using this fact in bioanalytical or diagnostic assays, the sensitivity and accuracy of such assays may be improved over current approaches.

References

1. Zhang, C.; Yan, L.; Wang, X.; Zhu, S.; Chen, C.; Gu, Z.; Zhao, Y. Progress, challenges, and future of nanomedicine. In *Nano Today*, Elsevier B.V.: 2020; Vol. 35.
2. Đorđević, S.; Gonzalez, M.M.; Conejos-Sánchez, I.; Carreira, B.; Pozzi, S.; Acúrcio, R.C.; Satchi-Fainaro, R.; Florindo, H.F.; Vicent, M.J. Current hurdles to the translation of nanomedicines from bench to the clinic. *Drug Delivery and Translational Research* **2022**, *12*, 500-525, doi:10.1007/s13346-021-01024-2.
3. Mo, S.; Tang, P.; Luo, W.; Zhang, L.; Li, Y.; Hu, X.; Ma, X.; Chen, Y.; Bao, Y.; He, X., et al. Patient-Derived Organoids from Colorectal Cancer with Paired Liver Metastasis Reveal Tumor Heterogeneity and Predict Response to Chemotherapy. *Advanced Science* **2022**, *9*, doi:10.1002/advs.202204097.
4. Soares, S.; Sousa, J.; Pais, A.; Vitorino, C. Nanomedicine: Principles, Properties, and Regulatory Issues. *Frontiers in Chemistry* **2018**, *6*.
5. Mitchell, M.J.; Billingsley, M.M.; Haley, R.M.; Wechsler, M.E.; Peppas, N.A.; Langer, R. Engineering precision nanoparticles for drug delivery. *Nature Reviews Drug Discovery* **2021**, *20*, 101-124, doi:10.1038/s41573-020-0090-8.
6. Sibuyi, N.R.S.; Moabelo, K.L.; Fadaka, A.O.; Meyer, S.; Onani, M.O.; Madiehe, A.M.; Meyer, M. Multifunctional Gold Nanoparticles for Improved Diagnostic and Therapeutic Applications: A Review. *Nanoscale Research Letters* **2021**, *16*, 174, doi:10.1186/s11671-021-03632-w.
7. Anselmo, A.C.; Mitragotri, S. Nanoparticles in the clinic. *Bioengineering & Translational Medicine* **2016**, *1*, 10-29, doi:https://doi.org/10.1002/btm2.10003.
8. Anselmo, A.C.; Mitragotri, S. Nanoparticles in the clinic: An update. *Bioengineering & Translational Medicine* **2019**, *4*, doi:10.1002/btm2.10143.
9. Hu, X.; Zhang, Y.; Ding, T.; Liu, J.; Zhao, H. Multifunctional Gold Nanoparticles: A Novel Nanomaterial for Various Medical Applications and Biological Activities. *Frontiers in Bioengineering and Biotechnology* **2020**, *8*.
10. Hua, S.; de Matos, M.B.C.; Metselaar, J.M.; Storm, G. Current trends and challenges in the clinical translation of nanoparticulate nanomedicines: Pathways for translational development and commercialization. In *Frontiers in Pharmacology*, Frontiers Media S.A.: 2018; Vol. 9.
11. Rennick, J.J.; Johnston, A.P.R.; Parton, R.G. Key principles and methods for studying the endocytosis of biological and nanoparticle therapeutics. In *Nature Nanotechnology*, Nature Research: 2021; Vol. 16, pp 266-276.
12. Wu, M.; Guo, H.; Liu, L.; Liu, Y.; Xie, L. Size-dependent cellular uptake and localization profiles of silver nanoparticles. *Int J Nanomedicine* **2019**, *14*, 4247-4259, doi:10.2147/IJN.S201107.
13. Frickenstein, A.N.; Hagood, J.M.; Britten, C.N.; Abbott, B.S.; McNally, M.W.; Vopat, C.A.; Patterson, E.G.; MacCuaig, W.M.; Jain, A.; Walters, K.B., et al. Mesoporous Silica Nanoparticles: Properties and Strategies for Enhancing Clinical Effect. In *Pharmaceutics*, 2021; Vol. 13.
14. Foroozandeh, P.; Aziz, A.A. Insight into Cellular Uptake and Intracellular Trafficking of Nanoparticles. *Nanoscale Research Letters* **2018**, *13*, 339, doi:10.1186/s11671-018-2728-6.

15. Xie, X.; Liao, J.; Shao, X.; Li, Q.; Lin, Y. The Effect of shape on Cellular Uptake of Gold Nanoparticles in the forms of Stars, Rods, and Triangles. *Scientific Reports* **2017**, *7*, 3827, doi:10.1038/s41598-017-04229-z.
16. Yue, J.; Feliciano, T.J.; Li, W.; Lee, A.; Odom, T.W. Gold Nanoparticle Size and Shape Effects on Cellular Uptake and Intracellular Distribution of siRNA Nanoconstructs. *Bioconjugate Chemistry* **2017**, *28*, 1791-1800, doi:10.1021/acs.bioconjchem.7b00252.
17. Vincent, M.P.; Bobbala, S.; Karabin, N.B.; Frey, M.; Liu, Y.; Navidzadeh, J.O.; Stack, T.; Scott, E.A. Surface chemistry-mediated modulation of adsorbed albumin folding state specifies nanocarrier clearance by distinct macrophage subsets. *Nature Communications* **2021**, *12*, 648, doi:10.1038/s41467-020-20886-7.
18. Abdelkhaliq, A.; van der Zande, M.; Punt, A.; Helsdingen, R.; Boeren, S.; Vervoort, J.J.M.; Rietjens, I.M.C.M.; Bouwmeester, H. Impact of nanoparticle surface functionalization on the protein corona and cellular adhesion, uptake and transport. *Journal of Nanobiotechnology* **2018**, *16*, 70, doi:10.1186/s12951-018-0394-6.
19. Walkey, C.D.; Olsen, J.B.; Guo, H.; Emili, A.; Chan, W.C.W. Nanoparticle Size and Surface Chemistry Determine Serum Protein Adsorption and Macrophage Uptake. *Journal of the American Chemical Society* **2012**, *134*, 2139-2147, doi:10.1021/ja2084338.
20. Wilhelm, S.; Bensen, R.; Kothapalli, R.; Burgett, A.; Merrifield, R.; Stephan, C. Quantification of Gold Nanoparticle Uptake into Cancer Cells using Single Cell ICP-MS. *PerkinElmer Appl Note* **2018**.
21. Donahue, N.D.; Sheth, V.; Frickenstein, A.N.; Holden, A.; Kanapilly, S.; Stephan, C.; Wilhelm, S. Absolute Quantification of Nanoparticle Interactions with Individual Human B Cells by Single Cell Mass Spectrometry. *Nano Letters* **2022**, *22*, 4192-4199, doi:10.1021/acs.nanolett.2c01037.
22. Murschhauser, A.; Röttgermann, P.J.F.; Woschée, D.; Ober, M.F.; Yan, Y.; Dawson, K.A.; Rädler, J.O. A high-throughput microscopy method for single-cell analysis of event-time correlations in nanoparticle-induced cell death. *Communications Biology* **2019**, *2*, doi:10.1038/s42003-019-0282-0.
23. Steinke, M.; Zunhammer, F.; Chatzopoulou, E.I.; Teller, H.; Schütze, K.; Walles, H.; Rädler, J.O.; Grüttner, C. Rapid Analysis of Cell–Nanoparticle Interactions using Single-Cell Raman Trapping Microscopy. *Angewandte Chemie International Edition* **2018**, *57*, 4946-4950, doi:https://doi.org/10.1002/anie.201713151.
24. Gupta, P.; Rai, N.; Verma, A.; Gautam, V. Microscopy based methods for characterization, drug delivery, and understanding the dynamics of nanoparticles. *Medicinal Research Reviews* **2023**, *n/a*, doi:https://doi.org/10.1002/med.21981.
25. Sheth, V.; Chen, X.; Mettenbrink, E.M.; Yang, W.; Jones, M.A.; M'Saad, O.; Thomas, A.G.; Newport, R.S.; Francek, E.; Wang, L., et al. Quantifying Intracellular Nanoparticle Distributions with Three-Dimensional Super-Resolution Microscopy. *ACS Nano* **2023**, *17*, 8376-8392, doi:10.1021/acsnano.2c12808.
26. McKinnon, K.M. Flow cytometry: An Overview. *Curr Protoc Immunol* **2019**, 10.1002/cpim.40, 1-5, doi:10.1002/cpim.40.
27. Adan, A.; Alizada, G.; Kiraz, Y.; Baran, Y.; Nalbant, A. Flow cytometry: basic principles and applications. *Critical Reviews in Biotechnology* **2017**, *37*, 163-176, doi:10.3109/07388551.2015.1128876.

28. Geethalakshmi, R.; Nivaz, S.R.; Lekshmi, G.S.; Surendhiran, D.; Hussain, C.M.; Sirajunnisa, A.R. Chapter 6 - Utilization of flow cytometry in nanomaterial/bionanomaterial detection. In *Handbook of Microbial Nanotechnology*, Hussain, C.M., Ed. Academic Press: 2022; https://doi.org/10.1016/B978-0-12-823426-6.00016-4pp. 133-144.
29. Wilschefski, S.C.; Baxter, M.R. Inductively Coupled Plasma Mass Spectrometry: Introduction to Analytical Aspects. *Clin Biochem Rev* **2019**, *40*, 115-133, doi:10.33176/AACB-19-00024.
30. Chemnitzer, R. Strategies for Achieving the Lowest Possible Detection Limits in ICP-MS. *Spectroscopy* **2019**, *34*, 12-16.
31. Frickenstein, A.N.; Mukherjee, S.; Harcourt, T.; He, Y.; Sheth, V.; Wang, L.; Malik, Z.; Wilhelm, S. Quantification of monodisperse and biocompatible gold nanoparticles by single-particle ICP-MS. *Anal Bioanal Chem* **2023**, 10.1007/s00216-023-04540-x, doi:10.1007/s00216-023-04540-x.
32. Yang, W.; Wang, L.; Fang, M.; Sheth, V.; Zhang, Y.; Holden, A.M.; Donahue, N.D.; Green, D.E.; Frickenstein, A.N.; Mettenbrink, E.M., et al. Nanoparticle Surface Engineering with Heparosan Polysaccharide Reduces Serum Protein Adsorption and Enhances Cellular Uptake. *Nano Lett* **2022**, *22*, 2103-2111, doi:10.1021/acs.nanolett.2c00349.
33. Zhang, Y.; Elechalawar, C.K.; Yang, W.; Frickenstein, A.N.; Asfa, S.; Fung, K.M.; Murphy, B.N.; Dwivedi, S.K.; Rao, G.; Dey, A., et al. Disabling partners in crime: Gold nanoparticles disrupt multicellular communications within the tumor microenvironment to inhibit ovarian tumor aggressiveness. *Mater Today (Kidlington)* **2022**, *56*, 79-95, doi:10.1016/j.mattod.2022.01.025.
34. Yang, W.; Frickenstein, A.N.; Sheth, V.; Holden, A.; Mettenbrink, E.M.; Wang, L.; Woodward, A.A.; Joo, B.S.; Butterfield, S.K.; Donahue, N.D., et al. Controlling Nanoparticle Uptake in Innate Immune Cells with Heparosan Polysaccharides. *Nano Lett* **2022**, *22*, 7119-7128, doi:10.1021/acs.nanolett.2c02226.
35. Noireaux, J.; Grall, R.; Hullo, M.; Chevillard, S.; Oster, C.; Brun, E.; Sicard-Roselli, C.; Loeschner, K.; Fisicaro, P. Gold Nanoparticle Uptake in Tumor Cells: Quantification and Size Distribution by sp-ICPMS. *Separations* **2019**, *6*, doi:10.3390/separations6010003.
36. Merrifield, R.C.; Stephan, C.; Lead, J.R. Quantification of Au Nanoparticle Biouptake and Distribution to Freshwater Algae Using Single Cell – ICP-MS. *Environmental Science & Technology* **2018**, *52*, 2271-2277, doi:10.1021/acs.est.7b04968.
37. López-Serrano Oliver, A.; Baumgart, S.; Bremser, W.; Flemig, S.; Wittke, D.; Grützkau, A.; Luch, A.; Haase, A.; Jakubowski, N. Quantification of silver nanoparticles taken up by single cells using inductively coupled plasma mass spectrometry in the single cell measurement mode. *Journal of Analytical Atomic Spectrometry* **2018**, *33*, 1256-1263, doi:10.1039/C7JA00395A.
38. Zanoni, I.; Crosera, M.; Pavoni, E.; Adami, G.; Mauro, M.; Costa, A.L.; Lead, J.R.; Larese Filon, F. Use of single particle ICP-MS to estimate silver nanoparticle penetration through baby porcine mucosa. *Nanotoxicology* **2021**, *15*, 1005-1015, doi:10.1080/17435390.2021.1940338.

39. Lum, J.T.-S.; Leung, K.S.-Y. Quantifying silver nanoparticle association and elemental content in single cells using dual mass mode in quadrupole-based inductively coupled plasma-mass spectrometry. *Analytica Chimica Acta* **2019**, *1061*, 50-59, doi:https://doi.org/10.1016/j.aca.2019.02.042.
40. Jiménez-Lamana, J.; Wojcieszek, J.; Jakubiak, M.; Asztemborska, M.; Szpunar, J. Single particle ICP-MS characterization of platinum nanoparticles uptake and bioaccumulation by Lepidium sativum and Sinapis alba plants. *Journal of Analytical Atomic Spectrometry* **2016**, *31*, 2321-2329, doi:10.1039/C6JA00201C.
41. Amable, L.; Stephan, C.; Smith, S.; Merrifield, R. An Introduction to Single Cell ICP-MS Analysis. *PerkinElmer Appl Note* **2017**.
42. Chen, Z.; Chen, B.; He, M.; Hu, B. Negative Magnetophoresis Focusing Microchips Online-Coupled with ICP–MS for High-Throughput Single-Cell Analysis. *Analytical Chemistry* **2022**, *94*, 6649-6656, doi:10.1021/acs.analchem.1c04216.
43. Jiao, Y.; Gao, L.; Ji, Y.; Liu, W. Recent advances in microfluidic single-cell analysis and its applications in drug development. *TrAC Trends in Analytical Chemistry* **2022**, *157*, 116796-116796, doi:https://doi.org/10.1016/j.trac.2022.116796.
44. Zhang, X.; Wei, X.; Men, X.; Jiang, Z.; Ye, W.-Q.; Chen, M.-L.; Yang, T.; Xu, Z.-R.; Wang, J.-H. Inertial-Force-Assisted, High-Throughput, Droplet-Free, Single-Cell Sampling Coupled with ICP-MS for Real-Time Cell Analysis. *Analytical Chemistry* **2020**, *92*, 6604-6612, doi:10.1021/acs.analchem.0c00376.
45. Corte-Rodríguez, M.; Álvarez-Fernández, R.; García-Cancela, P.; Montes-Bayón, M.; Bettmer, J. Single cell ICP-MS using on line sample introduction systems: Current developments and remaining challenges. *TrAC Trends in Analytical Chemistry* **2020**, *132*, 116042-116042, doi:https://doi.org/10.1016/j.trac.2020.116042.
46. Chun, K.-H.; Lum, J.T.-S.; Leung, K.S.-Y. Dual-elemental analysis of single particles using quadrupole-based inductively coupled plasma-mass spectrometry. *Analytica Chimica Acta* **2022**, *1192*, 339389-339389, doi:https://doi.org/10.1016/j.aca.2021.339389.
47. McDowell, M.T.; Ryu, I.; Lee, S.W.; Wang, C.; Nix, W.D.; Cui, Y. Studying the kinetics of crystalline silicon nanoparticle lithiation with in situ transmission electron microscopy. *Advanced Materials* **2012**, *24*, 6034-6041, doi:10.1002/adma.201202744.
48. Ding, K.; Liang, S.; Xie, C.; Wan, Q.; Jin, C.; Wang, S.; Tang, Y.-T.; Zhang, M.; Qiu, R. Discrimination and Quantification of Soil Nanoparticles by Dual-Analyte Single Particle ICP–QMS. *Analytical Chemistry* **2022**, *94*, 10745-10753, doi:10.1021/acs.analchem.2c01379.
49. Doble, P.A.; de Vega, R.G.; Bishop, D.P.; Hare, D.J.; Clases, D. Laser Ablation–Inductively Coupled Plasma–Mass Spectrometry Imaging in Biology. *Chemical Reviews* **2021**, *121*, 11769-11822, doi:10.1021/acs.chemrev.0c01219.
50. Theiner, S.; Schweikert, A.; Haberler, C.; Peyrl, A.; Koellensperger, G. Laser ablation-ICP-TOFMS imaging of germ cell tumors of patients undergoing platinum-based chemotherapy†. *Metallomics* **2020**, *12*, 1246-1252, doi:10.1039/d0mt00080a.

51. Sussulini, A.; Becker, J.S.; Becker, J.S. Laser ablation ICP-MS: Application in biomedical research. *Mass Spectrometry Reviews* **2017**, *36*, 47-57, doi:https://doi.org/10.1002/mas.21481.
52. Van Acker, T.; Van Malderen, S.J.M.; Van Heerden, M.; McDuffie, J.E.; Cuyckens, F.; Vanhaecke, F. High-resolution laser ablation-inductively coupled plasma-mass spectrometry imaging of cisplatin-induced nephrotoxic side effects. *Analytica Chimica Acta* **2016**, *945*, 23-30, doi:10.1016/j.aca.2016.10.014.
53. Schoeberl, A.; Gutmann, M.; Theiner, S.; Schaier, M.; Schweikert, A.; Berger, W.; Koellensperger, G. Cisplatin Uptake in Macrophage Subtypes at the Single-Cell Level by LA-ICP-TOFMS Imaging. *Analytical Chemistry* **2021**, *93*, 16456-16465, doi:10.1021/acs.analchem.1c03442.
54. Greenhalgh, C.J.; Karekla, E.; Miles, G.J.; Powley, I.R.; Costa, C.; de Jesus, J.; Bailey, M.J.; Pritchard, C.; MacFarlane, M.; Pringle, J.H., et al. Exploration of Matrix Effects in Laser Ablation Inductively Coupled Plasma Mass Spectrometry Imaging of Cisplatin-Treated Tumors. *Analytical Chemistry* **2020**, *92*, 9847-9855, doi:10.1021/acs.analchem.0c01347.
55. Wang, M.; Zheng, L.; Wang, B.; Yang, P.; Fang, H.; Liang, S.; Chen, W.; Feng, W. Laser ablation-single particle-inductively coupled plasma mass spectrometry as a sensitive tool for bioimaging of silver nanoparticles in vivo degradation. *Chinese Chemical Letters* **2022**, *33*, 3484-3487, doi:https://doi.org/10.1016/j.cclet.2022.03.098.
56. Elci, S.G.; Yan, B.; Kim, S.T.; Saha, K.; Jiang, Y.; Klemmer, G.A.; Moyano, D.F.; Tonga, G.Y.; Rotello, V.M.; Vachet, R.W. Quantitative imaging of 2 nm monolayer-protected gold nanoparticle distributions in tissues using laser ablation inductively-coupled plasma mass spectrometry (LA-ICP-MS). *Analyst* **2016**, *141*, 2418-2425, doi:10.1039/C6AN00123H.
57. Hsiao, I.L.; Bierkandt, F.S.; Reichardt, P.; Luch, A.; Huang, Y.-J.; Jakubowski, N.; Tentschert, J.; Haase, A. Quantification and visualization of cellular uptake of TiO2 and Ag nanoparticles: comparison of different ICP-MS techniques. *Journal of Nanobiotechnology* **2016**, *14*, 50-50, doi:10.1186/s12951-016-0203-z.
58. Zheng, L.N.; Feng, L.X.; Shi, J.W.; Chen, H.Q.; Wang, B.; Wang, M.; Wang, H.F.; Feng, W.Y. Single-Cell Isotope Dilution Analysis with LA-ICP-MS: A New Approach for Quantification of Nanoparticles in Single Cells. *Analytical Chemistry* **2020**, *92*, 14339-14345, doi:10.1021/acs.analchem.0c01775.
59. Zheng, L.-N.; Sang, Y.-B.; Luo, R.-P.; Wang, B.; Yi, F.-T.; Wang, M.; Feng, W.-Y. Determination of silver nanoparticles in single cells by microwell trapping and laser ablation ICP-MS determination. *Journal of Analytical Atomic Spectrometry* **2019**, *34*, 915-921, doi:10.1039/C8JA00438B.
60. Löhr, K.; Borovinskaya, O.; Tourniaire, G.; Panne, U.; Jakubowski, N. Arraying of Single Cells for Quantitative High Throughput Laser Ablation ICP-TOF-MS. *Analytical Chemistry* **2019**, *91*, 11520-11528, doi:10.1021/acs.analchem.9b00198.
61. Hendriks, L.; Gundlach-Graham, A.; Hattendorf, B.; Günther, D. Characterization of a new ICP-TOFMS instrument with continuous and discrete introduction of solutions. *Journal of Analytical Atomic Spectrometry* **2017**, *32*, 548-561, doi:10.1039/C6JA00400H.

62. Harycki, S.; Gundlach-Graham, A. Characterization of a high-sensitivity ICP-TOFMS instrument for microdroplet, nanoparticle, and microplastic analyses. *Journal of Analytical Atomic Spectrometry* **2023**, *38*, 111-120, doi:10.1039/D2JA00295G.
63. Salt, D.E.; Baxter, I.; Lahner, B. Ionomics and the Study of the Plant Ionome. *Annual Review of Plant Biology* **2008**, *59*, 709-733, doi:10.1146/annurev.arplant.59.032607.092942.
64. Malinouski, M.; Hasan, N.M.; Zhang, Y.; Seravalli, J.; Lin, J.; Avanesov, A.; Lutsenko, S.; Gladyshev, V.N. Genome-wide RNAi ionomics screen reveals new genes and regulation of human trace element metabolism. *Nature Communications* **2014**, *5*, 3301-3301, doi:10.1038/ncomms4301.
65. von der Au, M.; Borovinskaya, O.; Flamigni, L.; Kuhlmeier, K.; Büchel, C.; Meermann, B. Single cell-inductively coupled plasma-time of flight-mass spectrometry approach for ecotoxicological testing. *Algal Research* **2020**, *49*, 101964-101964, doi:https://doi.org/10.1016/j.algal.2020.101964.
66. Chronakis, M.I.; von der Au, M.; Meermann, B. Single cell-asymmetrical flow field-flow fractionation/ICP-time of flight-mass spectrometry (sc-AF4/ICP-ToF-MS): an efficient alternative for the cleaning and multielemental analysis of individual cells. *Journal of Analytical Atomic Spectrometry* **2022**, *37*, 2691-2700, doi:10.1039/D2JA00264G.
67. Hendriks, L.; Michael Skjolding, L.; Thomas, R. Single-Cell Analysis by Inductively Coupled Plasma–Time-of-Flight Mass Spectrometry to Quantify Algal Cell Interaction with Nanoparticles by Their Elemental Fingerprint. *Spectroscopy* **2020**, *35*, 9-16.
68. Lum, T.-S.; Sze-Yin Leung, K. Strategies to overcome spectral interference in ICP-MS detection. *Journal of Analytical Atomic Spectrometry* **2016**, *31*, 1078-1088, doi:10.1039/C5JA00497G.
69. Tan, S.H.; Horlick, G. Matrix-effect observations in inductively coupled plasma mass spectrometry. *Journal of Analytical Atomic Spectrometry* **1987**, *2*, 745-763, doi:10.1039/JA9870200745.
70. Hendriks, L.; Ramkorun-Schmidt, B.; Gundlach-Graham, A.; Koch, J.; Grass, R.N.; Jakubowski, N.; Günther, D. Single-particle ICP-MS with online microdroplet calibration: toward matrix independent nanoparticle sizing. *Journal of Analytical Atomic Spectrometry* **2019**, *34*, 716-728, doi:10.1039/C8JA00397A.
71. Mehrabi, K.; Günther, D.; Gundlach-Graham, A. Single-particle ICP-TOFMS with online microdroplet calibration for the simultaneous quantification of diverse nanoparticles in complex matrices. *Environmental Science: Nano* **2019**, *6*, 3349-3358, doi:10.1039/C9EN00620F.
72. Harycki, S.; Gundlach-Graham, A. Online microdroplet calibration for accurate nanoparticle quantification in organic matrices. *Analytical and Bioanalytical Chemistry* **2022**, *414*, 7543-7551, doi:10.1007/s00216-022-04115-2.
73. López-Serrano Oliver, A.; Haase, A.; Peddinghaus, A.; Wittke, D.; Jakubowski, N.; Luch, A.; Grützkau, A.; Baumgart, S. Mass Cytometry Enabling Absolute and Fast Quantification of Silver Nanoparticle Uptake at the Single Cell Level. *Analytical Chemistry* **2019**, *91*, 11514-11519, doi:10.1021/acs.analchem.9b01870.

74. Ivask, A.; Mitchell, A.J.; Hope, C.M.; Barry, S.C.; Lombi, E.; Voelcker, N.H. Single Cell Level Quantification of Nanoparticle–Cell Interactions Using Mass Cytometry. *Analytical Chemistry* **2017**, *89*, 8228-8232, doi:10.1021/acs.analchem.7b01006.
75. Malysheva, A.; Ivask, A.; Doolette, C.L.; Voelcker, N.H.; Lombi, E. Cellular binding, uptake and biotransformation of silver nanoparticles in human T lymphocytes. *Nature Nanotechnology* **2021**, *16*, 926-932, doi:10.1038/s41565-021-00914-3.
76. Yang, Y.S.S.; Atukorale, P.U.; Moynihan, K.D.; Bekdemir, A.; Rakhra, K.; Tang, L.; Stellacci, F.; Irvine, D.J. High-throughput quantitation of inorganic nanoparticle biodistribution at the single-cell level using mass cytometry. *Nature Communications* **2017**, *8*, doi:10.1038/ncomms14069.
77. Spitzer, M.H.; Nolan, G.P. Mass Cytometry: Single Cells, Many Features. In *Cell*, Cell Press: 2016; Vol. 165, pp 780-791.
78. Arnett, L.P.; Rana, R.; Chung, W.W.-Y.; Li, X.; Abtahi, M.; Majonis, D.; Bassan, J.; Nitz, M.; Winnik, M.A. Reagents for Mass Cytometry. *Chemical Reviews* **2023**, 10.1021/acs.chemrev.2c00350, doi:10.1021/acs.chemrev.2c00350.
79. Drescher, H.; Weiskirchen, S.; Weiskirchen, R. Flow cytometry: A blessing and a curse. *Biomedicines* **2021**, *9*, doi:10.3390/biomedicines9111613.
80. Tanner, S.D.; Baranov, V.I.; Ornatsky, O.I.; Bandura, D.R.; George, T.C. An introduction to mass cytometry: Fundamentals and applications. In *Cancer Immunology, Immunotherapy*, 2013; Vol. 62, pp 955-965.
81. Manohar, S.M.; Shah, P.; Nair, A. Flow cytometry: Principles, applications and recent advances. In *Bioanalysis*, Future Medicine Ltd.: 2021; Vol. 13, pp 185-202.
82. Bendall, S.C.; Simonds, E.F.; Qiu, P.; Amir, E.A.D.; Krutzik, P.O.; Finck, R.; Bruggner, R.V.; Melamed, R.; Trejo, A.; Ornatsky, O.I., et al. Single-cell mass cytometry of differential immune and drug responses across a human hematopoietic continuum. *Science* **2011**, *332*, 687-696, doi:10.1126/science.1198704.
83. Sahaf, B.; Rahman, A.; Maecker, H.T.; Bendall, S.C. High-Parameter Immune Profiling with CyTOF. In *Biomarkers for Immunotherapy of Cancer: Methods and Protocols*, Thurin, M., Cesano, A., Marincola, F.M., Eds. Springer New York: New York, NY, 2020; 10.1007/978-1-4939-9773-2_16pp. 351-368.
84. Gadalla, R.; Noamani, B.; MacLeod, B.L.; Dickson, R.J.; Guo, M.; Xu, W.; Lukhele, S.; Elsaesser, H.J.; Razak, A.R.A.; Hirano, N., et al. Validation of CyTOF Against Flow Cytometry for Immunological Studies and Monitoring of Human Cancer Clinical Trials. *Frontiers in Oncology* **2019**, *9*, doi:10.3389/fonc.2019.00415.
85. Tian, X.; Jiang, H.; Wang, M.; Cui, W.; Guo, Y.; Zheng, L.; Hu, L.; Qu, G.; Yin, Y.; Cai, Y., et al. Exploring the performance of quadrupole, time-of-flight, and multi-collector ICP-MS for dual-isotope detection on single nanoparticles and cells. *Analytica Chimica Acta* **2023**, *1240*, 340756-340756, doi:https://doi.org/10.1016/j.aca.2022.340756.
86. Nassar, A.F.; Ogura, H.; Wisnewski, A.V. Impact of recent innovations in the use of mass cytometry in support of drug development. *Drug Discovery Today* **2015**, *20*, 1169-1175, doi:https://doi.org/10.1016/j.drudis.2015.06.001.
87. Bandura, D.R.; Baranov, V.I.; Ornatsky, O.I.; Antonov, A.; Kinach, R.; Lou, X.; Pavlov, S.; Vorobiev, S.; Dick, J.E.; Tanner, S.D. Mass Cytometry: Technique for Real Time Single Cell Multitarget Immunoassay Based on Inductively Coupled

Plasma Time-of-Flight Mass Spectrometry. *Analytical Chemistry* **2009**, *81*, 6813-6822, doi:10.1021/ac901049w.
88. Zhu, Y.P.; Eggert, T.; Araujo, D.J.; Vijayanand, P.; Ottensmeier, C.H.; Hedrick, C.C. CyTOF mass cytometry reveals phenotypically distinct human blood neutrophil populations differentially correlated with melanoma stage. *Journal for ImmunoTherapy of Cancer* **2020**, *8*, e000473-e000473, doi:10.1136/jitc-2019-000473.
89. Ha, M.K.; Kwon, S.J.; Choi, J.-S.; Nguyen, N.T.; Song, J.; Lee, Y.; Kim, Y.-E.; Shin, I.; Nam, J.-W.; Yoon, T.H. Mass Cytometry and Single-Cell RNA-seq Profiling of the Heterogeneity in Human Peripheral Blood Mononuclear Cells Interacting with Silver Nanoparticles. *Small* **2020**, *16*, 1907674-1907674, doi:https://doi.org/10.1002/smll.201907674.
90. Schulz, A.R.; Stanislawiak, S.; Baumgart, S.; Grützkau, A.; Mei, H.E. Silver nanoparticles for the detection of cell surface antigens in mass cytometry. *Cytometry Part A* **2017**, *91*, 25-33, doi:https://doi.org/10.1002/cyto.a.22904.
91. Pichaandi, J.; Tong, L.; Bouzekri, A.; Yu, Q.; Ornatsky, O.; Baranov, V.; Winnik, M.A. Liposome-Encapsulated NaLnF4 Nanoparticles for Mass Cytometry: Evaluating Nonspecific Binding to Cells. *Chemistry of Materials* **2017**, *29*, 4980-4990, doi:10.1021/acs.chemmater.7b01339.
92. Chang, Q.; Ornatsky, O.I.; Siddiqui, I.; Loboda, A.; Baranov, V.I.; Hedley, D.W. Imaging Mass Cytometry. In *Cytometry Part A*, Wiley-Liss Inc.: 2017; Vol. 91, pp 160-169.
93. Ali, H.R.; Jackson, H.W.; Zanotelli, V.R.T.; Danenberg, E.; Fischer, J.R.; Bardwell, H.; Provenzano, E.; Rueda, O.M.; Chin, S.F.; Aparicio, S., et al. Imaging mass cytometry and multiplatform genomics define the phenogenomic landscape of breast cancer. *Nature cancer* **2020**, *1*, 163-175, doi:10.1038/s43018-020-0026-6.
94. Malile, B.; Brkic, J.; Bouzekri, A.; Wilson, D.J.; Ornatsky, O.; Peng, C.; Chen, J.I.L. DNA-Conjugated Gold Nanoparticles as High-Mass Probes in Imaging Mass Cytometry. *ACS Applied Bio Materials* **2019**, *2*, 4316-4323, doi:10.1021/acsabm.9b00574.
95. Donahue, N.D.; Acar, H.; Wilhelm, S. Concepts of nanoparticle cellular uptake, intracellular trafficking, and kinetics in nanomedicine. *Adv. Drug Delivery Rev.* **2019**, *143*, 68-96, doi:https://doi.org/10.1016/j.addr.2019.04.008.
96. Villanueva-Flores, F.; Castro-Lugo A Fau - Ramírez, O.T.; Ramírez Ot Fau - Palomares, L.A.; Palomares, L.A. Understanding cellular interactions with nanomaterials: towards a rational design of medical nanodevices. *Nanotechnology* **2020**, *31*, doi:https://doi.org/10.1088/1361-6528/ab5bc8.
97. Hoshyar, N.; Gray, S.; Han, H.; Bao, G. The effect of nanoparticle size on in vivo pharmacokinetics and cellular interaction. *Nanomedicine* **2016**, *11 (6)*, doi:https://doi.org/10.2217/nnm.16.5.
98. Thomas, O.S.; Weber, W. Overcoming physiological barriers to nanoparticle delivery—are we there yet? *Front. Bioeng. Biotechnol.* **2019**, *7*, 415, doi:https://doi.org/10.3389/fbioe.2019.00415.
99. Chen, K.-H.; Lundy, D.; Toh, E.-W.; Chen, C.-H.; Shih, C.; Chen, P.; Chang, H.-C.; Lai, J.; Stayton, P.; Hoffman, A. Nanoparticle distribution during systemic

inflammation is size-dependent and organ-specific. *Nanoscale* **2015**, *7*, 15863-15872, doi:https://doi.org/10.1039/C5NR03626G.
100. Muzzio, M.; Li, J.; Yin, Z.; Delahunty, I.M.; Xie, J.; Sun, S. Monodisperse nanoparticles for catalysis and nanomedicine. *Nanoscale* **2019**, *11*, 18946-18967, doi:https://doi.org/10.1039/C9NR06080D.
101. Dheyab, M.A.; Aziz, A.A.; Moradi Khaniabadi, P.; Jameel, M.S.; Oladzadabbasabadi, N.; Mohammed, S.A.; Abdullah, R.S.; Mehrdel, B. Monodisperse Gold Nanoparticles: A Review on Synthesis and Their Application in Modern Medicine. *Int. J. Mol. Sci.* **2022**, *23*, 7400, doi:https://doi.org/10.3390/ijms23137400.
102. Kus-Liśkiewicz, M.A.-O.; Fickers, P.A.-O.; Ben Tahar, I. Biocompatibility and Cytotoxicity of Gold Nanoparticles: Recent Advances in Methodologies and Regulations. *Int. J. Mol. Sci.* **2021**, *22 (20)*, doi:https://doi.org/10.3390/ijms222010952.
103. Turnbull, T.; Thierry, B.; Kempson, I. A quantitative study of intercellular heterogeneity in gold nanoparticle uptake across multiple cell lines. *Anal. Bioanal. Chem.* **2019**, *411*, 7529-7538, doi:https://doi.org/10.1007/s00216-019-02154-w.
104. Carabineiro, S.A.C. Applications of Gold Nanoparticles in Nanomedicine: Recent Advances in Vaccines. *Molecules* **2017**, *22 (5)*, doi:https://doi.org/10.3390/molecules22050857.
105. Elumalai, M.; Ipatov, A.; Carvalho, J.; Guerreiro, J.; Prado, M. Dual colorimetric strategy for specific DNA detection by nicking endonuclease-assisted gold nanoparticle signal amplification. *Anal. Bioanal. Chem.* **2022**, *414*, 5239-5253, doi:https://doi.org/10.1007/s00216-021-03564-5.
106. Sánchez-Visedo, A.; Ferrero, F.J.; Costa-Fernández, J.M.; Fernández-Argüelles, M.T. Inorganic nanoparticles coupled to nucleic acid enzymes as analytical signal amplification tools. *Anal. Bioanal. Chem.* **2022**, *414*, 5201-5215, doi:https://doi.org/10.1007/s00216-022-03998-5.
107. Modena, M.M.; Rühle, B.; Burg, T.P.; Wuttke, S. Nanoparticle Characterization: What to Measure? *Adv. Mater.* **2019**, *31*, 1901556, doi:https://doi.org/10.1002/adma.201901556.
108. Hoo, C.M.; Starostin, N.; West, P.; Mecartney, M.L. A comparison of atomic force microscopy (AFM) and dynamic light scattering (DLS) methods to characterize nanoparticle size distributions. *J. Nanopart. Res.* **2008**, *10*, 89-96, doi:https://doi.org/10.1007/s11051-008-9435-7.
109. Dastanpour, R.; Boone, J.M.; Rogak, S.N. Automated primary particle sizing of nanoparticle aggregates by TEM image analysis. *Powder Technology* **2016**, *295*, 218-224, doi:https://doi.org/10.1016/j.powtec.2016.03.027.
110. Mozhayeva, D.; Engelhard, C. A critical review of single particle inductively coupled plasma mass spectrometry – A step towards an ideal method for nanomaterial characterization. *J. Anal. At. Spectrom.* **2020**, *35*, 1740-1783, doi:https://doi.org/10.1039/C9JA00206E.
111. Montaño, M.D.; Lowry, G.V.; von der Kammer, F.; Blue, J.; Ranville, J.F. Current status and future direction for examining engineered nanoparticles in natural systems. *Environ. Chem.* **2014**, *11*, 351-366, doi:https://doi.org/10.1071/EN14037.

112. Bocca, B.; Battistini, B.; Petrucci, F. Silver and gold nanoparticles characterization by SP-ICP-MS and AF4-FFF-MALS-UV-ICP-MS in human samples used for biomonitoring. *Talanta* **2020**, *220*, 121404, doi:https://doi.org/10.1016/j.talanta.2020.121404.
113. Xing, Y.; Han, J.; Wu, X.; Pierce, D.T.; Zhao, J.X. Aggregation-based determination of mercury(II) using DNA-modified single gold nanoparticle, T-Hg(II)-T interaction, and single-particle ICP-MS. *Microchim. Acta* **2019**, *187*, 56, doi:https://doi.org/10.1007/s00604-019-4057-6.
114. Xu, X.; Chen, J.; Li, B.; Tang, L.; Jiang, J. Single particle ICP-MS-based absolute and relative quantification of E. coli O157 16S rRNA using sandwich hybridization capture. *Analyst* **2019**, *144*, 1725-1730, doi:https://doi.org/10.1039/C8AN02063A.
115. Hu, J.; Deng, D.; Liu, R.; Lv, Y. Single nanoparticle analysis by ICPMS: a potential tool for bioassay. *J. Anal. At. Spectrom.* **2018**, *33*, 57-67, doi:https://doi.org/10.1039/C7JA00235A.
116. Donahue, N.D.; Kanapilly, S.; Stephan, C.; Marlin, M.C.; Francek, E.R.; Haddad, M.; Guthridge, J.; Wilhelm, S. Quantifying Chemical Composition and Reaction Kinetics of Individual Colloidally Dispersed Nanoparticles. *Nano Letters* **2022**, *22*, 294-301, doi:10.1021/acs.nanolett.1c03752.
117. Donahue, N.D.; Francek, E.R.; Kiyotake, E.; Thomas, E.E.; Yang, W.; Wang, L.; Detamore, M.S.; Wilhelm, S. Assessing nanoparticle colloidal stability with single-particle inductively coupled plasma mass spectrometry (SP-ICP-MS). *Anal. Bioanal. Chem.* **2020**, *412*, 5205-5216, doi:https://doi.org/10.1007/s00216-020-02783-6.
118. Perrault, S.D.; Chan, W.C.W. Synthesis and Surface Modification of Highly Monodispersed, Spherical Gold Nanoparticles of 50−200 nm. *J. Am. Chem. Soc.* **2009**, *131*, 17042-17043, doi:https://doi.org/10.1021/ja907069u.
119. Zheng, Y.; Zhong, X.; Li, Z.; Xia, Y. Successive, Seed-Mediated Growth for the Synthesis of Single-Crystal Gold Nanospheres with Uniform Diameters Controlled in the Range of 5–150 nm. *Part. Part. Syst. Charact.* **2014**, *31*, 266-273, doi:https://doi.org/10.1002/ppsc.201300256.
120. Liu, N.; Zhang, H.; Zhao, J.; Xu, Y.; Ge, F. Mechanisms of cetyltrimethyl ammonium chloride-induced toxicity to photosystem II oxygen evolution complex of Chlorella vulgaris F1068. *J. Hazard. Mater.* **2020**, *383*, 121063, doi:https://doi.org/10.1016/j.jhazmat.2019.121063.
121. Tang, M.; Zhang, P.; Liu, J.; Long, Y.; Cheng, Y.; Zheng, H. Cetyltrimethylammonium chloride-loaded mesoporous silica nanoparticles as a mitochondrion-targeting agent for tumor therapy. *RSC Adv.* **2020**, *10*, 17050-17057, doi:https://doi.org/10.1039/D0RA02023.
122. Turkevich, J.; Stevenson, P.C.; Hillier, J. A study of the nucleation and growth processes in the synthesis of colloidal gold. *Discuss. Faraday Soc.* **1951**, *11*, 55-75, doi:https://doi.org/10.1039/DF9511100055.
123. Schulz, F.; Pavelka, O.; Lehmkühler, F.; Westermeier, F.; Okamura, Y.; Mueller, N.S.; Reich, S.; Lange, H. Structural order in plasmonic superlattices. *Nat. Commun.* **2020**, *11*, 3821, doi:https://doi.org/10.1038/s41467-020-17632-4.
124. Zheng, Y.; Ma, Y.; Zeng, J.; Zhong, X.; Jin, M.; Li, Z.-Y.; Xia, Y. Seed-Mediated Synthesis of Single-Crystal Gold Nanospheres with Controlled Diameters in the

Range 5–30 nm and their Self-Assembly upon Dilution. *Chem. - Asian J.* **2013**, *8*, 792-799, doi:https://doi.org/10.1002/asia.201201105.
125. Pace, H.E.; Rogers, N.J.; Jarolimek, C.; Coleman, V.A.; Higgins, C.P.; Ranville, J.F. Determining Transport Efficiency for the Purpose of Counting and Sizing Nanoparticles via Single Particle Inductively Coupled Plasma Mass Spectrometry. *Anal. Chem.* **2011**, *83*, 9361-9369, doi:https://doi.org/10.1021/ac201952t.
126. Pace, H.E.; Rogers, N.J.; Jarolimek, C.; Coleman, V.A.; Gray, E.P.; Higgins, C.P.; Ranville, J.F. Single Particle Inductively Coupled Plasma-Mass Spectrometry: A Performance Evaluation and Method Comparison in the Determination of Nanoparticle Size. *Environ. Sci. Technol.* **2012**, *46*, 12272-12280, doi:https://doi.org/10.1021/es301787d.
127. Laborda, F.; Bolea, E.; Jiménez-Lamana, J. Single Particle Inductively Coupled Plasma Mass Spectrometry: A Powerful Tool for Nanoanalysis. *Anal. Chem.* **2014**, *86*, 2270-2278, doi:https://doi.org/10.1021/ac402980q.
128. Lee, J.C.; Donahue, N.D.; Mao, A.S.; Karim, A.; Komarneni, M.; Thomas, E.E.; Francek, E.R.; Yang, W.; Wilhelm, S. Exploring Maleimide-Based Nanoparticle Surface Engineering to Control Cellular Interactions. *ACS Applied Nano Materials* **2020**, *3*, 2421-2429, doi:10.1021/acsanm.9b02541.
129. Li, J.; Zhu, B.; Zhu, Z.; Zhang, Y.; Yao, X.; Tu, S.; Liu, R.; Jia, S.; Yang, C.J. Simple and Rapid Functionalization of Gold Nanorods with Oligonucleotides Using an mPEG-SH/Tween 20-Assisted Approach. *Langmuir* **2015**, *31*, 7869-7876, doi:https://doi.org/10.1021/acs.langmuir.5b01680.
130. Slesiona, N.; Thamm, S.; Stolle, H.L.K.S.; Weißenborn, V.; Müller, P.; Csáki, A.; Fritzsche, W. DNA-Biofunctionalization of CTAC-Capped Gold Nanocubes. *Nanomaterials* **2020**, *10*, 1119, doi:https://doi.org/10.3390/nano10061119.
131. Lee, C.-Y.; Nguyen, P.-C.T.; Grainger, D.W.; Gamble, L.J.; Castner, D.G. Structure and DNA Hybridization Properties of Mixed Nucleic Acid/Maleimide−Ethylene Glycol Monolayers. *Anal. Chem.* **2007**, *79*, 4390-4400, doi:https://doi.org/10.1021/ac0703395.
132. Chou, L.Y.T.; Zagorovsky, K.; Chan, W.C.W. DNA assembly of nanoparticle superstructures for controlled biological delivery and elimination. *Nat. Nanotechnol.* **2014**, *9*, 148-155, doi:https://doi.org/10.1038/nnano.2013.309.
133. Zagorovsky, K.; Chou, L.Y.T.; Chan, W.C.W. Controlling DNA–nanoparticle serum interactions. *Proc. Natl. Acad. Sci.* **2016**, *113*, 13600-13605, doi:https://doi.org/10.1073/pnas.1610028113.
134. Maguire, C.A.-O.; Rösslein, M.; Wick, P.; Prina-Mello, A.A.-O. Characterisation of particles in solution - a perspective on light scattering and comparative technologies. *Sci. Technol. Adv. Mater.* **2018**, *19 (1)*, 732-745, doi:https://doi.org/10.1080/14686996.2018.1517587.
135. Khlebtsov, N.G. Determination of Size and Concentration of Gold Nanoparticles from Extinction Spectra. *Anal. Chem.* **2008**, *80*, 6620-6625, doi:https://doi.org/10.1021/ac800834n.
136. Shafiqa, A.R.; Abdul Aziz, A.; Mehrdel, B. Nanoparticle Optical Properties: Size Dependence of a Single Gold Spherical Nanoparticle. *J. Phys.: Conf. Ser.* **2018**, *1083*, 012040, doi:https://doi.org/10.1088/1742-6596/1083/1/012040.

137. Huang, Y.; Kim, D.-H. Synthesis and Self-Assembly of Highly Monodispersed Quasispherical Gold Nanoparticles. *Langmuir* **2011**, *27*, 13861-13867, doi:https://doi.org/10.1021/la203143k.
138. Lee, S.; Bi, X.; Reed, R.B.; Ranville, J.F.; Herckes, P.; Westerhoff, P. Nanoparticle Size Detection Limits by Single Particle ICP-MS for 40 Elements. *Environ. Sci. Technol.* **2014**, *48*, 10291-10300, doi:https://doi.org/10.1021/es502422v.
139. Suk, J.S.; Xu, Q.; Kim, N.; Hanes, J.; Ensign, L.M. PEGylation as a strategy for improving nanoparticle-based drug and gene delivery. *Adv. Drug Delivery Rev.* **2016**, *99 (A)*, 28-51, doi:https://doi.org/10.1016/j.addr.2015.09.012.
140. Jokerst, J.V.; Lobovkina T Fau - Zare, R.N.; Zare Rn Fau - Gambhir, S.S.; Gambhir, S.S. Nanoparticle PEGylation for imaging and therapy. *Nanomedicine* **2011**, *6 (4)*, doi:https://doi.org/10.2217/nnm.11.19.
141. Kokkin, D.L.; Zhang, R.; Steimle, T.C.; Wyse, I.A.; Pearlman, B.W.; Varberg, T.D. Au–S Bonding Revealed from the Characterization of Diatomic Gold Sulfide, AuS. *J. Phys. Chem. A* **2015**, *119*, 11659-11667, doi:https://doi.org/10.1021/acs.jpca.5b08781.
142. Bürgi, T. Properties of the gold–sulphur interface: from self-assembled monolayers to clusters. *Nanoscale* **2015**, *7*, 15553-15567, doi:https://doi.org/10.1039/C5NR03497C.
143. Dai, Q.; Wilhelm, S.; Ding, D.; Syed, A.M.; Sindhwani, S.; Zhang, Y.; Chen, Y.Y.; MacMillan, P.; Chan, W.C.W. Quantifying the Ligand-Coated Nanoparticle Delivery to Cancer Cells in Solid Tumors. *ACS Nano* **2018**, *12*, 8423-8435, doi:https://doi.org/10.1021/acsnano.8b03900.
144. Syed, A.M.; Sindhwani, S.; Wilhelm, S.; Kingston, B.R.; Lee, D.S.W.; Gommerman, J.L.; Chan, W.C.W. Three-Dimensional Imaging of Transparent Tissues via Metal Nanoparticle Labeling. *J. Am. Chem. Soc.* **2017**, *139*, 9961-9971, doi:https://doi.org/10.1021/jacs.7b04022.
145. Wang, F.; Chen, B.; Yan, B.; Yin, Y.; Hu, L.; Liang, Y.; Song, M.; Jiang, G. Scattered Light Imaging Enables Real-Time Monitoring of Label-Free Nanoparticles and Fluorescent Biomolecules in Live Cells. **2019**, 10.1021/jacs.9b05894, doi:10.1021/jacs.9b05894.
146. Arnida; Janát-Amsbury, M.M.; Ray, A.; Peterson, C.M.; Ghandehari, H. Geometry and surface characteristics of gold nanoparticles influence their biodistribution and uptake by macrophages. *European Journal of Pharmaceutics and Biopharmaceutics* **2011**, *77*, 417-423, doi:10.1016/j.ejpb.2010.11.010.
147. Bai, X.; Wang, Y.; Song, Z.; Feng, Y.; Chen, Y.; Zhang, D.; Feng, L. The basic properties of gold nanoparticles and their applications in tumor diagnosis and treatment. In *International Journal of Molecular Sciences*, MDPI AG: 2020; Vol. 21.
148. Yeh, Y.-C.; Creran, B.; Rotello, V.M. Gold nanoparticles: preparation, properties, and applications in bionanotechnology. *Nanoscale* **2012**, *4*, 1871-1880, doi:10.1039/C1NR11188D.
149. Herizchi, R.; Abbasi, E.; Milani, M.; Akbarzadeh, A. Current methods for synthesis of gold nanoparticles. *Artificial Cells, Nanomedicine, and Biotechnology* **2016**, *44*, 596-602, doi:10.3109/21691401.2014.971807.
150. Kang, M.S.; Lee, S.Y.; Kim, K.S.; Han, D.-W. State of the Art Biocompatible Gold Nanoparticles for Cancer Theragnosis. In *Pharmaceutics*, 2020; Vol. 12.

151. Kumar, V.; Sharma, N.; Maitra, S.S. In vitro and in vivo toxicity assessment of nanoparticles. *International Nano Letters* **2017**, *7*, 243-256, doi:10.1007/s40089-017-0221-3.
152. Balog, S. Hydrodynamic Radius of Polymer-Coated Nanoparticles Measured by Taylor Dispersion: A Mathematical Model. *Analytical Chemistry* **2020**, *92*, 10693-10699, doi:10.1021/acs.analchem.0c01837.
153. Stetefeld, J.; McKenna, S.A.; Patel, T.R. Dynamic light scattering: a practical guide and applications in biomedical sciences. *Biophysical Reviews* **2016**, *8*, 409-427, doi:10.1007/s12551-016-0218-6.
154. Giorgi, F.; Curran, J.M.; Gilliland, D.; La Spina, R.; Whelan, M.; Patterson, E.A. Limitations of Nanoparticles Size Characterization by Asymmetric Flow Field-Fractionation Coupled with Online Dynamic Light Scattering. *Chromatographia* **2021**, *84*, 199-206, doi:10.1007/s10337-020-03997-7.
155. Chauhan, M.K.; Sachdeva, A.; Ansari, L.; Gugulothu, D. Manufacturing Process of Nanoparticles. In *Pharmaceutical Process Engineering and Scale-up Principles*, Jindal, A.B., Ed. Springer Nature Switzerland: Cham, 2023; 10.1007/978-3-031-31380-6_11pp. 151-172.
156. Yoon, S.; Kim, C.; Lee, B.; Lee, J.H. From a precursor to an etchant: spontaneous inversion of the role of Au(iii) chloride for one-pot synthesis of smooth and spherical gold nanoparticles. *Nanoscale Advances* **2019**, *1*, 2157-2161, doi:10.1039/C9NA00157C.
157. Anik, M.I.; Mahmud, N.; Al Masud, A.; Hasan, M. Gold nanoparticles (GNPs) in biomedical and clinical applications: A review. *Nano Select* **2022**, *3*, 792-828, doi:https://doi.org/10.1002/nano.202100255.
158. Li, X.; Wang, L.; Fan, Y.; Feng, Q.; Cui, F.-z. Biocompatibility and Toxicity of Nanoparticles and Nanotubes. *Journal of Nanomaterials* **2012**, *2012*, 548389, doi:10.1155/2012/548389.
159. Zhang, Y.; Elechalawar, C.K.; Yang, W.; Frickenstein, A.N.; Asfa, S.; Fung, K.-M.; Murphy, B.N.; Dwivedi, S.K.; Rao, G.; Dey, A., et al. Disabling partners in crime: Gold nanoparticles disrupt multicellular communications within the tumor microenvironment to inhibit ovarian tumor aggressiveness. *Materials Today* **2022**, *56*, 79-95, doi:https://doi.org/10.1016/j.mattod.2022.01.025.
160. Elechalawar, C.K.; Rao, G.; Gulla, S.K.; Patel, M.M.; Frickenstein, A.; Means, N.; Roy, R.V.; Tsiokas, L.; Asfa, S.; Panja, P., et al. Gold Nanoparticles Inhibit Macropinocytosis by Decreasing KRAS Activation. *ACS Nano* **2023**, *17*, 9326-9337, doi:10.1021/acsnano.3c00920.
161. Xu, M.; Soliman, M.G.; Sun, X.; Pelaz, B.; Feliu, N.; Parak, W.J.; Liu, S. How Entanglement of Different Physicochemical Properties Complicates the Prediction of in Vitro and in Vivo Interactions of Gold Nanoparticles. *ACS Nano* **2018**, *12*, 10104-10113, doi:10.1021/acsnano.8b04906.
162. Chen, B.-M.; Cheng, T.-L.; Roffler, S.R. Polyethylene Glycol Immunogenicity: Theoretical, Clinical, and Practical Aspects of Anti-Polyethylene Glycol Antibodies. *ACS Nano* **2021**, *15*, 14022-14048, doi:10.1021/acsnano.1c05922.
163. Ju, Y.; Lee, W.S.; Pilkington, E.H.; Kelly, H.G.; Li, S.; Selva, K.J.; Wragg, K.M.; Subbarao, K.; Nguyen, T.H.O.; Rowntree, L.C., et al. Anti-PEG Antibodies Boosted

in Humans by SARS-CoV-2 Lipid Nanoparticle mRNA Vaccine. *ACS Nano* **2022**, *16*, 11769-11780, doi:10.1021/acsnano.2c04543.
164. Kiyotake, E.A.; Thomas, E.E.; Homburg, H.B.; Milton, C.K.; Smitherman, A.D.; Donahue, N.D.; Fung, K.-M.; Wilhelm, S.; Martin, M.D.; Detamore, M.S. Conductive and injectable hyaluronic acid/gelatin/gold nanorod hydrogels for enhanced surgical translation and bioprinting. *Journal of Biomedical Materials Research Part A* **2022**, *110*, 365-382, doi:https://doi.org/10.1002/jbm.a.37294.
165. Zhou, S.; Huo, D.; Goines, S.; Yang, T.-H.; Lyu, Z.; Zhao, M.; Gilroy, K.D.; Wu, Y.; Hood, Z.D.; Xie, M., et al. Enabling Complete Ligand Exchange on the Surface of Gold Nanocrystals through the Deposition and Then Etching of Silver. *Journal of the American Chemical Society* **2018**, *140*, 11898-11901, doi:10.1021/jacs.8b06464.
166. Mehtala, J.G.; Zemlyanov, D.Y.; Max, J.P.; Kadasala, N.; Zhao, S.; Wei, A. Citrate-Stabilized Gold Nanorods. *Langmuir* **2014**, *30*, 13727-13730, doi:10.1021/la5029542.
167. Byzova, N.A.; Zherdev, A.V.; Khlebtsov, B.N.; Burov, A.M.; Khlebtsov, N.G.; Dzantiev, B.B. Advantages of Highly Spherical Gold Nanoparticles as Labels for Lateral Flow Immunoassay. In *Sensors*, 2020; Vol. 20.
168. Anastassopoulou, J.D. Mass and FT-IR Spectra of Quaternary Ammonium Surfactants. In *Chemistry and Properties of Biomolecular Systems*, Rizzarelli, E., Theophanides, T., Eds. Springer Netherlands: Dordrecht, 1991; 10.1007/978-94-011-3620-4_1pp. 1-9.
169. Gurunathan, S.; Han, J.; Park, J.H.; Kim, J.-H. A green chemistry approach for synthesizing biocompatible gold nanoparticles. *Nanoscale Research Letters* **2014**, *9*, 248, doi:10.1186/1556-276X-9-248.
170. Kurrey, R.; Deb, M.K.; Shrivas, K.; Khalkho, B.R.; Nirmalkar, J.; Sinha, D.; Jha, S. Citrate-capped gold nanoparticles as a sensing probe for determination of cetyltrimethylammonium surfactant using FTIR spectroscopy and colorimetry. *Analytical and Bioanalytical Chemistry* **2019**, *411*, 6943-6957, doi:10.1007/s00216-019-02067-8.
171. Villarreal, E.; Li, G.G.; Zhang, Q.; Fu, X.; Wang, H. Nanoscale Surface Curvature Effects on Ligand–Nanoparticle Interactions: A Plasmon-Enhanced Spectroscopic Study of Thiolated Ligand Adsorption, Desorption, and Exchange on Gold Nanoparticles. *Nano Letters* **2017**, *17*, 4443-4452, doi:10.1021/acs.nanolett.7b01593.
172. Deangelis, P.L. Expert Opinion on Drug Delivery Heparosan, a promising 'naturally good' polymeric conjugating vehicle for delivery of injectable therapeutics. **2014**, 10.1517/17425247.2015.978282, doi:10.1517/17425247.2015.978282.
173. Yang, T.-H.; Shi, Y.; Janssen, A.; Xia, Y. Surface Capping Agents and Their Roles in Shape-Controlled Synthesis of Colloidal Metal Nanocrystals. *Angewandte Chemie International Edition* **2020**, *59*, 15378-15401, doi:https://doi.org/10.1002/anie.201911135.
174. Scarabelli, L.; Sánchez-Iglesias, A.; Pérez-Juste, J.; Liz-Marzán, L.M. A “Tips and Tricks” Practical Guide to the Synthesis of Gold Nanorods. *The Journal of Physical Chemistry Letters* **2015**, *6*, 4270-4279, doi:10.1021/acs.jpclett.5b02123.

175. Personick, M.L.; Mirkin, C.A. Making Sense of the Mayhem behind Shape Control in the Synthesis of Gold Nanoparticles. *Journal of the American Chemical Society* **2013**, *135*, 18238-18247, doi:10.1021/ja408645b.
176. Walkey, C.D.; Olsen, J.B.; Song, F.; Liu, R.; Guo, H.; Olsen, D.W.H.; Cohen, Y.; Emili, A.; Chan, W.C.W. Protein Corona Fingerprinting Predicts the Cellular Interaction of Gold and Silver Nanoparticles. *ACS Nano* **2014**, *8*, 2439-2455, doi:10.1021/nn406018q.
177. Farkas, N.; Kramar, J.A. Dynamic light scattering distributions by any means. *Journal of Nanoparticle Research* **2021**, *23*, 120, doi:10.1007/s11051-021-05220-6.
178. Perera, Y.R.; Xu, J.X.; Amarasekara, D.L.; Hughes, A.C.; Abbood, I.; Fitzkee, N.C. Understanding the Adsorption of Peptides and Proteins onto PEGylated Gold Nanoparticles. In *Molecules*, 2021; Vol. 26.
179. Zhang, Z.-L.; Pang, D.-W.; Yuan, H.; Cai, R.-X.; Abruña, H.D. Electrochemical DNA sensing based on gold nanoparticle amplification. *Anal. Bioanal. Chem.* **2005**, *381*, 833-838, doi:https://doi.org/10.1007/s00216-004-2972-8.
180. Hossen, M.N.; Rao, G.; Dey, A.; Robertson, J.D.; Bhattacharya, R.; Mukherjee, P. Gold Nanoparticle Transforms Activated Cancer-Associated Fibroblasts to Quiescence. *ACS Appl. Mater. Interfaces* **2019**, *11*, 26060-26068, doi:https://doi.org/10.1021/acsami.9b03313.

Appendix A – Abbreviations

SP-ICP-MS	Single Particle Inductively Coupled Plasma Mass Spectrometry
ICP-MS	Inductively Coupled Plasma Mass Spectrometry
LA-ICP-MS	Laser Ablation ICP-MS
CyTOF	Mass Cytometry
ICP-Q-MS	Quadrupole ICP-MS
TOF-ICP-MS	Time-of-Flight ICP-MS
AuNP	Gold Nanoparticle
DLS	Dynamic Light Scattering
HDD	Hydrodynamic Diameter
PDI	Polydispersity Index
CTAC	Cetyltrimethylammonium Chloride
UV-Vis	Ultraviolet-Visible Spectrophotometry
TEM	Transmission Electron Microscopy
SEM	Scanning Electron Microscopy
PEG	Polyethylene glycol
HEP	Heparosan
Citrate-PR	Citrate Physical Replacement

Appendix B – Electronic Supplementary Information for Chapter 3

The electronic supporting information for Chapter 3 is reproduced here for additional information from Reference 31. Permission for reuse has been granted, see Appendix E.

Materials

We used aqueous gold(III) chloride trihydrate ($HAuCl_4$, SigmaAldrich 520918), sodium citrate tribasic dihydrate (SigmaAldrich S4641), hydroquinone (Sigma-Aldrich, ReagentPlus, ≥ 99.0%), cetyltrimethylammonium bromide (CTAB, SigmaAldrich H6269), sodium borohydride ($NaBH_4$, 213462), cetyltrimethylammonium chloride (CTAC, SigmaAldrich 292737), and L-ascorbic acid (AA, SigmaAldrich 255564) to synthesize gold nanoparticles (AuNPs) using different methods. We cleaned Glassware for synthesis and digested cell samples for ICP-MS using hydrochloric acid (HCl, SigmaAldrich ACS reagent 37%) and nitric acid (HNO_3, SigmaAldrich ACS reagent 70%). We used Tween20 (SigmaAldrich P9416) during the centrifugation and purification of AuNPs. We PEGylated AuNPs using 5-kDa methoxy-PEG-thiol (mPEG-SH, Laysan Bio) or 5-kDa maleimide-PEG-OPSS (malPEG-OPSS, Laysan Bio).

We used DNA strands from Integrated DNA Technologies (IDT). We composed DNA storage and reaction buffers using mixtures of tris(hydroxymethyl)aminomethane ACS reagent ≥99.8% (Tris, SigmaAldrich 252859), ethylenediaminetetraacetic acid BioUltra, anhydrous ≥99% (EDTA, SigmaAldrich EDS), or sodium chloride (NaCl S7653). We purified DNA using illlustra NAP-5 columns (GE Healthcare 17-0853-01). We implemented the peptide K7C (Biomatik, amino acid sequence N'-C' KKKKKKKC) to improve cell uptake of AuNPs in cells.

TEM imaging was completed on copper TEM grids with carbon film (Ted Pella, 01813-F).

In preparing RAW 264.7 macrophages for confocal laser scanning microscopy (CLSM), we used NucBlue DAPI (Invitrogen R37606) to label cell nuclei and wheat germ agglutinin CF488A (WGA, Biotium 29024) to label glycoproteins on cell membranes. We suspended both labeling agents in 1x Hank's balanced salt solution (HBSS, Gibco 14185-052) in 1x phosphate buffered saline (PBS, ThermoFisher BP3994). We cleaned the microscopy coverslips using a mixed solution of hydrogen peroxide (H_2O_2, SigmaAldrich 216763) and sulfuric acid (H_2SO_4, Avantor 7664-93-9).

Instrumentation

CTAC-capped AuNP synthesis was performed using Harvard Apparatus PHD ULTRA syringe pumps (Harvard Apparatus 703005). Vortexing steps for physical replacement PEGylation were carried out using VWR® Analog Vortex Mixers (Avantor 10153-838). Dynamic light scattering (DLS) and zeta potential measurements were carried out on a Malvern Zetasizer NanoZS. Ultraviolet-visible spectrophotometry measurements were performed using a UV-Vis-NIR spectrophotometer (Agilent Cary 5000). Transmission electron microscopy (TEM) images were collected on a JEOL 2010F Field Emission TEM with a Direct Electron DE-12 camera. We conducted SP-ICP-MS analysis of AuNPs using a PerkinElmer NexION 2000 ICP-MS instrument with a single cell introduction system (PerkinElmer N8150032) and the PerkinElmer Single Cell Application software. We performed confocal microscopy imaging using a ZEISS LSM 880 inverted CLSM with a photomultiplier tube (PMT) detector, a 405 nm diode laser, a

488 nm argon laser, a 561 nm diode-pumped solid-state laser for fluorescent channels through a main beam splitter (MBS) 488/561/633 filter.

Synthesis of Citrate-capped Gold Nanoparticles

We synthesized citrate-capped AuNPs by following established protocols.[117,118,128] We first made a 0.25-M solution of $HAuCl_4$ by dissolving 984 mg of $HAuCl_4$ in 10 mL of nanopure water (18.2 MΩ-cm). To synthesize larger citrate-capped AuNPs, 14-nm citrate-capped AuNP seeds are required. To synthesize these seeds, we cleaned a 250-mL Erlenmeyer flask using 80 mL of aqua regia (3:1 v/v $HCl:HNO_3$). We added ~100 mL of nanopure water to the cleaned flask and then added 1 mL of a 30-mg/mL solution of aqueous sodium citrate tribasic dihydrate (0.102 M). We gently mixed the resulting solution using a Teflon-coated magnetic stir bar and heated the solution to boiling. Once the solution was boiling, we rapidly added 100 µL of 0.25-M $HAuCl_4$ and stirred the solution vigorously. We allowed the reaction to run for 7 min, during which time the solution color changed from clear to purple to red. We then rapidly cooled the gold nanoparticles (AuNPs) to room temperature by placing the Erlenmeyer flask on ice. We characterized the resulting 14-nm citrate-capped AuNP seeds by dynamic light scattering (DLS) and ultraviolet-visible spectrophotometry (UV-Vis) prior to use in subsequent AuNP growth or characterization. We aliquoted 20 mL of the resulting 14-nm AuNP solution for purification and further characterization; the remaining solution was used for continued AuNP growth. To purify the 14-nm AuNPs, we added 200 µL of a 10% Tween20 solution in nanopure water (final concentration of 0.01% Tween20), aliquoted the solution into 50-mL tubes, and centrifuged at 15,000 relative centrifugal force (rcf, 1 rcf=1x g-force) for 90 min at 4°C. We removed the supernatant, resuspended the resulting pellet in 0.01%

Tween solution, aliquoted the solution into 1.5-mL tubes, and centrifuged once more for 30 min at 4°C. The purified 14-nm AuNPs were characterized by DLS, UV-Vis, transmission electron microscopy (TEM), and single-particle inductively coupled plasma mass spectrometry (SP-ICP-MS).

Using the as-synthesized (i.e. not purified) 14-nm AuNP seeds, we grew citrate-capped AuNPs of >14 nm diameters. We performed AuNP growth in 250-mL Erlenmeyer flasks cleaned using aqua regia, as described. To grow AuNPs, we swiftly added cold nanopure water, 0.025-M $HAuCl_4$, 0.015-M aqueous sodium citrate tribasic dihydrate, 2.4-nM 14-nm AuNP seeds, and 0.025-M hydroquinone to the flask under vigorous stirring and let the reaction run overnight. The final diameter of citrate-capped AuNPs is controlled primarily through the molar ratio of $HAuCl_4$ to 14-nm AuNPs, as reported previously.[118] Our final reaction volume was 100 mL, and Table S1 details the volumes of $HAuCl_4$ and 14-nm AuNP solutions used for each final target AuNP diameter. The volume of 0.015-M aqueous sodium citrate tribasic dihydrate and 0.025-M hydroquinone added should equal the volume of $HAuCl_4$ added. After the overnight reaction, we added 1 mL of a 10% Tween20 solution to the flask, aliquoted the reaction solution in 50-mL tubes, and centrifuged it for 90 min at 4°C. Following this centrifugation, we removed the supernatant, resuspended the pellets in 1.5-mL tubes using 0.1% Tween20 solution, and centrifuged again for 30 min at 4°C. We adjusted the centrifugation speed depending on the target size of the grown AuNPs (Table S1). After the final centrifugation, we resuspended the pellets in 0.1% Tween20 solution. We characterized the final AuNPs by DLS, UV-Vis, TEM, and SP-ICP-MS. To produce enough 60-nm citrate-capped AuNPs, we repeated this procedure scaled-up 10x by volume.

Synthesis of CTAC-capped Gold Nanoparticles

We followed established protocols to synthesize CTAC-capped AuNPs.[119,123,124] Synthesis of CTAC-capped AuNPs occurs in stages. First, we created Au-clusters that serve as the nucleation sites for making the seeds for growing larger AuNPs. To make Au-clusters, we cleaned a 20-mL glass scintillation vial using 10 mL aqua regia (3:1 v/v $HCl:HNO_3$). After cleaning, we set the vial to heat up to 30°C on a hot plate before adding 500 µL of a 5-mM $HAuCl_4$ solution and 9.5 mL of a 30°C 38-M CTAB solution. We mixed the vial contents rapidly using a Teflon-coated magnetic stir bar, resulting in an orange color. Separately, we prepared 600 µL fresh, ice-cold solution of 0.1-M $NaBH_4$, which was added to the 20-mL scintillation vial. After 2 min of rapid mixing, the vial contents changed color from orange to brown (Figure C3.1a). After mixing, we let the Au-cluster solution remain on the hot plate for 3 hours before characterizing the cluster solution by UV-Vis (Figure C3.1b). Per the methods by Zheng *et al*., we used the extinction value of the clusters at the extinction wavelength of 390 nm to determine the volume of clusters to use in subsequent steps.[119,124]

Compared to established protocols, we scaled up the synthesis of CTAC-capped 10-nm AuNP seeds to ensure we had a sufficient number of seeds for all experiments. In our approach, we cleaned a 250-mL Erlenmeyer flask using aqua regia, as previously described. We placed the clean flask on a hot plate set for 25°C and added the following solutions in order: 16.54 mL of nanopure water, 20 mL of 110-mM CTAC solution, 8.46 mL of 0.17-M ascorbic acid (AA), and 941 µL of our Au-clusters (extinction value at λ=390 nm of 0.42). We estimated the volume of Au-clusters needed based on the extinction value at λ=390 nm based on prior studies.[119,124] We vigorously mixed the resulting

solution using a Teflon-coated magnetic stir bar for 5 min before adding 10 mL of 1-mM $HAuCl_4$ via one-shot injection into the solution. We continued mixing the solution for 15 min. before centrifuging the solution at 21,000 rcf for 90 min at 4°C. We washed the resulting pellet in nanopure water before centrifuging again at 21,000 rcf for 90 min at 4°C. After this second centrifugation, we suspended the pellet in 20-mM CTAC solution and characterized the 10-nm CTAC-capped AuNP seeds by DLS, UV-Vis, and TEM (Figure C3.2).

Our 10-nm CTAC-capped AuNP seeds served as the sites for growing larger CTAC-capped AuNPs. The final AuNP size was controlled by changing the mole amount of 10-nm CTAC-capped AuNP seeds (Table D3.2). Our 10-nm CTAC-capped AuNP seed solution was measured to have a concentration of 19.9 nM by UV-Vis. To grow CTAC-capped AuNPs, we first cleaned a 250-mL Erlenmeyer flask using aqua regia as previously described. This flask was put on a hot plate set for 35°C. We prepared a 20-mL solution of 100-mM CTAC in nanopure water with the appropriate volume of 10-nm CTAC-capped AuNP seed solution and, after sonicating it for 1 min, added it to the flask. To this flask, we then added 1.3 mL of 10-mM AA. After 1 min of stirring, we added 20 mL total of 0.625-mM $HAuCl_4$ solution via dropwise addition controlled by syringe pumps set to pump at 20 mL/hr. After 1 hour, we let the reaction continue to run for 15 min before removing the flask from heat and centrifuging. We centrifuged the final reaction solution twice – once for 90 min at 4°C with resuspending in nanopure water and once for 30 min at 4°C with resuspending in 20 mM CTAC solution. Centrifugation speed was varied based on the final targeted AuNP diameter (Table D3.2). After purification, CTAC-capped AuNPs were characterized by DLS, UV-Vis, TEM, and SP-ICP-MS. To ensure we had

enough 60-nm CTAC-capped AuNPs, we synthesized an additional batch that was scaled up 2x by concentration and 2x by volume (total 4x scale-up).

SP-ICP-MS Transport Efficiency Calculations and Sample Preparation

To measure the mass distribution of synthesized AuNPs, we performed quantitative SP-ICP-MS measurements. We completed the measurements using a PerkinElmer NexION 2000 ICP-MS using a high-efficiency sample introduction comprised of a nebulizer, spray chamber, and a heating element wrapped around the spray chamber. The heating element limits condensation on the interior of the spray chamber, improving the transport efficiency (TE) of introduced AuNPs. Transport efficiency was measured using commercially available 3-µm polystyrene microparticles doped with Lu175 (Fluidigm). We measured the transport efficiency as being ~70% using previously established methods.[116,117] The conditions we used for data collection were optimized for SP-ICP-MS data collection by using a NexION setup solution (PerkinElmer, N8145051) to affirm consistent ion signal (Table D3.3). Further, AuNP mass was measured using a particle calibration curve generated using synthesized AuNP standards (Figure C3.5). Following earlier studies, we confirmed the diameter of AuNP standards by DLS and TEM before using them in establishing the particle calibration curve.[21,116,117] We diluted all AuNPs to ~$3x10^{-16}$ M in nanopure water prior to measurement to limit signal overlap from dual-event readings.

PEGylation of Synthesized AuNPs

For citrate-capped AuNPs, we PEGylated according to established protocols.[117,128] We added purified citrate-capped AuNPs to a concentrated solution of

0.1% Tween20 and either mPEG-SH or malPEG-OPSS, depending on the experiment to be performed. We incubated the AuNP-PEG mixture for 30 min at room temperature before characterizing it by DLS to affirm an increase in hydrodynamic diameter. The concentration of the PEG solution was such that the final PEG density added could be up to 7 PEG molecules per nm^2 of available AuNP surface area. This PEG surface density exceeds the known saturation point for PEG ligands on the surface of AuNPs, ensuring that the maximal PEG possible is conjugated to the surface of the AuNPs.[128]

The PEGylation method used for citrate-capped AuNPs does not work for CTAC-capped AuNPs. Therefore, we devised a physical replacement method by which CTAC can be replaced by PEG. Our approach is inspired by similar methods from other studies.[129,130] We started by centrifuging purified CTAC-capped AuNPs, using the appropriate speed (Table D3.2) to recover AuNP pellets. After removing the supernatant, we resuspended the AuNP pellet in 50 µL of a solution of 0.1% Tween and either concentrated mPEG-SH or malPEG-OPSS, depending on the experiment to be performed. We set the concentration of PEG in this resuspension solution such that the PEG surface density added would be ~2.3 PEG molecules per nm^2. After we suspended the pellets, we sonicated for 1 min before vortexing vigorously (~3200 rcf) for 30 s. After vortexing, we diluted to 1 mL using 0.1% Tween and centrifuged again. We repeated this PEGylation process two more times for three vortexing steps. Thus, the final estimated PEG surface density added would be ~7 PEG molecules per nm^2. After the third PEGylation step, we centrifuged one more time to remove excess PEG prior to characterization by DLS, UV-Vis, TEM, and SP-ICP-MS.

While we attempted to indicate PEG presence on PEGylated CTAC-capped AuNPs via negative staining with 2% uranyl acetate solution, we detected no discernible difference between CTAC-capped AuNPs before or after PEGylation (Figure C3.8).

DNA Conjugation and Hybridization for DNA-AuNP Superstructures

To synthesize DNA-AuNP superstructures in-line with those seen in previous studies, we first started by making a 1x TE buffer comprised of 10-mM Tris and 1-mM EDTA. We adjusted the pH of the buffer to 8.0 by adding HCl and suspended ordered DNA in the buffer before freezing at negative 20°C prior to use. We selected DNA sequences based on prior studies and used DNA strands modified with thiol (-SH) end groups to allow for maleimide-thiol chemistry to drive conjugation to AuNPs.[132,179] Before use in AuNP conjugation, we first reduced aliquots of the thiolated DNA with Tris(2-carboxyethyl)phosphine (TCEP, SigmaAldrich C4706) using 100x molar concentration. To purify the reduced DNA and resuspend in an alternative buffer, we ran the DNA through illustra NAP-5 columns and resuspended the DNA in a neutral buffer comprised of 1.5-M NaCl and 0.015-M aqueous sodium citrate tribasic dihydrate (pH 7.0). This buffer exchange is necessary to ensure the pH conditions promote maleimide-thiol reaction chemistry when conjugating to AuNPs.[131] We confirmed DNA concentration using UV-Vis prior to use in subsequent steps.

After quantifying the DNA, 60-nm and 15-nm diameter CTAC-capped AuNPs were PEGylated using 5-kDa malPEG-OPSS as described. After PEGylation, we centrifuged the AuNPs to remove excess PEG and resuspended the AuNP pellets in a solution of concentrated thiolated DNA. We added OligoA to the 60-nm AuNPs and OligoB to the 15-nm AuNPs. We diluted the DNA solution such that there could be an added maximum

of 7 DNA molecules per nm^2 on the surface of the AuNPs. As with our PEG methods, we expect this added seven ligand molecules per nm^2 surface density to exceed the saturation point on the surface of the AuNPs, resulting in maximal DNA binding to the AuNPs by thiol-maleimide chemistry. After incubating the DNA-AuNP solutions overnight, we centrifuged three times to remove excess DNA, resuspending in a 0.1% Tween 1x PBS solution each time. We characterized DNA-conjugated AuNPs by DLS to confirm DNA presence by detecting differences in hydrodynamic diameter compared to PEGylated controls.

To create DNA-AuNP superstructures, we first centrifuged the DNA-conjugated 60-nm AuNPs down to a pellet. We resuspended this pellet in 100 µL of a 1x TE buffer solution containing the DNA Linker strand. We incubated this DNA-AuNP solution at 37°C for 2 hours, then cooled the solution to room temperature for ~20 min. To remove excess linker, we centrifuged the Linker-DNA-AuNP mixture three times, resuspending in 0.1% Tween 1x PBS after each centrifugation. At the last incubation step, the pellet was resuspended in a solution containing the DNA-conjugated 15 nm AuNPs, allowing for hybridization between the 15 nm AuNPs and the Linker DNA hybridized to the 60-nm AuNPs. We incubated this mixture of DNA-conjugated AuNPs for 2 hours at 37°C before cooling to room temperature, as before. We then centrifuged at 1200 rcf three times to remove as many excess 15-nm AuNPs as possible based on their lower mass. The final superstructures were characterized by DLS and TEM.

The concentration of the Linker strand was set such that there would be 25 DNA Linker molecules added to one 60-nm AuNP (25:1 DNA:AuNP ratio). We selected this ratio based on prior studies to limit the saturation of the AuNP with linker strands and,

subsequently, with hybridized 15-nm AuNPs.[132] Conversely, we added enough DNA-conjugated 15-nm diameter AuNPs to ensure all available linker strands on the surface of the 60-nm AuNPs were occupied. Thus, we added enough 15-nm AuNPs to have 100 15-nm AuNPs for every one 60-nm AuNP (100:1 satellite-to-core ratio).

Cell Culture Conditions

We cultured DC 2.4 murine dendritic cells in T-75 flasks with RPMI 1640 cell culture media (ATCC 30-2001) supplemented with 1% Penicillin Streptomycin (pen-strep, Gibco 15140122) and 10% fetal bovine serum (FBS). Separately, we cultured RAW 264.7 murine macrophages in T-75 flasks with DMEM cell culture media (ThermoFisher 11995073) supplemented with 1% Penicillin Streptomycin and 10% fetal bovine serum (FBS, ThermoFisher 16000044). We incubated cells at 37°C with 5% CO_2 until confluent. We used trypsin-mediated release to recover and count adherent cells prior to XTT, microscopy, or ICP-MS cell experiments.

XTT Viability Methods

We performed cell viability tests to confirm that our PEGylation method completely removed CTAC and imparted biocompatibility on originally CTAC-capped AuNPs. We also performed these tests to ensure that our K7C-conjugated AuNPs of both citrate- and CTAC-capped origins would not impact cell viability. In all cases, we performed cell viability assays as previously reported in other studies.[32,34,180] We seeded cells in 96-well plates and allowed them to incubate for 24 hours prior to AuNP incubation. For Figure 5a, we seeded 10,000 cells/well using DC 2.4 murine dendritic cells in RPMI 1640 with 1% pen-strep and 10% FBS. For Figures 5b and 5c, we seeded 10,000 cells/well and

22,000 cells/well, respectively, using RAW 264.7 murine macrophages in DMEM with 1% pen-strep and 10% FBS. After incubating for 24 hours, we treated cells with 100 µL of 0.1-nM AuNP groups in appropriate media as described. After incubating with AuNPs overnight (Figures 3.5a and 3.5b) or for 3 hours (Figure 3.5c), we aspirated well contents out, and wells were washed two times with 100 µL 1x PBS. To measure viability, we used the XTT assay (2,3-Bis-(2-Methoxy-4-Nitro-5-Sulfophenyl)-2H-Tetrazolium-5-Carboxanilide, SigmaAldrich 11465015001) method according to the manufacturer's instructions. We assessed cell viability by measuring the absorbance of formazan in dimethyl sulfoxide (DMSO) at 570 nm and normalizing each group to the cell-only group after subtracting any absorbance associated with the well-plate or media contents.

Confocal Laser Scanning Microscopy Preparation and Image Collection

To better visualize the uptake of 60-nm AuNPs by RAW 264.7 macrophages, we performed imaging analysis using confocal laser scanning microscopy (CLSM). We performed the cell preparation, treatment, and imaging using previously established methods.[32] We first cleaned 18-mm round microscopy coverslips using 20 mL of a 3:1 v/v mixture of sulfuric acid and hydrogen peroxide. After being immersed for 15 min, we removed the coverslips and rinsed them thoroughly with nanopure water. We placed the coverslips in separate wells of a 12-well plate before treating the plate with UV light for 10 min. To each well with a coverslip, we added 500 µL containing 15,000 cells/well of RAW 264.7 macrophages in DMEM with 1% pen-strep and 10% FBS. We allowed cells to incubate for 24 hours before aspirating out media and adding in media with 0.01-nM of AuNP treatments as described. After incubating for 3 hours, we aspirated out the media and washed with 1x PBS three times to remove excess AuNPs. We then added 500 µL

4% paraformaldehyde (PFA, ThermoFisher AAJ19943K2) at room temperature for 10 minutes to fix cells. After fixing the cells, we stained the cells using DAPI and WGA according to the manufacturer's protocols to label the cell nuclei and membrane, respectively. We imaged each coverslip using a 63x oil immersion objective (1.4 NA) on a ZEISS LSM 880 inverted confocal laser microscope with the specification detailed above and using the Zen Black imaging software. We successfully imaged AuNPs in the cells and on the slides by applying the light scattering principles previously described.[144,145]

ICP-MS Sample Preparation and Measurement

Measurement of AuNP cell uptake by ICP-MS followed established methods.[32,34] We PEGylated citrate-capped AuNPs with 5-kDa mPEG-SH or 5-kDa malPEG-OPSS as described. Separately, we PEGylated CTAC-capped AuNPs with 5-kDa mPEG-SH or 5-kDa malPEG-OPSS as described. We added seven K7C/nm^2 to both AuNP groups with malPEG-OPSS to bio-functionalize the AuNPs. We cultured 2e5 RAW 264.7 cells/well in a 48-well plate. We then gave each well either no AuNPs, PEGylated citrate-capped AuNPs, K7C citrate-capped AuNPs, PEGylated CTAC-capped AuNPs, or K7C CTAC-capped AuNPs. We used a concentration of 0.01 nM for all AuNP groups. Separately, a 48-well plate with no cells was treated with all four AuNP groups. After 3 h incubation with the nanoparticles, we washed half the wells two times with 1x PBS and the other half the wells rapidly with dilute KI/I_2 gold etchant solution (4 µL into 40 µL 1x PBS), followed by two times with 1x PBS. We then stored the well plates at 4°C overnight. The following day, we added 500 µL aqua regia (1:4 v/v HCl:HNO_3) to each well and incubated for 30 min. at room temperature. After 30 min, we transferred well contents to 1.5-mL tubes,

which were immediately placed into a 70 °C water bath. After 60 min., tube contents were diluted to 5 mL in nanopure water and immediately measured by ICP-MS.

ICP-MS measurements were performed in the form of signal intensity values. To translate these into more applicable concentration values, we used the data from Au^{3+} and cell standards to generate calibration curves relating Au^{3+} or Mg^{2+} signal intensity with Au or cell concentration, respectively (Figure C3.9). Using this information, we estimated the number of AuNPs/cell by calculating the number of AuNPs per sample, assuming a constant diameter of 60 nm. Note: this assumption is leniently applied given the observed differences in AuNP monodispersity, as discussed previously. We then calculated the number of cells based on the Mg^{2+} signal of each measurement, giving us the final value needed to estimate AuNP uptake.

Appendix C – Supporting Figures

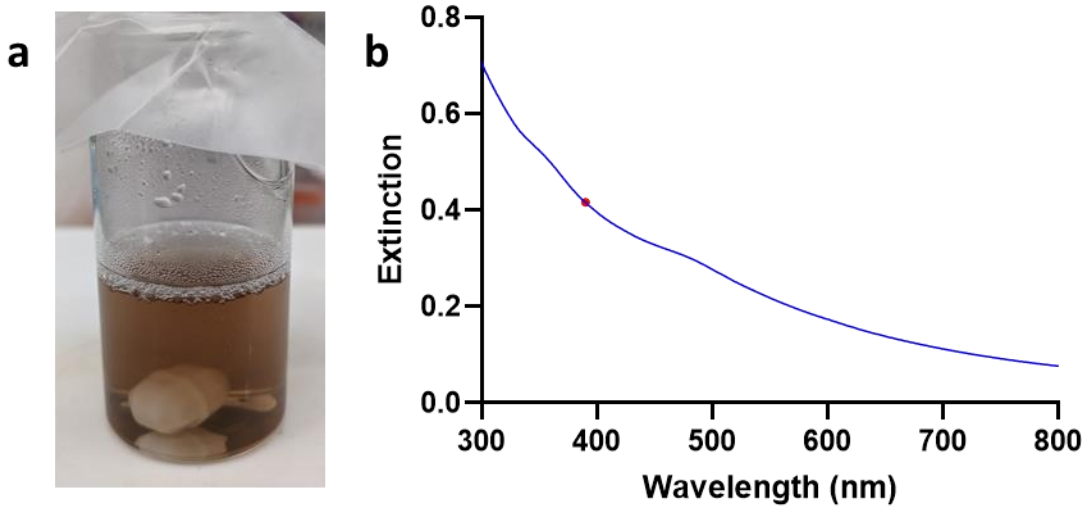

Figure C3.1: Au-clusters characterization preceding CTAC-capped AuNP synthesis. a) The Au-cluster solution in a 20-mL glass scintillation after 3 h incubation has a deep brown color, as shown. **b)** UV-Vis extinction spectra of the post-incubation Au-cluster solution. The red dot indicates the extinction value at λ=390 nm used to determine the volume of clusters needed for subsequent synthesis steps. This extinction wavelength was selected based on prior studies using Au-clusters for AuNP synthesis.[119,124]

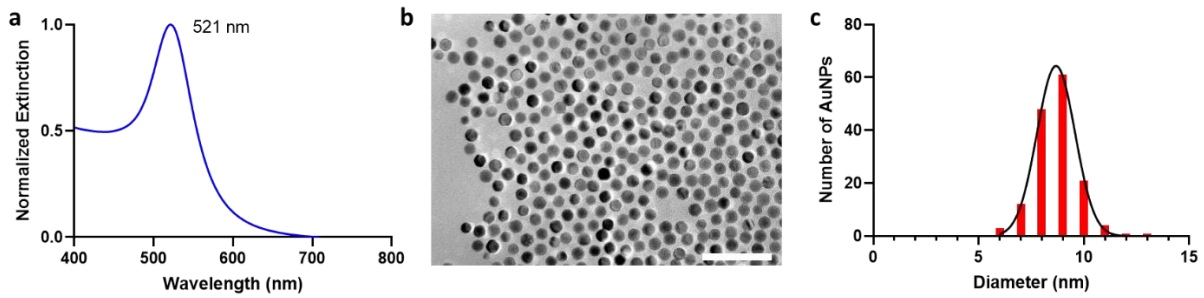

Figure C3.2: Characterization of 10-nm diameter CTAC-capped AuNPs. a) Normalized UV-Vis extinction spectra of synthesized seeds with the peak extinction wavelength shown. **b)** TEM micrograph of synthesized seeds. The scale bar is 50 nm. **c)** Size distribution analysis of synthesized seeds based on TEM micrographs. While the target diameter was 10 nm, the mean diameter was found to be 8.9 nm ± 0.9 nm.

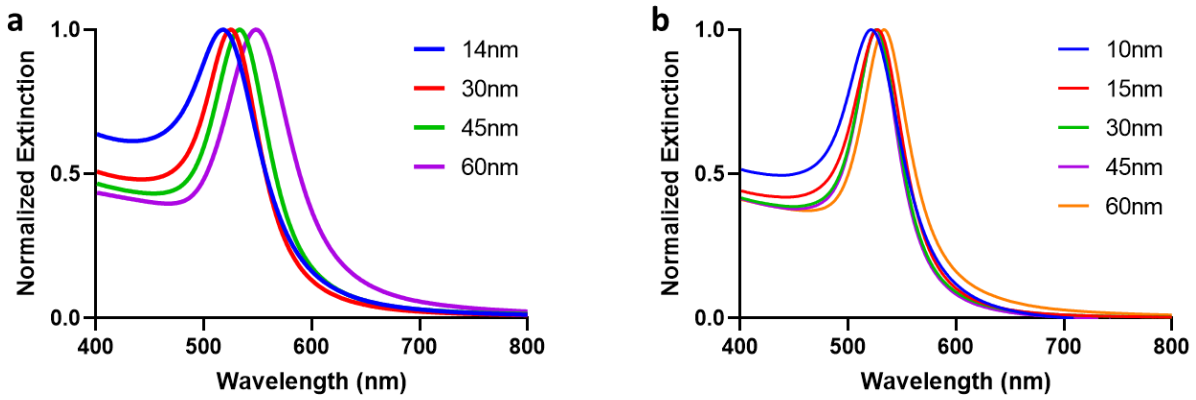

Figure C3.3: Comparison of UV-Vis extinction spectra between synthesized AuNPs.

Notably, the peak extinction wavelength and the spectral width of the citrate-capped AuNPs (C3.3a) are larger than the same values of the corresponding CTAC-capped AuNPs (C3.3b).

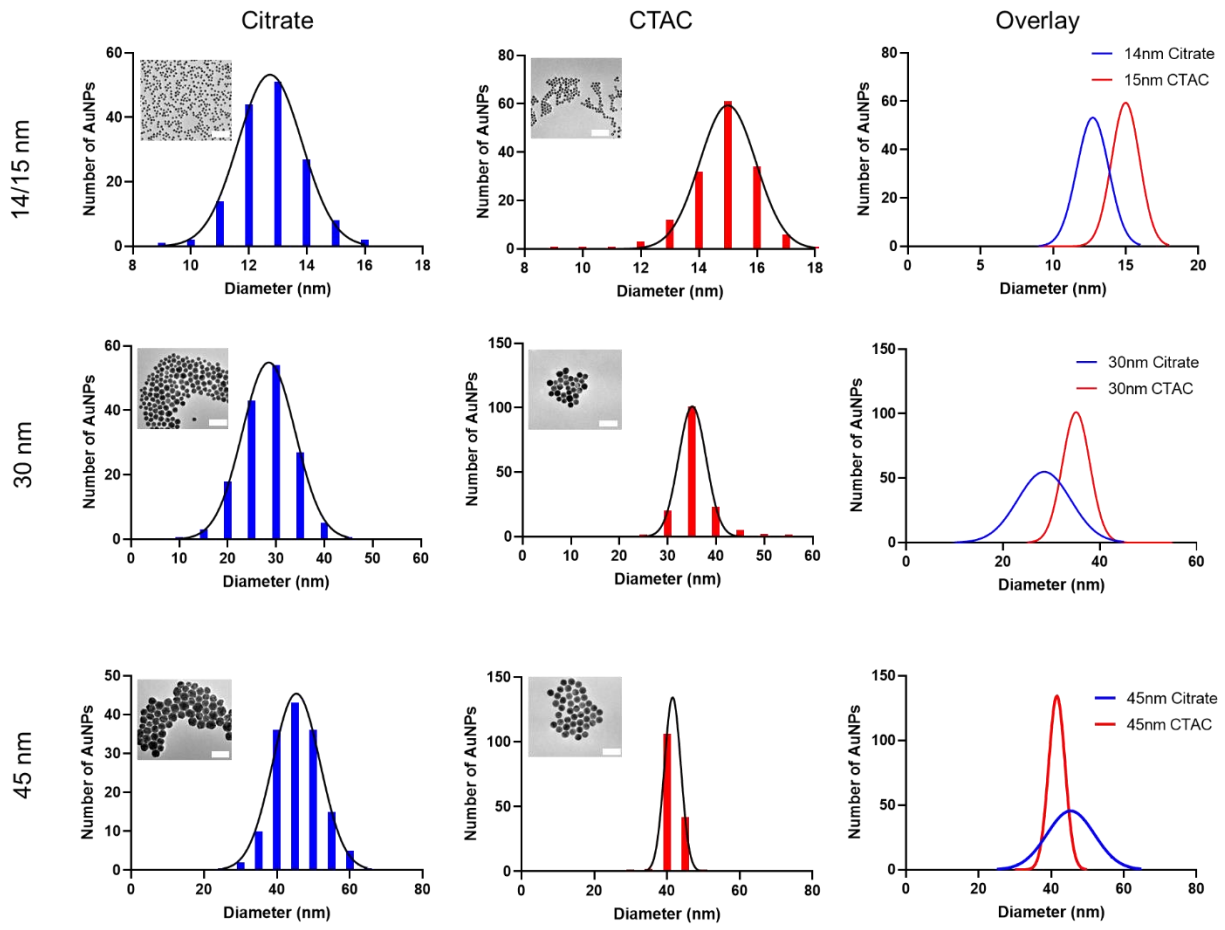

Figure C3.4: TEM size distributions of synthesized AuNPs. Colored bars represent the frequency of AuNPs of each diameter, while black lines represent Gaussian normal distributions of the data. Distributions were taken for N=150 AuNPs. Scale bars of TEM micrograph inserts indicate 100 nm. The far-right column of the graphs shows the overlap in the Gaussian normal mass distributions, generally demonstrating any difference in monodispersity between the citrate- and CTAC-capped AuNPs.

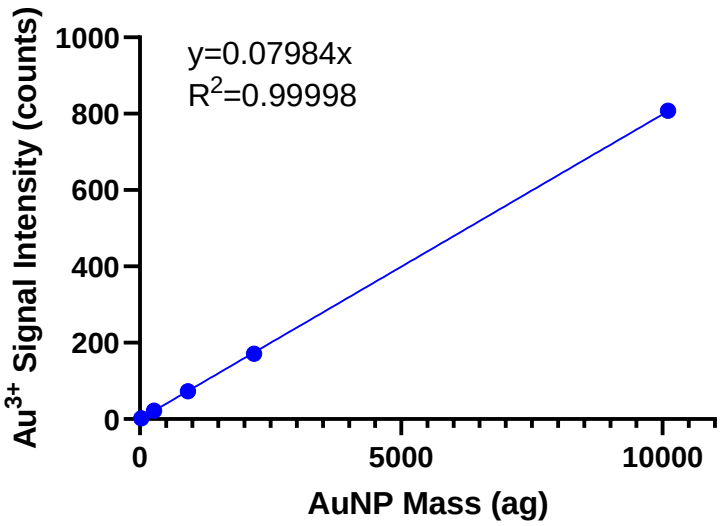

Figure C3.5: AuNP calibration curve for SP-ICP-MS. When AuNPs are ionized in the plasma torch during SP-ICP-MS sample introduction, the resulting ion cloud is measured as a signal intensity of Au^{3+} ions. The signal intensity is correlated to the mass of the AuNPs to generate a robust linear calibration curve.

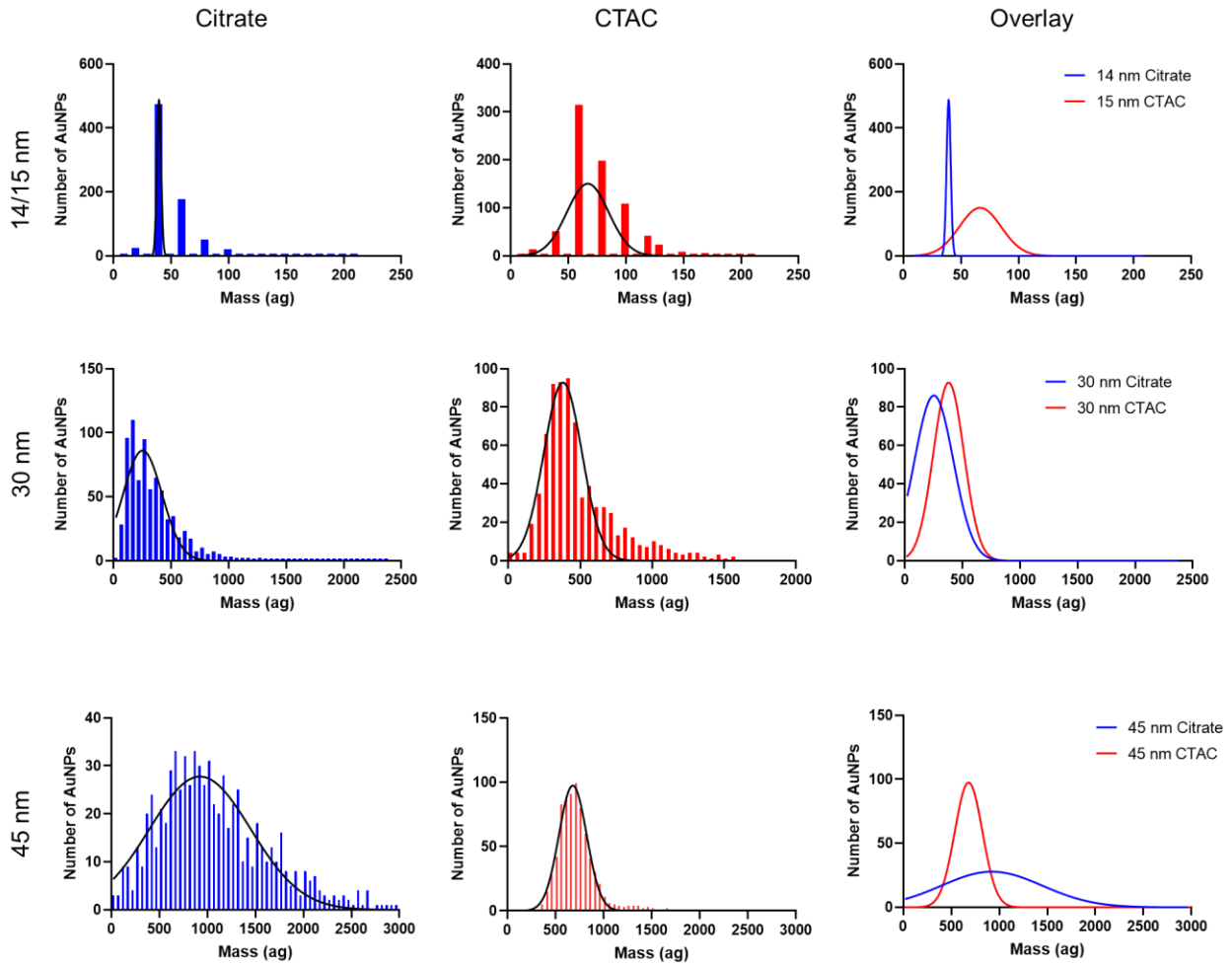

Figure C3.6: Measured mass distributions of synthesized AuNPs. Colored lines indicate frequency values for each mass, while black lines indicate Gaussian normal distributions. All distributions were normalized for N=750 AuNPs. The far-right column of graphs shows the overlap in the Gaussian normal mass distributions, demonstrating any difference in monodispersity between the citrate- and CTAC-capped AuNPs.

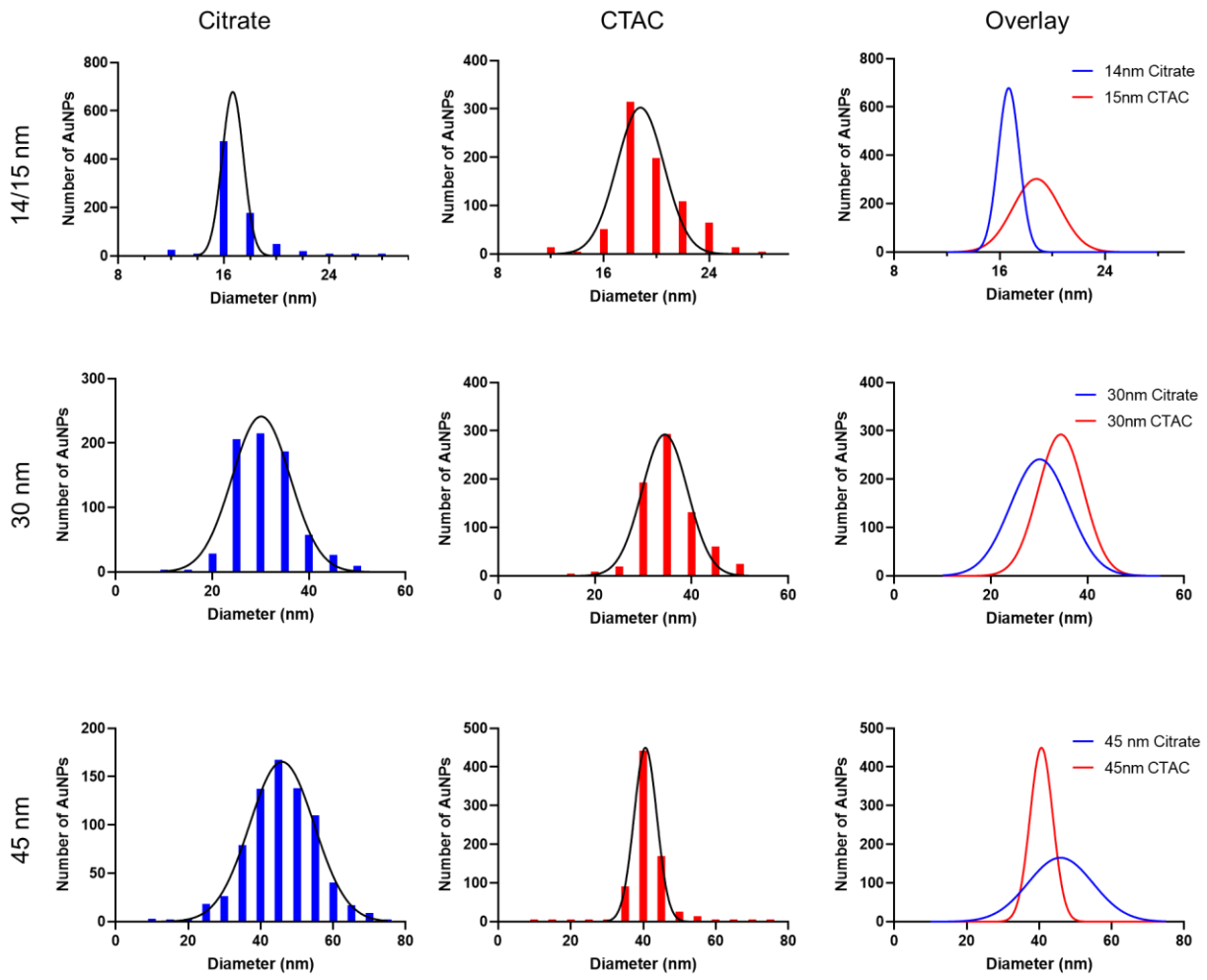

Figure C3.7: Measured size distributions of synthesized AuNPs. Colored lines indicate frequency values for each diameter, while black lines indicate Gaussian normal distributions. All distributions were normalized for N=750 AuNPs. The far-right column of the graphs shows the overlap in the Gaussian normal diameter distributions, demonstrating the difference in monodispersity between the citrate- and CTAC-capped AuNPs.

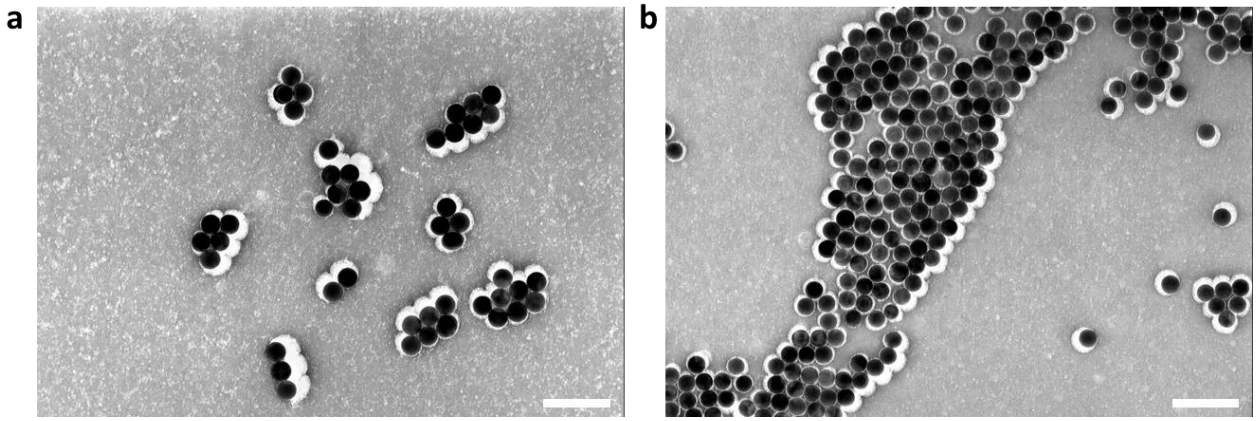

Figure C3.8: TEM images of negatively stained 60 nm diameter CTAC-capped and PEGylated AuNPs. Given the organic nature of CTAC molecules and PEG molecules, negative staining is required to visualize the molecular layer around AuNPs. We used a 2% uranyl acetate solution to stain micrographs of each population. Interestingly, CTAC-capped AuNPs before (C3.8a) and after PEGylation (C3.8b) both show similar staining patterns, demonstrating that alternative means (i.e., DLS) are needed to affirm PEG layer presence on the surface of AuNPs.

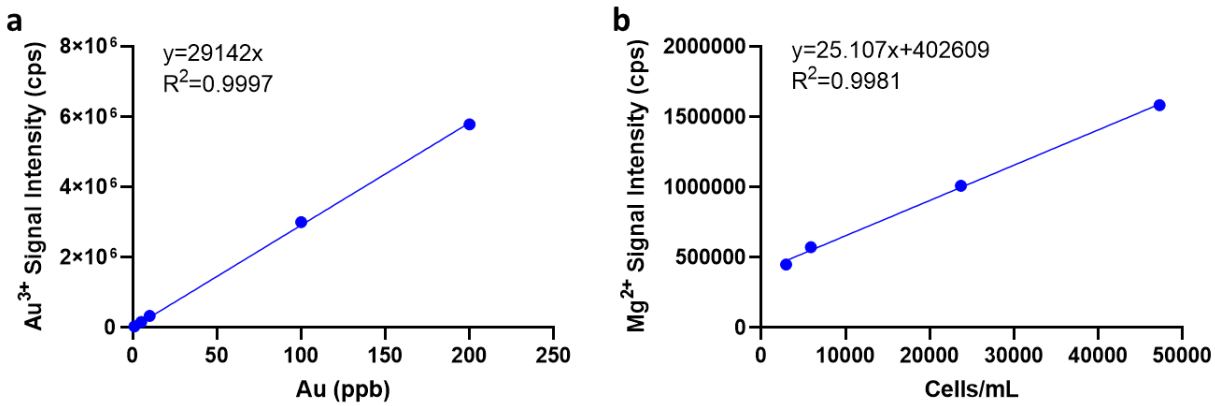

Figure C3.9: Calibration curves for ICP-MS measurements. The linear calibration curves for both Au^{3+} (C3.9a) and Mg^{2+} (C3.9b) demonstrated strong correlations. These curves were used to estimate the number of AuNPs and cells, respectively, for each ICP-MS measurement.

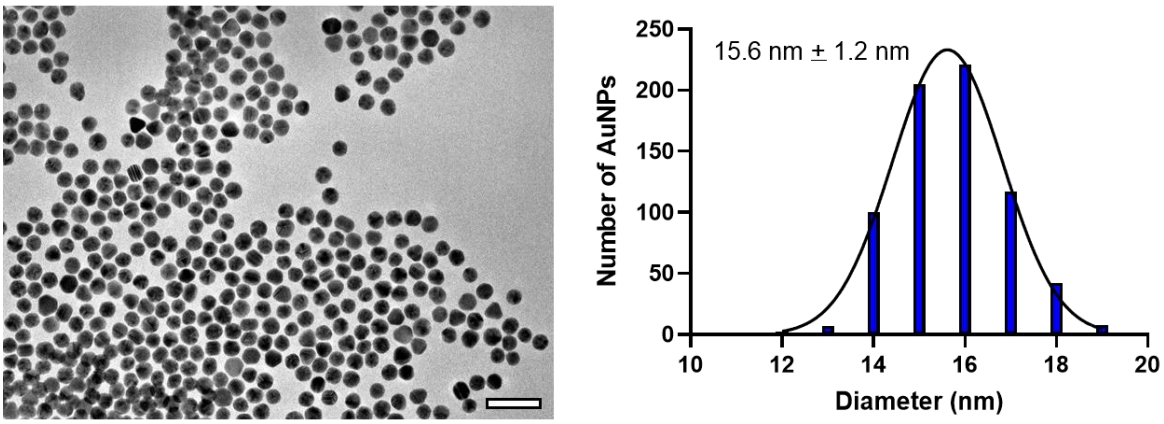

Figure C4.1: Representative TEM image and size distribution of ~14 nm citrate AuNP seeds. TEM micrograph (left) was analyzed using ImageJ to acquire estimated size distribution (right) and correlating mean diameter ± standard deviation estimate. Scale bar of TEM image is 50 nm.

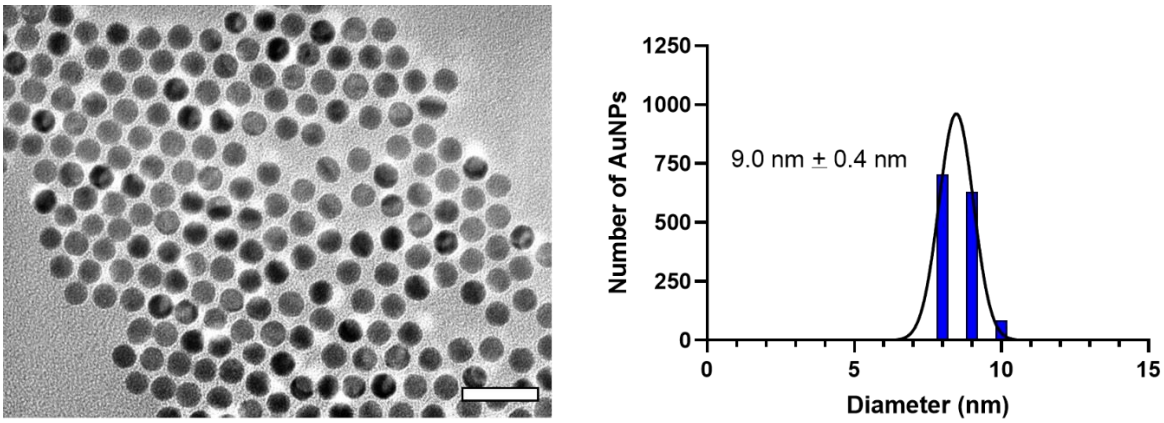

Figure C4.2: Representative TEM image and size distribution of ~10 nm CTAC AuNP seeds. TEM micrograph (left) was analyzed using ImageJ to acquire estimated size distribution (right) and correlating mean diameter ± standard deviation estimate. Scale bar of TEM image is 30 nm.

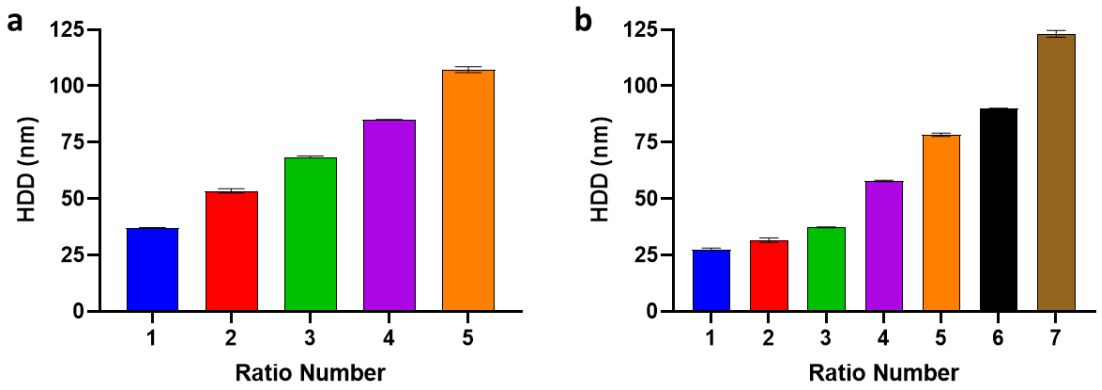

Figure C4.3: HDD measurements of model AuNPs by DLS. (**a)** DLS readings of citrate-based AuNPs immediately after synthesis and purification. Black bars indicate standard deviation of the mean. Ratio number indicates predicted AuNP/Au value assignment, as shown in Table 4.1. **b)** DLS readings of CTAC-based AuNPs immediately after synthesis and purification. Black bars indicate standard deviation of the mean. Ratio number indicates predicted AuNP/Au value assignment, as shown in Table 4.2.

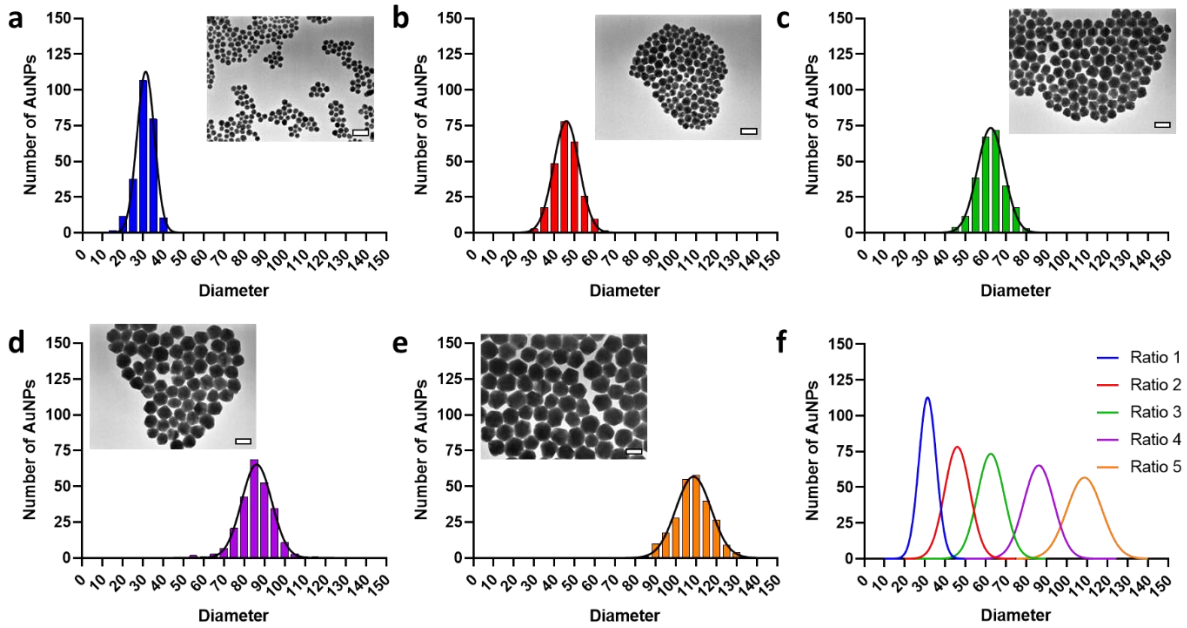

Figure C4.4: TEM characterization of citrate-based AuNPs. **a-e)** Gaussian normal distributions of citrate-based AuNPs diameter estimates from TEM imaging of Ratio 1, Ratio 2, Ratio 3, Ratio 4, and Ratio 5, respectively. Inset TEM images have 100 nm scale bars. For all analysis, distributions were normalized to N = 250 AuNPs. **f)** Overlay of Gaussian normal distributions of TEM estimated diameter for all synthesized citrate-based AuNP ratios.

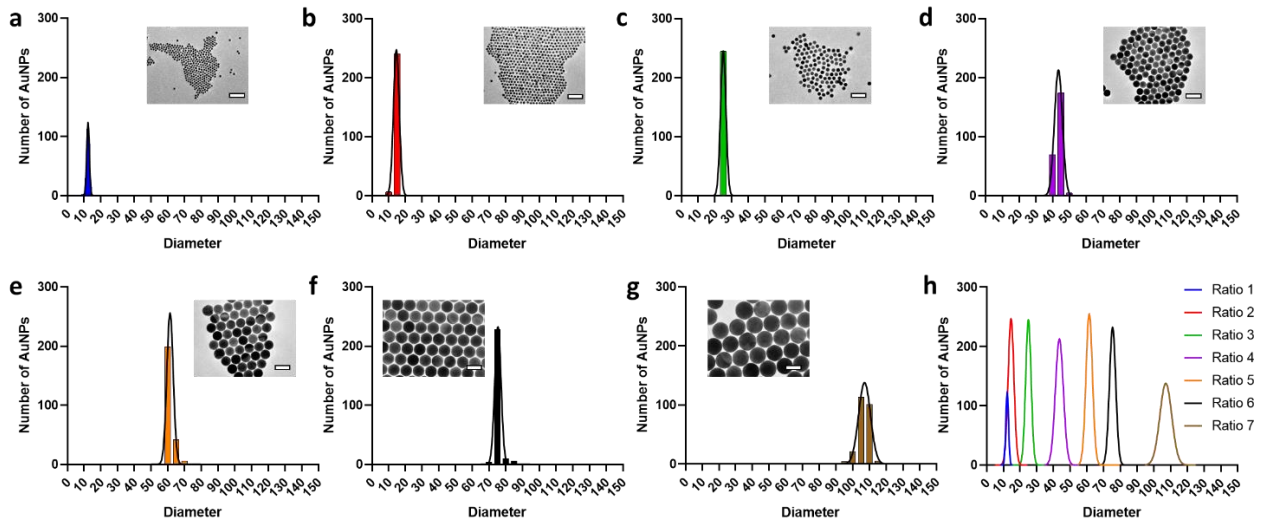

Figure C4.5: TEM characterization of CTAC-based AuNPs. **a-g)** Gaussian normal distributions of CTAC-based AuNPs diameter estimates from TEM imaging of Ratio 1, Ratio 2, Ratio 3, Ratio 4, Ratio 5, Ratio 6, and Ratio 7, respectively. Inset TEM images have 100 nm scale bars. For all analysis, distributions were normalized to N = 250 AuNPs. **h)** Overlay of Gaussian normal distributions of TEM estimated diameter for all synthesized CTAC-based AuNP ratios.

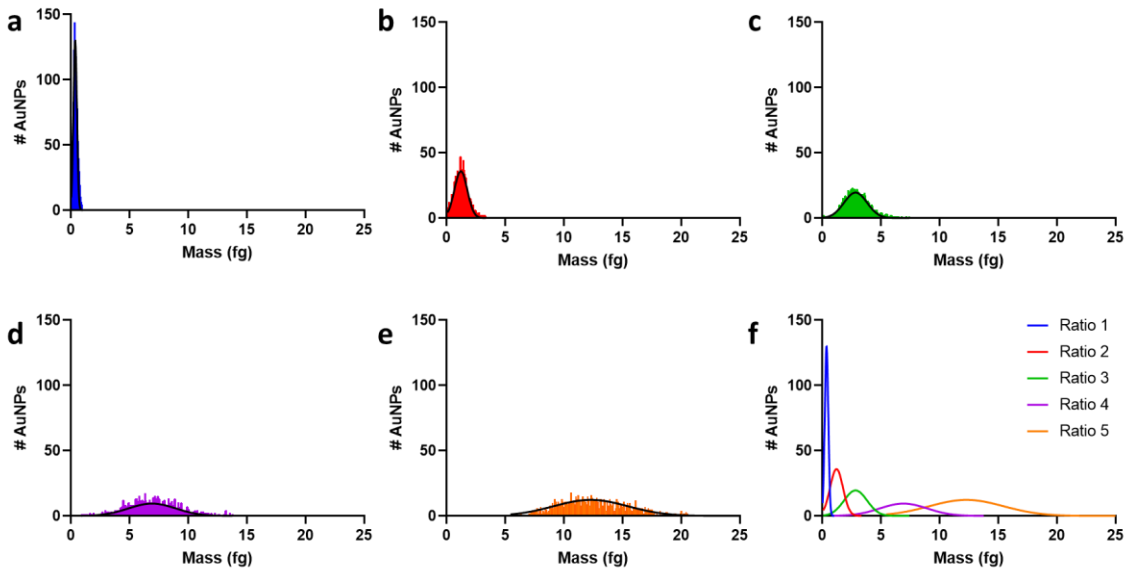

Figure C4.6: SP-ICP-MS characterization of citrate-based AuNPs by mass. a-e) Gaussian normal distributions of citrate-based AuNP measured mass from SP-ICP-MS measurements of Ratio 1, Ratio 2, Ratio 3, Ratio 4, and Ratio 5, respectively. For all analysis, distributions were normalized to N = 1000 AuNPs. **f)** Overlay of Gaussian normal distributions of SP-ICP-MS measured mass for all synthesized citrate-based AuNP ratios.

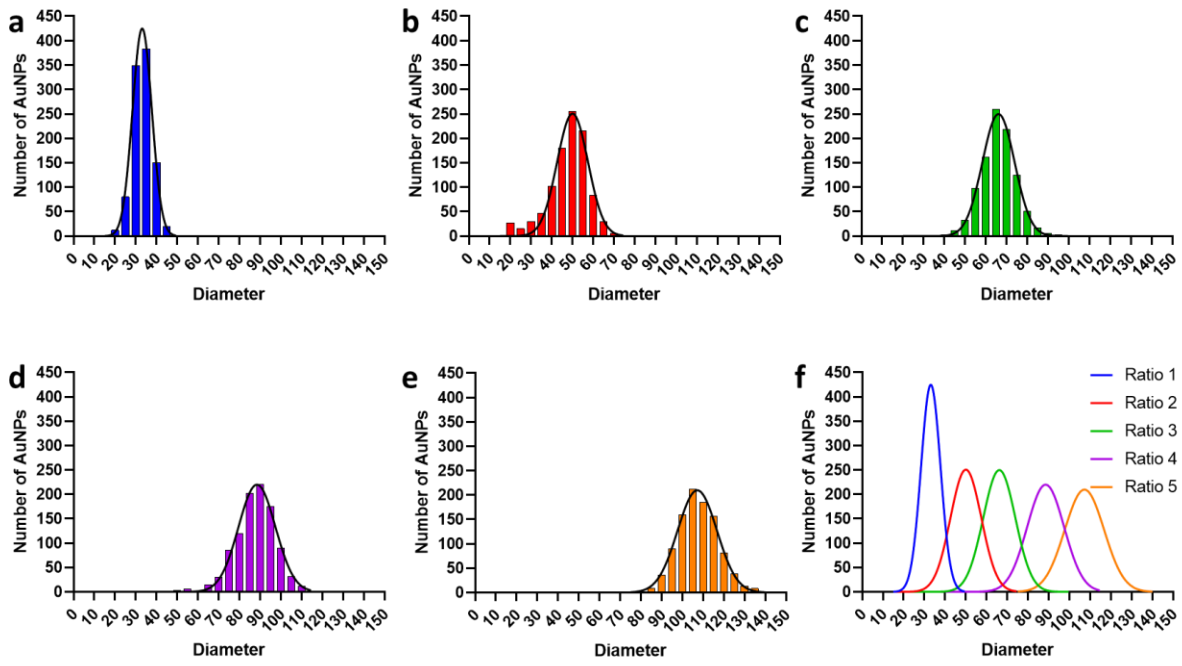

Figure C4.7: SP-ICP-MS characterization of citrate-based AuNPs by diameter. a-e) Gaussian normal distributions of citrate-based AuNPs diameter estimates from SP-ICP-MS analysis of Ratio 1, Ratio 2, Ratio 3, Ratio 4, and Ratio 5, respectively. For all analysis, distributions were normalized to N = 1000 AuNPs. **f)** Overlay of Gaussian normal distributions of SP-ICP-MS estimated diameter for all synthesized citrate-based AuNP ratios.

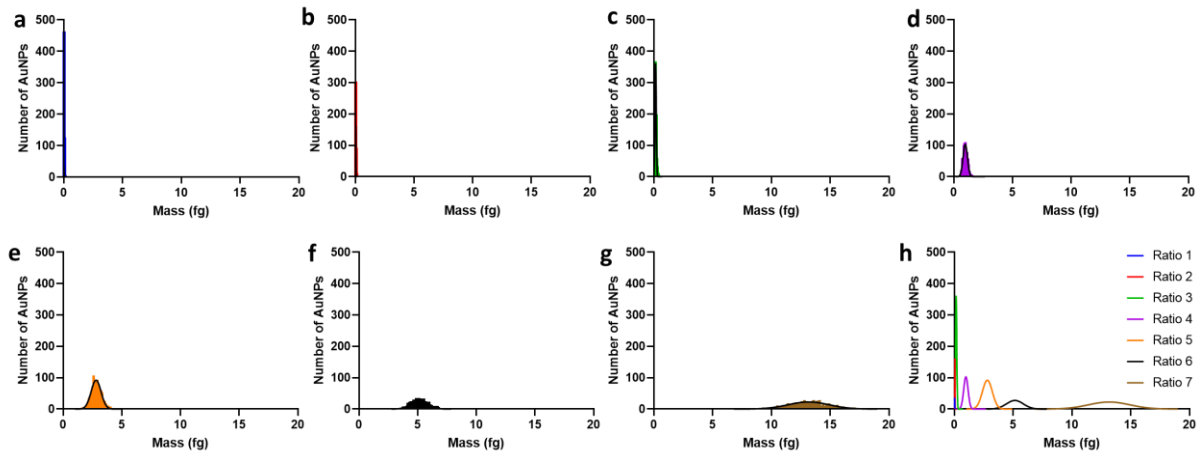

Figure C4.8: SP-ICP-MS characterization of CTAC-based AuNPs by mass. a-g) Gaussian normal distributions of CTAC-based AuNPs measured mass from SP-ICP-MS analysis of Ratio 1, Ratio 2, Ratio 3, Ratio 4, Ratio 5, Ratio 6, and Ratio 7, respectively. For all analysis, distributions were normalized to N = 1000 AuNPs. **h)** Overlay of Gaussian normal distributions of SP-ICP-MS measured mass for all synthesized CTAC-based AuNP ratios.

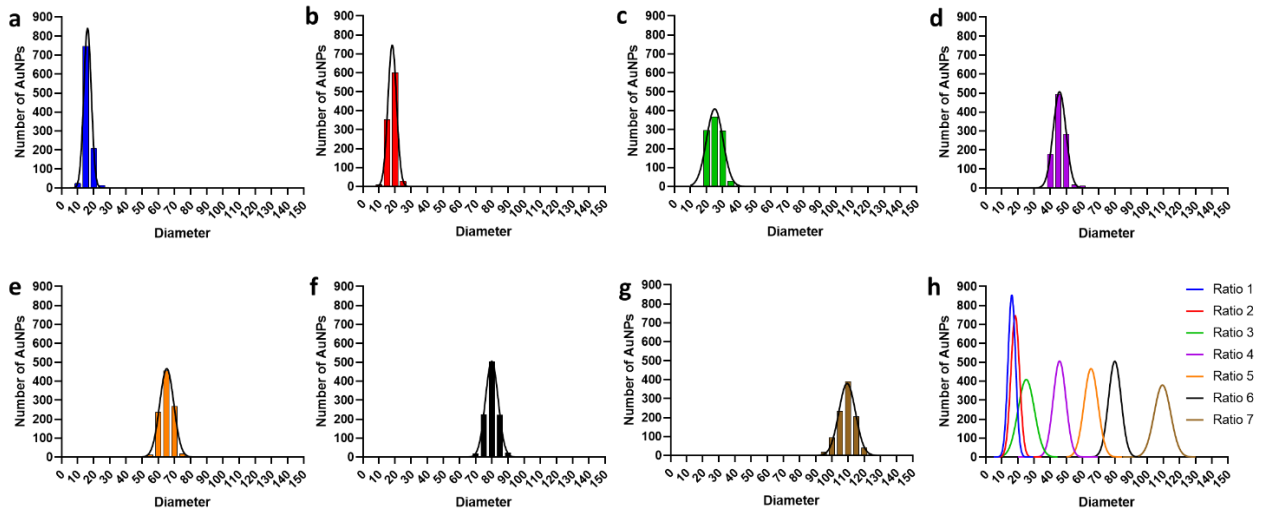

Figure C4.9: SP-ICP-MS characterization of CTAC-based AuNPs by diameter. a-g) Gaussian normal distributions of CTAC-based AuNPs diameter estimates from SP-ICP-MS analysis of Ratio 1, Ratio 2, Ratio 3, Ratio 4, Ratio 5, Ratio 6, and Ratio 7, respectively. For all analysis, distributions were normalized to N = 1000 AuNPs. **h)** Overlay of Gaussian normal distributions of SP-ICP-MS estimated diameter for all synthesized CTAC-based AuNP ratios.

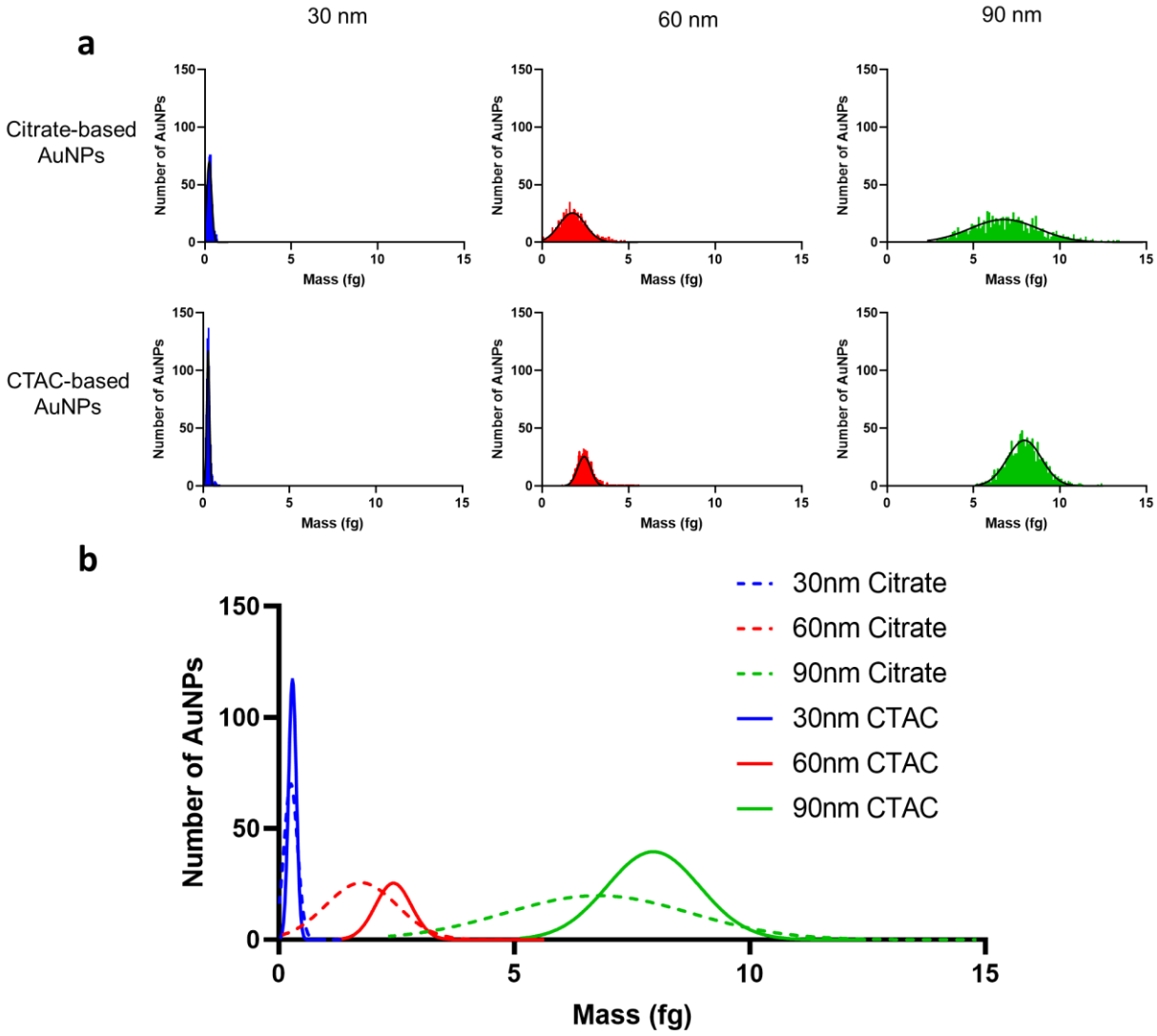

Figure C4.10: SP-ICP-MS characterization by mass of AuNPs synthesized to test model accuracy. **a)** Gaussian normal distributions of measured masses for AuNPs synthesized for specific target diameters. For all analysis, distributions were normalized to N = 1000 AuNPs. **b)** Overlay of Gaussian normal distributions of SP-ICP-MS measured masses for all AuNPs to test model accuracy.

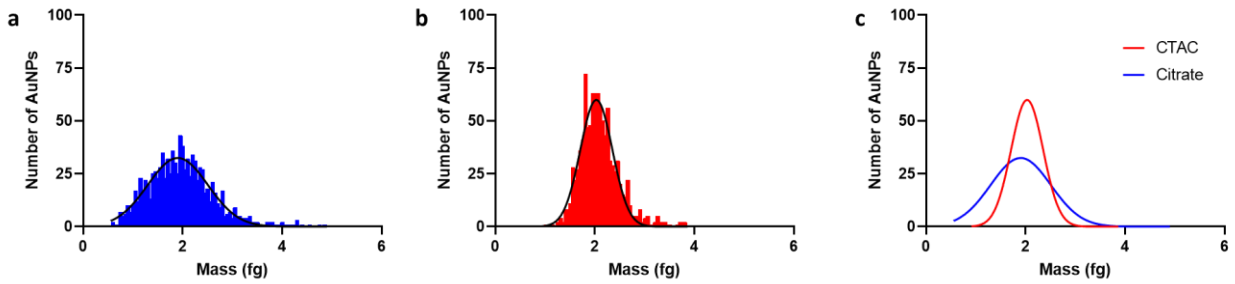

Figure C4.11: SP-ICP-MS characterization by mass of AuNPs synthesized to test scale-up model accuracy. **a)** Gaussian normal distribution of mass measured by SP-ICP-MS for 5x scale 60 nm target citrate-based AuNPs, normalized to N = 1000 AuNPs. **b)** Gaussian normal distribution of mass measured by SP-ICP-MS for 5x scale 60 nm target CTAC-based AuNPs, normalized to N = 1000 AuNPs. **c)** Overlay of citrate- and CTAC-based Gaussian normal distributions for mass measured by SP-ICP-MS.

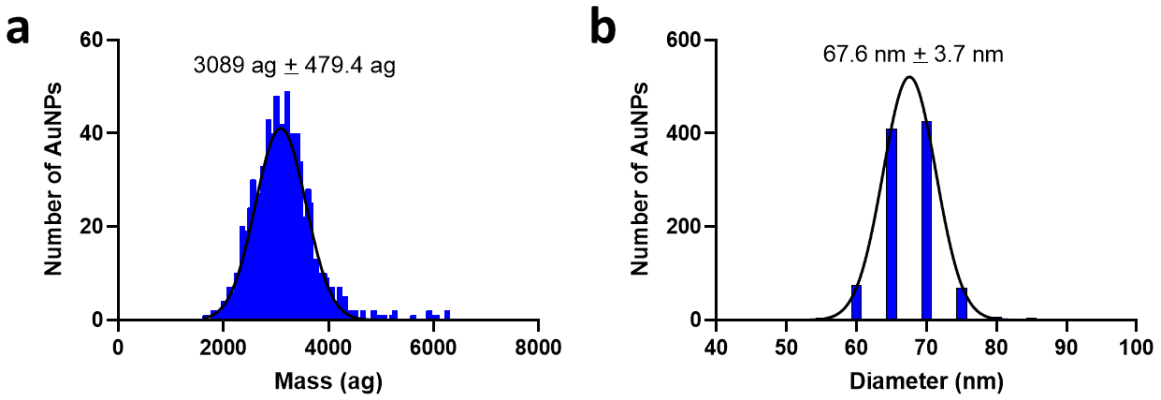

Figure C5.1: Representative SP-ICP-MS measurements of 60 nm CTAC-based AuNPs used in Chapter 5. a) Gaussian normal distribution of SP-ICP-MS measured mass of 60 nm CTAC-based AuNPs, normalized to N = 1000 AuNPs. **b)** Gaussian normal distribution of SP-ICP-MS estimated diameter of 60 nm CTAC-based AuNPs, normalized to N = 1000 AuNPs. While the mass and diameter values deviate from the target 60 nm, the AuNPs were usable for the purposed of testing CTAC removal by citrate-PR.

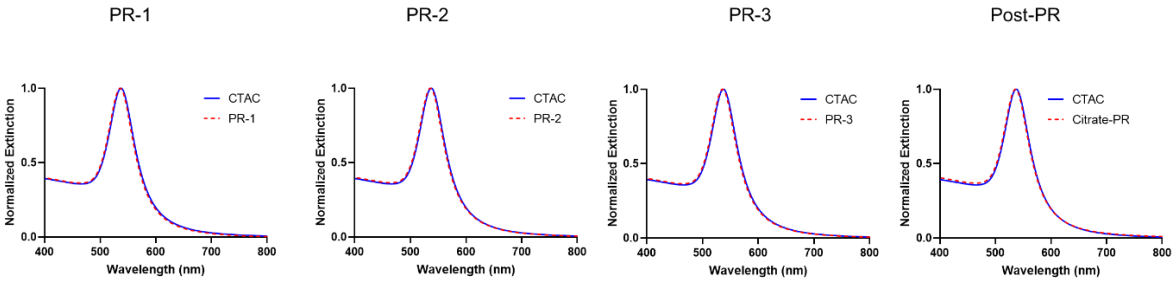

Figure C5.2: Stepwise analysis of citrate-PR using UV-Vis spectrophotometry. Normalized extinction spectra between 60 nm CTAC-based AuNPs were compared throughout the citrate-PR process. “PR-1” indicates the first step in the citrate-PR process, “PR-2” indicates the second step in the citrate-PR process, etc. No significant change in extinction spectrum is observed at any point throughout the citrate-PR process.

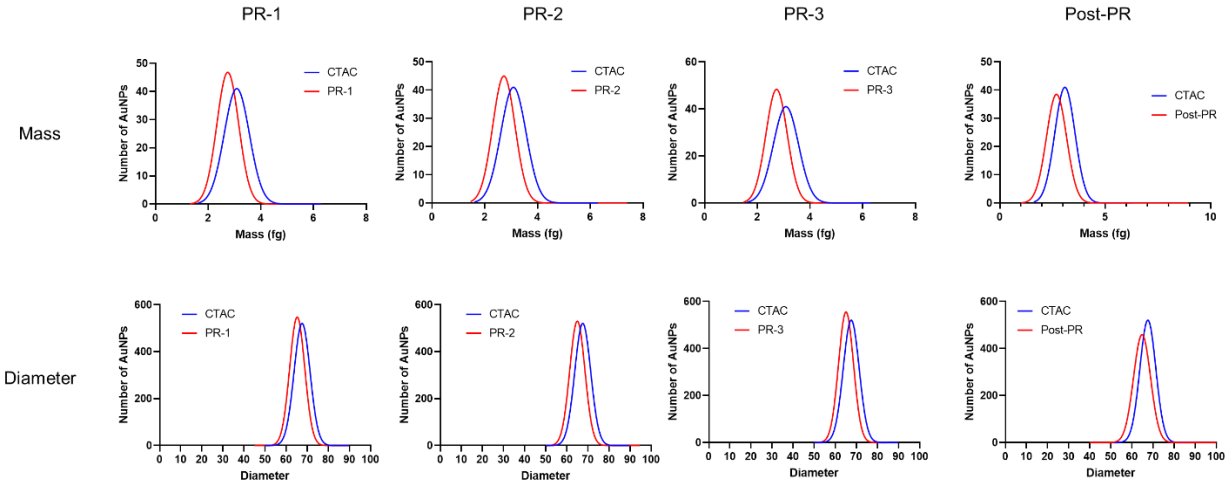

Figure C5.3: Stepwise analysis of citrate-PR using SP-ICP-MS. Mass measurements and diameter estimates of 60 nm CTAC-based AuNPs undergoing citrate-PR were collected using SP-ICP-MS. “PR-1” indicates the first step in the citrate-PR process, “PR-2” indicates the second step in the citrate-PR process, etc. No significant change in distribution, mass, or diameter is observed throughout citrate-PR compared to the as-synthesized control.

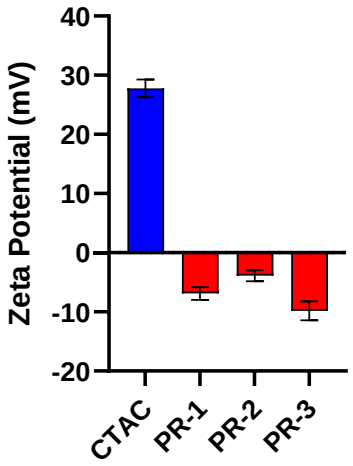

Figure C5.4: Stepwise analysis of citrate-PR using zeta potential measurements. Zeta potential measurements collected during the citrate-PR process performed on 60 nm CTAC-based AuNPs were analyzed to assess changes in surface charge associated with the removal of CTAC. “PR-1” indicates the first step in the citrate-PR process, “PR-2” indicates the second step in the citrate-PR process, etc. The shift from positive surface charge to negative surface charge is attributed to the removal of CTAC from the surface of the AuNPs.

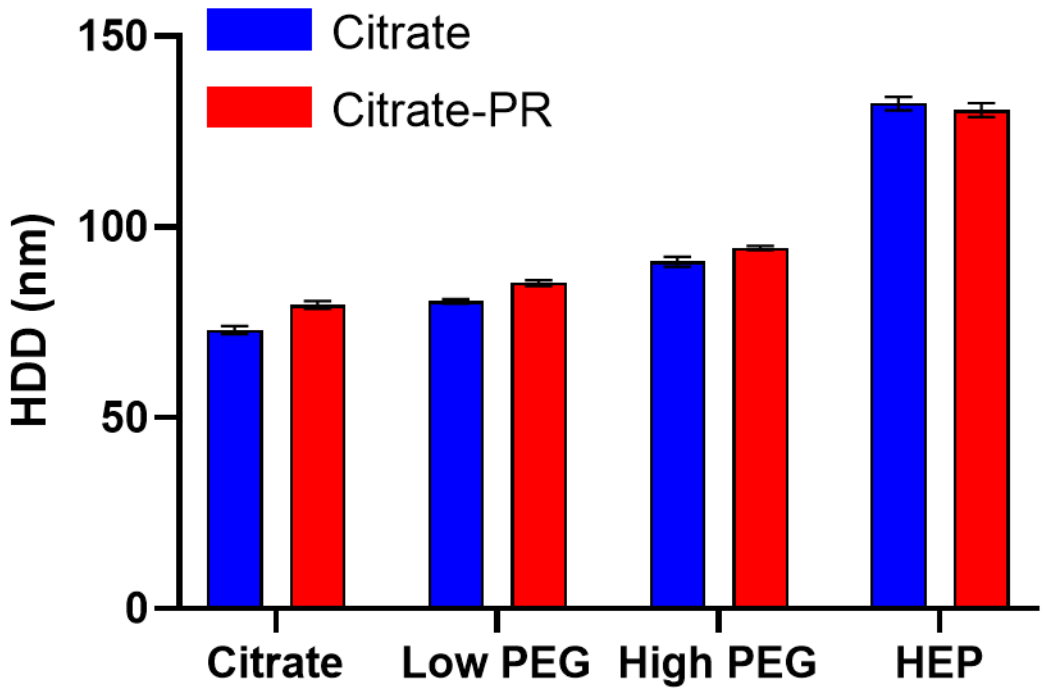

Figure C5.5: Representative DLS measurements of AuNPs used for cell and protein studies. Colored bars indicate measured HDD of AuNPs of different cores (citrate-based or post-citrate-PR) and different surface chemistries. Black error bars indicate standard deviation.

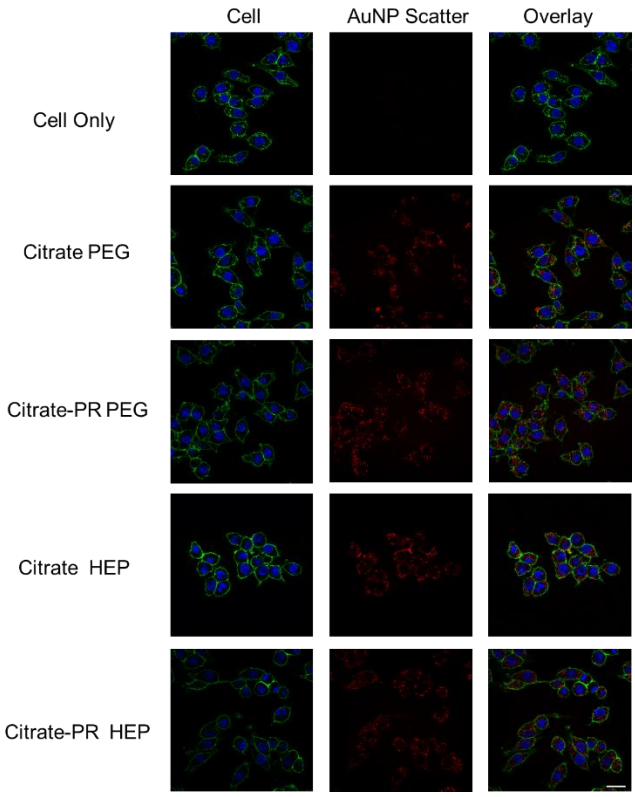

Figure C5.6: CSLM images of RAW 264.7 macrophages treated citrate-based and post-citrate-PR CTAC-based AuNPs of different surface chemistries. Blue shows the cell nucleus (DAPI), green shows the cell membrane, and red shows scattering of light caused by AuNPs. Similar qualitative uptake is observed between AuNPs of the same surface chemistry. Scale bar is 20 µm.

Appendix D – Supporting Tables

Table D3.1: Reagent volumes and centrifugation conditions for citrate-capped AuNPs.

Target AuNP Diameter (nm)	2.4-nM 14-nm AuNP Seed Volume (mL)	0.025-M $HAuCl_4$ Volume (mL)	Centrifugation Speed (rcf)
30	11.29	0.887	3500
45	3.35	0.967	2000
60	1.41	0.986	1200

Table D3.2: Ten-nm CTAC-capped AuNP seed volumes and centrifugation conditions for CTAC-capped AuNPs.

Target AuNP Size	Seed Volume (µL)*	Centrifugation Speed (rcf)
15	3821.3	15000
30	556.9	3500
45	120.4	2000
60	40.6	1200

*Volume of a 19.9-nM colloidal dispersion of 10-nm CTAC-capped AuNP seeds.

Table D3.3: Conditions Used for SP-ICP-MS Measurements.

Setting	Value
RF Power	1600
Nebulizer Gas Flow (mL/min.)	0.43
Make up gas flow (mL/min.)	0.73
Sample Flow rate (mL/min.)	0.013
Dwell time (µs)	50
Scan time (s)	30

Table D3.4: Details on DNA Strand used

DNA Sequence Name	DNA Sequence	Molar Extinction Coefficient (L mol^{-1} cm^{-1})
OligoA	5'- HS—AAAAAAAAAACCTATCGACCATGCT- 3'	256,500
OligoB	5'- TAACAACGATCCCTCAAAAAAAAAA—SH- 3'	263,500
Linker	5'- GAGGGATCGTTGTTATACAGTTCAGGCAGTGTAGCATGGTCGATAGG- 3'	472,200

Table D4.1: SP-ICP-MS Mass Measurements of Synthesized AuNPs for Predictive Model

AuNP Type	Ratio Number	AuNP/Au Ratio Value (mols AuNP/mols Au3+)	Mean Mass (ag)[#]
Citrate	1	1.22E-06	353.9 ± 147.7
	2	3.33E-07	1206 ± 547.8
	3	1.37E-07	2831 ± 981.2
	4	5.75E-08	6920 ± 2033
	5	2.94E-08	12285 ± 3173
CTAC	1	7.20E-06	32.4 ± 10.3
	2	4.00E-06	48.8 ± 8.3
	3	1.01E-06	161.0 ± 51.7
	4	1.85E-07	983.5 ± 186.6
	5	7.56E-08	2810 ± 421.9
	6	4.60E-08	5152 ± 717.9
	7	1.60E-08	13171 ± 1765

[#] Mean value ± standard deviation.

Table D4.2: SP-ICP-MS Mass, Diameter, and Monodispersity Measurements of Synthesized AuNPs for Confirming Model and Scale-up Accuracy

AuNP Type	Target Diameter (nm)	Mean Mass (ag)[#]	Mass FWHM (ag)	Mass RSD (%)	Mean Diameter (nm)[#]	Diameter FWHM (nm)	Diameter RSD (%)
Citrate	30	256.9 ± 143.2	337.2	55.7	30.3 ± 4.2	9.9	13.9
	60	1755 ± 756	1780	43.1	56.5 ± 8.0	18.8	14.2
	60 (5x Scale-up)	1903 ± 605.4	1426	31.8	57.6 ± 6.3	14.8	10.9
	90	6777 ± 1967	4632	29.0	88.1 ± 8.8	20.7	10.0
CTAC	30	292.7 ± 82.1	193.3	28.0	30.6 ± 3.0	7.1	9.8
	60	2436 ± 380.9	897.0	15.6	62.7 ± 3.7	8.7	5.9
	60 (5x Scale-up)	2032 ± 322.9	760.4	16.4	58.7 ± 3.9	9.2	6.6
	90	7953 ± 985.2	2320	12.4	92.5 ± 4.2	9.9	4.5

[#] Mean value ± standard deviation.

Table D5.1: Representative DLS HDD measurements of AuNPs used in Chapter 5

AuNP Type	Surface Chemistry	HDD (nm)[#]	PDI[#]
Citrate	Citrate[*]	73 ± 1.1	0.05 ± 0.03
	Low PEG	80.5 ± 0.6	0.02 ± 0.03
	High PEG	90.9 ± 1.3	0.04 ± 0.01
	HEP	132.3 ± 1.8	0.03 ± 0.03
CTAC	CTAC	79.5 ± 0.5	0.04 ± 0.02
	Citrate[^,*]	79.6 ± 1.0	0.03 ± 0.02
	Low PEG	85.3 ± 0.7	0.04 ± 0.02
	High PEG	94.5 ± 0.6	0.02 ± 0.02
	HEP	130.6 ± 1.8	0.02 ± 0.01

[*] Includes Tween20

[^] AuNPs underwent citrate-PR process

[#] Mean value ± standard deviation

Appendix E – Permissions

Reuse for Chapter 2

Permission for Figure 2.1 has been acquired from the American Chemical Society, Copyright 2023.

Permission for Figure 2.2 has been acquired from the American Chemical Society, Copyright 2023.

Permission for Figure 2.3 has been acquired from the Royal Chemical Society, Copyright 2023.

Permission for Figure 2.4 has been acquired from the American Chemical Society, Copyright 2023 (https://pubs.acs.org/doi/10.1021/acs.analchem.9b01870). Further permission related to Figure 2.4 in this work should be directed to the ACS.

All permission files for Chapter 2 are available upon request. Please contact africk256@ou.edu as needed.

Reuse for Chapter 3

Permission for reuse for all content used in Chapter 3 has been granted from Springer Nature, Copyright 2023.

Permission files available upon request. Please contact africk256@ou.edu as needed.